APPLICATIONS OF POLYOXOMETALATES AS ELECTRON MEDIATORS

by

Chaokang Gu

A dissertation submitted to the Graduate Faculty of
Auburn University
in partial fulfillment of the
requirements for the Degree of
Doctor of Philosophy

Auburn, Alabama
December 18, 2009

Polyoxometalates, Electrocatalysis, Fuel Cell, Nanotechnology
Semiconductor Electrochemical Deposition

Approved by

Curtis Shannon, Chair, Professor of Chemistry and Biochemistry
Vince Cammarata, Associate Professor of Chemistry and Biochemistry
Minseo Park, Associate Professor of Physics
Wei Zhan, Assistant Professor of Chemistry and Biochemistry

Abstract

The large variety of size, structure and elemental composition of polyoxometalates leads to a wide range of different properties. The primary goal of this dissertation is to study the structure-property relationship of polyoxometalates and to employ these versatile molecules as electron mediator in nano-scale. Stability of some polyoxometalates in the presence of metal ions in aqueous environment will also be discussed.

Chapter 1 provides the motivation of studies and an introduction to polyoxometalate structure and chemistry with a detailed literature review of the value added properties responsible for the electrocatalytic activities of polyoxometalates used in this research. Insights into the phenomenon of electrocatalysis are provided and the suitability of employing polyoxometalates as electron transfer mediators is discussed in detail.

Chapter 2 deals with the application TiO_2-Polyoxometalate co-catalyst system for use in a hybrid photo-electrochemical cell to oxidize methanol. We employed a simple α-Keggin-type polyoxometalate ($PW_{12}O_{40}^{3-}$) that is known to adsorb to the surface of positively charged TiO_2 particles at low pH. The use of the co-catalyst system dramatically improves the separation of photogenerated electron–hole pairs in suspended TiO_2 nanoparticles, leading to a 50-fold increase in the observed photocurrent compared to the use of TiO_2 alone. Due to the improved charge separation offered by the co-catalyst system, the new kinetic limitation appears to be the electron transfer from the reduced polyoxometalate to the anode. In addition, we find that the polyoxometalate itself can oxidize methanol efficiently in the absence of TiO_2. However,

photogenerated holes in the POM are unable to oxidize either formic acid or acetic acid, in contrast to the behavior of TiO_2. The dependence of the photocurrent on [$PW_{12}O_{40}^{3-}$] was also investigated. We find that the optimum [$PW_{12}O_{40}^{3-}$] is approximately 2 mM. A study of pH dependence is performed. An optimum pH equal to ~3 is found, suggesting a balancing of two processes. A survey using two other α-Keggin-type polyoxometalates ($SiW_{12}O_{40}^{3-}$ and $PMo_{12}O_{40}^{3-}$) is also executed. The comparison of results of three polyoxometalates meets our theoretical expectation well.

In Chapter 3, Au nanoparticle films were prepared on glassy carbon supports by depositing alternating layers of positively charged poly(diallyldimethylammonium)-stabilized Au nanoparticles and negatively charged Cobalt substituted α_2-Wells-Dawson-polyoxometalate ($CoP_2W_{17}O_{61}^{8-}$) interlayers. The polyoxometalate anions act as electron shuttles transferring electrons between the carbon electrode and Au nanoparticles, as well as between adjacent Au nanoparticles layers. Au/CuI, Au/CdS and Au/CdTe core-shell nanoparticle thin films were synthesized using codeposition and electrochemical atomic layer deposition (EC-ALD). CuI was deposited onto the surface of Au nanoparticles using electrochemical atomic layer deposition, while CdS and CdTe films were grown by an atom-by-atom codeposition method. The Au-semiconductor core-shell nanoparticles were characterized by electrochemistry, photoluminescence spectroscopy, and Raman spectroscopy. Our results indicate that the semiconductors are deposited onto the Au nanoparticles surface by surface-limited electrochemical reactions. A Mott-Schottky analysis using capacitance data from electrochemical impedance spectroscopy is also discussed.

Chapter 4 deals with dual-functional aspect of polyoxometalates in photosynthesis of Ag nanoparticles. The Ag nanoparticles prepared by simple α-Keggin-type polyoxometalate

($PW_{12}O_{40}^{3-}$) and sandwich type polyoxometalate ($[WZn_3(H_2O)_2(ZnW_9O_{34})_2]^{12-}$) are characterized by UV-vis, TEM and Dynamic light Scattering. The fact that polyoxometalates can serve as both reducing agent and stabilizing agent in metal nanoparticles synthesis has been well known. The Ag nanoparticles synthesized by $[WZn_3(H_2O)_2(ZnW_9O_{34})_2]^{12-}$ in return assist the polyoxometalate blackberry structure formation. Only Polyoxometalates with very large sizes are reported to self-assemble into the blackberry structures. $[WZn_3(H_2O)_2(ZnW_9O_{34})_2]^{12-}$ is much smaller in size than those reported. The roles of Ag nanoparticles in blackberry structure formation are discussed. A detail mechanism is proposed.

Chapter 5 presents a degradation phenomenon of giant Keplerate type mixed valence polyoxometalate $Mo^{VI}_{72}Mo^{V}_{60}O_{372}(CH_3COO)_{30}(H_2O)_{72}]^{42-}$ catalyzed by Cu^{2+}. The degradation is monitored by UV-vis spectroscopy. The decomposition of $Mo^{VI}_{72}Mo^{V}_{60}O_{372}(CH_3COO)_{30}(H_2O)_{72}]^{42-}$ is not sensitive to other divalent metal cations such as Co^{2+} and Ni^{2+}.

Chapter 6 provides a brief conclusion of this research and recommendations for further research.

Acknowledgments

I would like to give deepest appreciation to Dr. Curtis Shannon for his continuous guidance, invaluable inspiration and endless support through the entire research work during the Ph.D period in Auburn University. I would like to give thanks to all the committee members, Dr. Vince Cammarata, Dr. Minseo Park, and Dr. Wei Zhan for their valuable suggestions and helpful insights in aiding the course of my research. I would also like to thank my outside reader Dr. Dong-Joo Kim for his participation in evaluating my work.

I have received so much support from the faculty and staffs at Auburn. I am very thankful to Mr. Tom Carrington for his helpful suggestions and assistance in setting up analytical instrumentation. I would like to thank Dr. S. D. Worley for his gifting of TiO_2 P25 nanopowder sample; Dr. W. C. Neely for his gifting of organophosphous sample; Dr. G. Mills for the use of the Rayonet photochemical reactor; Dr. Michael Miller for the help in using TEM; Dr. Bart Prorok for the help in using SEM. Dr. Ram B. Gupta for his permission using the Dynamic Light Scattering instrument; Dr. David M. Stanbury for his permission using the UV-vis spectroscopy and Electrochemical AC Impedance instrument; and Dr. Thomas Albrecht-Schmitt and his group for the help in XRD characterization.

My colleagues in Dr. Shannon group have been very helpful at various stages of my study at Auburn and I would like to thank each one of them, Dr. Ugur Tamer, Dr. Yuming Chen, Dr. Lunsheng Zhang, Dr. Tsunghsueh Wu, Dr. Junxua Xin, Dr. Anand Sankarraj, Dr. Hongxia

Zhang, Ms. Sridevi Ramakrishnan, Ms. Rajakumari Ramaswamy, Ms.Weiping Li, Ms. Sanghapi Ndzesse, Ms. Tanyu Wang, and Ms. Yajiao Yu.

I would also like to thank all the friends and colleagues at Auburn for the supports and encouragement, both at work and out of it.

I would like to thank my parents, sister for their support and encouragement during my graduate studies. Last but not least, I would like to express special thanks to my girlfriend Hui Xu, without her caring, encourage and endless love, the work could be much harder to finish.

Table of Contents

List of Tables

List of Figures

Chapter 1.

Introduction

1.1 Research Motivations

The mission for scientific community is to improve our understanding to the nature. In the meantime, it's better to help solving real world problems. Global warming, environmental pollutions, and the energy crisis are some of the main challenges facing the scientific community, and the world in general, in the twenty-first century. Coal, oil and natural gas currently provide more than 85% of all the energy consumed in the United States[1]. These fossil fuels, essentially storage of ancient solar energy, supply nearly two-thirds of electricity, and virtually all of the transportation fuels. The reserves of these fossil fuels, however, are not unlimited, and are in fact, approaching the bottom. The development of alternative energy sources to take the place of these fossil fuels is a promising solution to these problems. With respect to everyday use, electricity is the ideal energy source. It is clean, controllable, and easy to be produced, stored, and transported. Hence, converting energy from alternative source other than fossil fuel into the form of electricity is desirable. Numerous groups around the world are striving to investigate such conversion systems[2], namely fuel cells and solar cells. In these systems, catalysts play the key role in terms of efficiency, economical feasibility and environmental viability. A catalyst with stable electron mediating ability would be beneficial to these alternative energy technologies.

Based on previous research[3,4], polyoxometalates are very promising in terms of retaining structural stability when undergoing redox reaction. In this context, we have embarked on a journey to investigate the electron mediation properties of polyoxometalates and their potential applications.

1.2 Introduction to Polyoxometalate (POM)

1.2.1 Fundamentals

Polyoxometalates (POM) are a group of large, closed 3-dimensional polyanion frameworks that form via self assembly of monomeric oxoanions in acidic solutions. The polyanion usually consists of three or more metal oxyanions linked together by shared oxygen atoms. The metal atoms in the oxoanions are usually group V or group VI transition metals in their high oxidation states, normally with electron configuration of d^0 or d^1. Typical examples include vanadium (V), niobium (V), tantalum (V), molybdenum (VI), and tungsten (VI). Unlike main group metals, transition metals may have multiple oxidation states, since they can lose d electrons without a high energetic penalty. This feature of transition metals can be extended to polyoxometalates, and enable polyoxometalates to undergo multiple one- or two- electron oxidation/reduction. Some polyoxometalates can accept as many as 32 electrons without major structural modification[5]. Thus, this group of molecules possesses opportunities, insights, properties, and applications that cannot be matched by any other single group of inorganic compounds[6].

1.2.2 Retrospectives

Even though the first observation of polyoxometalates dates back to centuries ago when Native Americans observed mysterious "blue water" from Idaho Springs or the Valley of the Ten Thousand Smokes[7], the scientific community did not pay much attention to polyoxometalates until the late eighteenth century. In 1826, Berzelius[8] described that the yellow precipitate produced when ammonium molybdate is added in excess to phosphoric acid and which is now known as $(NH_4)_3[PMo_{12}O_{40}]$. However the 12:1 composition was not revealed until Galissard de Marignac[9] discovered and determined the atomic ratio of the tungstosilicic acids and their salts in 1864. The first attempt to extract the exact structures of 12:1 species was made based on Werner's coordination theory[10] in 1907. The structural hypothesis was then further developed by Miolati and Pizzighelli[11], and later by Rosenheim[12] in the early 20th century. According to the so-called Miolati-Rosenheim theory, polyoxometalates were assembled based on six-coordinate units MO_4^{2-} or $M_2O_7^{2-}$, which showed structures different to the ones with modern inorganic chemistry. Pauling[13], however, questioned this and claimed that the basic units were octahedral based on his element radii measurement. Keggin[14] solved the first crystal structure of heteropolyanion $(H_5O_2)_3[PW_{12}O_{40}]$ by using X-ray diffraction, and the results supported Pauling's theory. By the mid-20th century, hundreds of polyanions had been reported and their chemical and physical properties had been described and some of these structures had been solved[12]. However, very little was known about the reactions of formation, degradation and interconversion of these species until Souchay[15-20] started the study of condensation reactions in solution by various techniques. Pope, then enabled the use of the NMR as a tool to resolve the structure of polyoxometalates in 1960s[21,22]. Pope contributed immensely to the field of polyoxometalates by publishing the leading monograph[5] on polyoxometalates and around 200

research papers, review articles and chapters. He developed a systematical method to prepare and characterizes heteropolyanions containing vanadium[23-28], niobium[23] and tantalum[29,30], lanthanide[31-36] and actinide elements, as well as their organic and organometallic derivatives. His groundbreaking work has important implications for homogeneous catalysis applications and nuclear waste management. It could be said that Pope had brought the research of polyoxometalates into the realm of modern inorganic chemistry and drawn the attention of workers of various areas to the great potential of these compounds.

1.2.3 Structures

Depending on the presence of heteroatoms X, polyoxometalates can be categorized into two groups: isopolyoxometalates and heteropolyoxometalates. Here the polyoxometalates discussed in this thesis are referred to heteropolyoxometalates only. The general formula of these two groups can be written as:

$$[M_mO_y]^{p-} \quad \textbf{Isopolyanions}$$

$$[X_xM_mO_y]^{q-} \quad \textbf{Heteropolyanions}$$

Where M is termed as addenda atoms, usually group V or group VI transition metals in their high oxidation states, normally with electron configuration is d^0 or d^1. The selection of addenda atoms appears to be limited by a combination of ionic radius, charge, and the ability to from dπ-pπ metal-oxygen bonds. Thus, only certain elements can be addenda atoms. In a contrast, there seems to be no such restriction on the heteroatoms X in a heteropolyanion. It has been reported that more than sixty-five elements from all groups in the periodic table, except for noble gases, can be filled as heteroatoms[5]. Taking several factors, such as different M/X ratio, more than one

kind of heteroatoms, and mixture of addenda atoms, into account, the number of different heteropolyanions could be unlimited.

Keggin structures

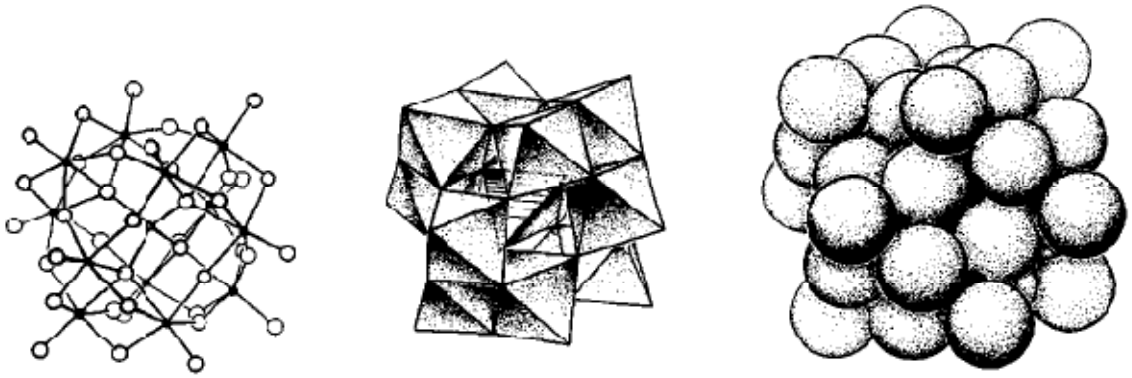

Figure 1.1 the α-Keggin structures in ball and stick, polyhedral, and space-filling representations. Taken from Ref. 5 with permission

The Keggin structures are the best known polyoxometalate structures. They were the first XRD-resolved structure of polyoxometalates which was reported by Keggin in 1933 for 12-tungstophosphoric acid, and later confirmed for numerous other compounds. Keggin structures are quasi-spherical molecules with diameter of approximately 1.2 nm, as show in Figure 1.1 in their α-isomer form[37].

The Keggin structure can be represented by the general molecular formula, $[XM_{12}O_{40}]^{x-8}$, where X is the heteroatom, x is the oxidation state of X, and M is the addenda atom.

From a more structural point of view, this formula can be re-written as $[XO_4 \cdot (MO_3)_{12}]^{x-8}$. The Keggin unit has a central XO_4 tetrahedron surrounded by twelve edge and corner-sharing MO_6 octahedra. These 12 MO_6 octahedra are arranged in four groups of three octahedra, M_3O_{13}, which are so-called "M_3 triplet". Each group is formed by three edges-sharing octahedra and linked by sharing a common corner oxygen atom. Each M_3 triplet group also shares an oxygen atom with the central tetrahedron XO_4.

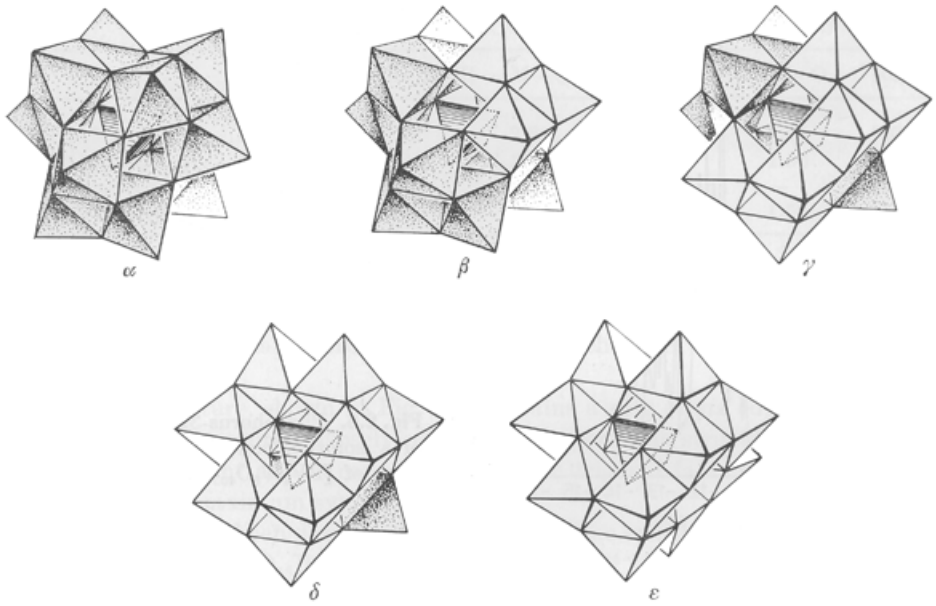

Figure 1.2 The five Baker-Figgis isomers of Keggin structures. Taken from Ref. 5 with permission

The Keggin structures have five different isomers. The α-Keggin structure is one with a symmetry point T_d. With one, two, three, and four M_3 triplet rotated by π/3 along their tri-fold axis, there forms β, γ, δ, and ε-isomers respectively. The structures of all five isomers are shown in Figure 1.2.

The overall symmetry for these five isomers are T_d (α), C_{3v} (β), C_{2v} (γ), C_{3v} (δ), and T_d (ε). The degrees of symmetries, however, have little relationship with stabilities of these isomers. The α-isomer is the most common Keggin anion. The rotation of M_3O_{13} triplets will result in a more acute M-O-M angle and a shorter M-M distance, which imply less favorable pπ-dπ interaction[38] and stronger coulombic repulsion[39] respectively. Thus, the more rotated the M_3O_{13} units, the less stable the Keggin unit is.

One or more MO_6 octahedron can be replaced by other octahedrally coordinated peripheral addenda atoms, which is the "mixed" Keggin with general formula $[XM'_xM_{12-x}O_{40}]^{n-}$. If more than one MO_6 octahedron is substituted, it will lead to numerous isomer possibilities termed positional isomers. The existence of positional isomers makes the number of possible polyoxometalates even larger. Taking $[PV_2W_{10}O_{40}]^{5-}$ as a quick example, its α-structure has 5 different positional isomers, and its β-structure can form 14 positional isomers, theoretically. Several of the 5 positional isomers of α-$[PV_2W_{10}O_{40}]^{5-}$ had been experimentally confirmed the existence by NMR and ESR[40].

If the MO_6 octahedron are removed from Keggin molecules and not replaced by other heteroatoms, "Keggin with holes" will be formed. This "defective Keggin" is termed Lacunary Keggin, which is shown in Figure 1.3[41]. Usually Keggin unit with one or two "holes" are used as precursors to prepare mixed Keggin materials. Of those trivacant lacunary structures, if there is a

removal of one corner-sharing MO_6 octahedron from each of three bridging M_3O_{13} triplets, it is called an A-type; if there is a removal of one entire M_3O_{13} triplet, it is called a B-type. Such trivacant species can be used as building blocks to assemble into larger polyoxometalate structures, either directly or by the incorporation of metal ion linkers.

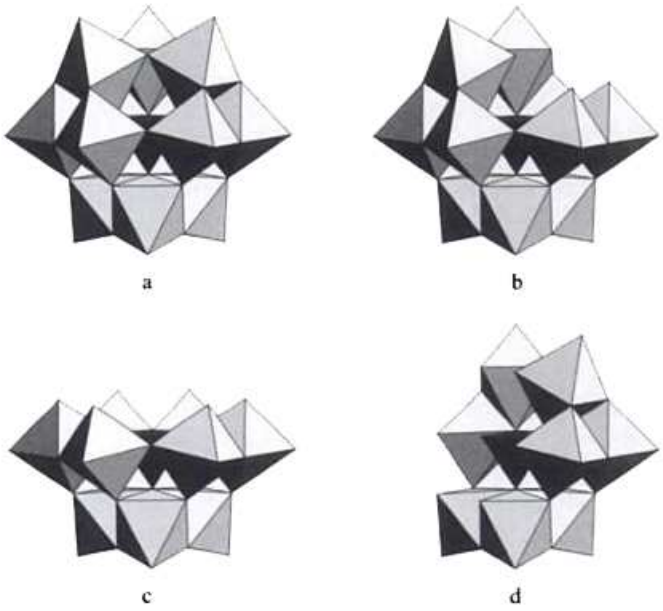

Figure 1.3 The structures of (a) α-Keggin anion $[XM_{12}O_{40}]^{x-8}$, and its lacunary derivatives: (b) monovavant, (c) A-type trivacant, (d) B-type trivacant. Taken from Ref. 5 with permission

Wells-Dawson Structures

One of these trivacant lacunary Keggin derivatives is the well-known Wells-Dawson heteropolyanion $[X_2M_{18}O_{62}]^{2x-16}$. Its α-structure is shown in Figure 1.4. The Wells-Dawson

structure was first synthesized by Kehrmann[42] in 1892 and then solved by Dawson[43] 60 years later. The Wells-Dawson polyoxoanion consists of two A-type trivacant lacunary Keggin units linked directly across the lacunae.

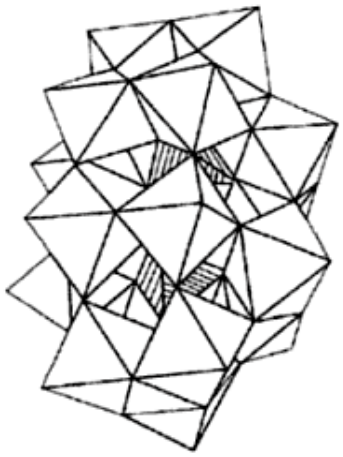

Figure 1.4 The structure of Wells-Dawson type polyoxometalate $[X_2M_{18}O_{62}]^{2x-16}$ (α-isomer). Taken from Ref. 5 with permission

The Wells-Dawson structure contains two M_3O_{13} groups. Its isomeric β structure can be originated by rotating one half unit of the α-isomer $\pi/3$ around the X-X axis. Similar to Keggin and many other polyoxometalate structures, the Wells-Dawson polyanions can be chemically manipulated to generate "Wells-Dawson with holes" species by removing up to 6 MO_6 octahedra. These "holes" of the lacunary species can be filled by other octahedrally coordinated elements and form substituted Wells-Dawson polyoxometalates.

Sandwich Type Polyoxometalate

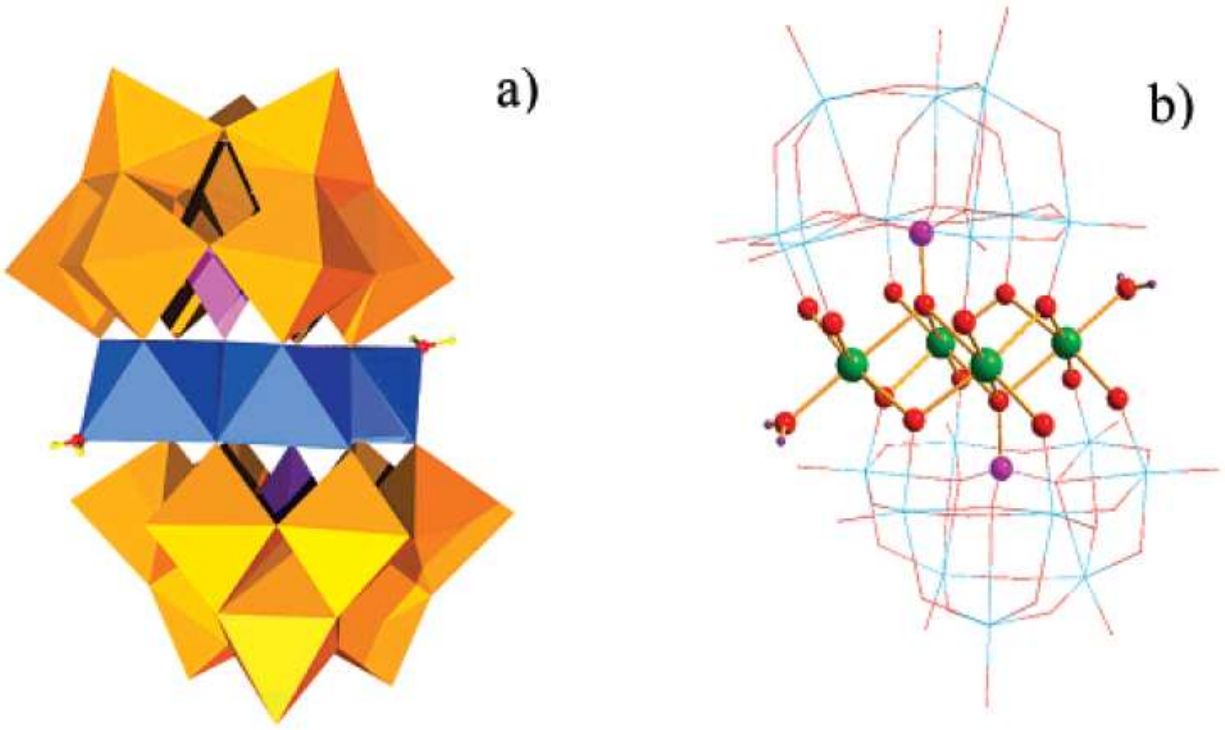

Figure 1.5 (a) The Polyhedral structure of sandwich type polyoxometalate $[M_4(H_2O)_2(XW_9O_{34})_2]^{n-}$ and (b) ball and stick structure of sandwich type polyoxometalate $[M_4(H_2O)_2(XW_9O_{34})_2]^{n-}$ with the central $M_4(H_2O)_2O_{14}$ unit in a highlighted.

Taken from Ref. 64 with permission.

Trivacant lacunary Keggin species can undergo self-assembly to form another type dimeric polyoxometalate framework - the sandwich structure, also known as Weakley or Tourne

structures. These sandwich complexes were first reported by Weakley, Tourne and co-workers[44] in 1973.

Sandwich structures are formed by two B-type trivacant α-Keggin fragments with vacant site facing each other and a belt shape central unit in between, as shown in Figure 1.5a. Many elements that may not be used as addenda atoms, such as Co, Cu, Zn, Mn, Fe, can fit in the central belt region of these sandwich type polyoxometalates (Figure 1.5b). Unlike heteroatoms that almost are fully covered by addenda octahedra, MO_6, the central atom at the belt region is fully exposed to the solution and can be directly involved in some reactions. Some noble metals, such as ruthenium[45-48], palladium[45] and platinum[45], based sandwich type structures, have revealed interesting catalytic properties and were believed to be promising in oxygen reduction reactions.

Giant Polyoxometalates and Their Second Solute State

Polyoxometalate chemistry has been developed rapidly in the past 15 years. As a result of the incorporation of advanced combinatorial strategies into inorganic chemistry, giant polyoxometalates, which can be regarded as inorganic 'nanomodels' for biological activity at the cellular level, can be created by self assembling systems using molybdates, vanadates and tungstates in solution as building blocks[49]. The first giant polyoxometalate was discovered by Müller[50] in 1995, with a giant wheel shape structure. Each molecule was made up of a total of 154 molybdenum atoms embedded in a network of oxygen atoms, as shown in Figure 1.6a. At that time, it was the largest inorganic molecular cluster ever characterized. Some other typical

examples of giant polyoxometalates includes ball shape Mo_{132}[51] (Figure 1.6b), and "Nano-hedgehog" Mo_{368}[52] (Figure 1.6 c and d).

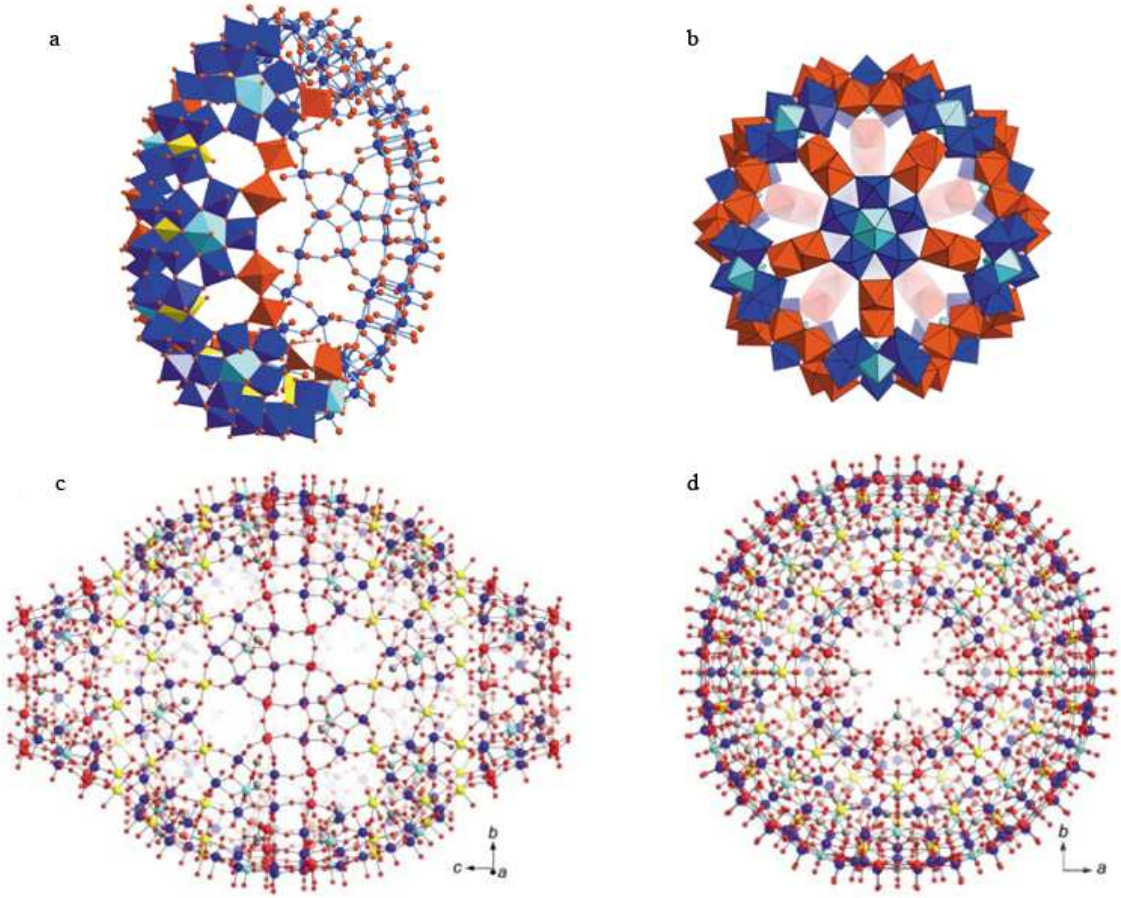

Figure 1.6 (a) the "Bielefeld giant wheel" Mo_{154}. (b) the "Keplerates" Mo_{132}. (c) and (d) sideview and toipview of the "Nano-hedgehog" Mo_{368}.

It should be noted that the nano-hedgehog Mo_{368} has an internal cavity 2.5 nanometers wide and 4 nanometers long which can encapsulate approximately 400 water molecules. It is

actually the size of a protein. It is believed that these giant polyoxometalates structures could be used as selective catalysts, similar to zeolites, or as nanoreactors.

These giant polyoxometalates can be self-assembled into a large ordered structure, which mimics the protein self-assembly into cell. The as-formed large structure, which was termed "second solute state", was first discovered by Liu in 2003. It will be developed into more detail in the following chapter.

Secondary, and Tertiary Structures

The structures of polyoxometalates being discussed in the previous sections are considered as primary structure by Misono[53]. The primary structure refers to the large polyanions. The polyaions, plus their counter-ions, water of crystallization or solvation, and other molecules, is the "secondary structure". In contrast, the tertiary structure refers to how polyoxometalates assemble in the solid state. The size of the particles, pore structure, and distribution of protons in the particle, are the characteristic elements of the tertiary structure. The term tertiary structure only applies to solid state polyoxometalates, which is beyond the scope of this dissertation. The graphical definitions of three structures of polyoxometalates are shown in Figure 1.7.

In general, the primary structure is maintained regardless of whether it is in solid state or in solution state. It remains unchanged in different solvents. In contrast, the secondary structure is very variable.

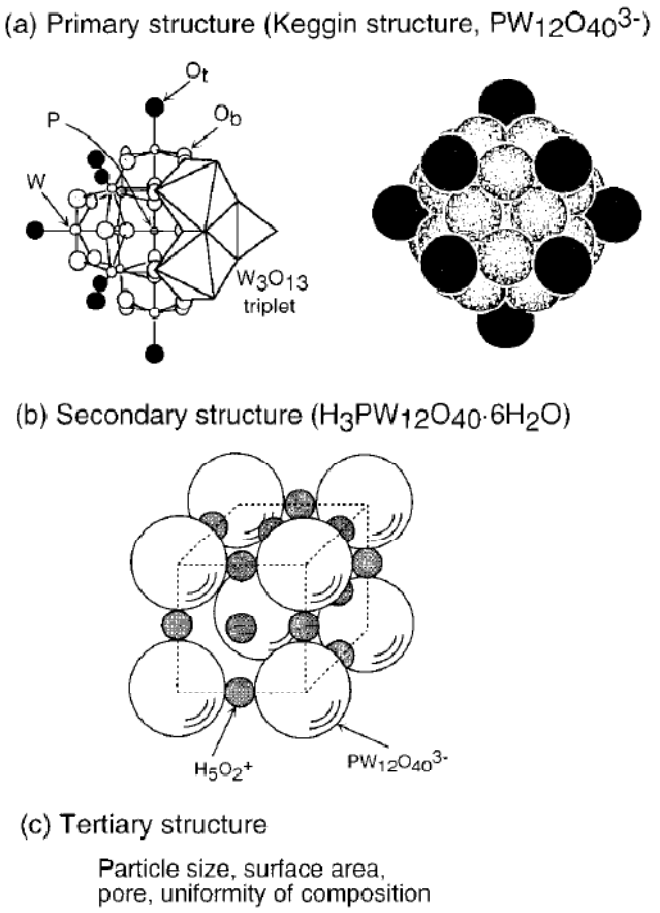

Figure 1.7 Primary, secondary, and tertiary structures of polyoxometalates: (a) primary structure (Keggin structure, $PW_{12}O_{40}$), (b) secondary structure ($H_3PW_{12}O_{40}\cdot 6H_2O$), and (c) tertiary structure.

1.2.4 Structure-Property relationship

The properties of polyoxometalates are closely related to their size, structure and elemental compositions. For example, some polyoxometalates exhibit luminescence due to the excitation of ligand-to-metal charge-transfer[54]; some polyoxometalates containing transition

metal atoms with unpaired electrons have unusual magnetic properties and are being investigated as electrically-controlled gates device for possible quantum bit computer data storage[55].

Polyoxometalates are most widely used as catalysts for a range of reactions, taking advantage of their thermal stability and reversibility of being reduced by accepting electrons. The catalytic properties of polyoxometalates are mainly determined by the electronic structure of the metal forming the bond with oxygen and also by the geometry of the polyanion structures. In fact, the degree of charge transfer from the metal to oxygen, which determines the degree of ionicity or covalence of the M-O bond, depends on the nature of the metal and on its coordination number, which in turns determines acid and oxidation–reduction properties properties of the polyoxometalate system. In another words, it is very important to the understanding of the metal-oxygen interaction. Taking Keggin as an example, there are totally 40 oxygen atoms in one Keggin polyanion and they can be categorized into four types based on their position in the matrix[41]:

• Twelve terminal oxygen atoms at the outer edge of MO_6 octahedra.

• Twelve edge-bridging angular M-O-M shared by three octahedra within the same M_3O_{13} triplet.

• Twelve corner-bridging quasi-linear M-O-M connecting two different M_3O_{13} triplets.

• Four X-O-M in the internal XO_4 tetrahedron.

All these four types of oxygen atoms can be individually addressed by ^{17}O NMR, and their metal-oxygen bonds provide the signature bands in the fingerprint range (600 to 1100cm^{-1})

in infrared spectroscopy. Thus, it is convenient to modify the Keggin unit structure to tune the properties of polyoxometalates.

One noteworthy catalytic processes of polyoxometalate have been reported as an environmentally friendly alternative to current widely-used but toxic approaches: a non-chlorine based, wood pulp bleaching process[56]. Some potential medical applications for antitumoral, antibacterial, and antiviral purposes have been reported as well[57].

1.3 Polyoxometalates as electrocatalysts

1.3.1Electrocatalysis

Catalysis is the process in which the rate of a chemical reaction is changed, either increased or decreased, by chemical substances termed as catalysts, which do not themselves show a permanent chemical change. Catalysts that speed up the reaction are called positive catalysts, while catalysts that slow down the reaction are called negative catalysts or inhibitors. In general, people want to get more desired products rather than less, from reactants (termed substrate). Positive catalysts can lower the activation energy of the chemical reaction, thus resulting in a higher reaction rate at the same temperature. Depending on whether catalysts exist in the same phase as the substrate or not, there are two type of catalysis. Heterogeneous catalysts are those which function in a different phases than the substrates. And homogeneous catalysts function in the same phase as the substrates.

Electrocatalysis usually relates to the increase of rates of electrochemical reactions, or the decrease of overpotential. Electrocatalysis is unique from other catalytic systems because the electrode potential can be controlled, and so do the electrochemical reaction rate. A relatively

small change in electrode potential can cause very large changes in rate for a reaction. For example, a change about 400 mV in electrode potential can cause 10^3 to10^{10} fold increase of reaction rate[58]. Both rate increase and decrease are of considerable practical importance in electrocatalysis since they can affect the economics of electrochemical processes. Similar to conventional catalysis, electrocatalysis can be divided into two types – heterogeneous electrocatalysis and homogeneous electrocatalysis. In heterogeneous electrocatalysis, the electrocatalyst can either function at electrode surfaces or may be the electrode surface itself. In contrast, the catalytic species is spread in electrolyte and in homogeneous electrocatalysis. In a homogeneous electrocatalytic reaction, the electrocatalysts assist in electron transfer between the electrode and substrates, as shown in Figure 1.8. Direct heterogeneous electron transfer between the electrode and the substrate is sometimes very slow because of poor interaction. In these cases the electrode reaction occurs only at high overpotentials. Electrocatalysts can minimize the activation energy and hence allow such an electrode reaction to occur at high current density close to the equilibrium potential or even considerably below it[59]. In an electrocatalytic reaction, an electrocatalyst is activated by a heterogeneous redox step at the electrode surface (E process) in order to react homogeneously with the substrate in the bulk solution (C process). The C process will regenerate the unactivated electrocatalyst.

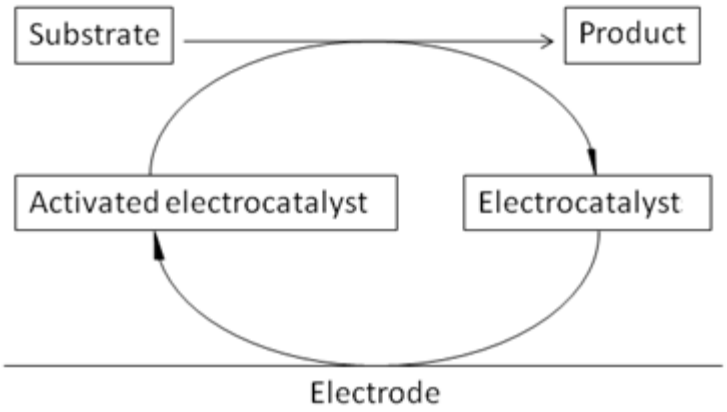

Figure 1.8 Schematic presentation of an electrochemical reaction catalyzed by electrocatalyst.

There is one more advantage that makes electrocatalysis unique from conventional catalysis. In conventional systems, the free energy of the reaction is turned into heat while it's possible to collect the free energy in the form of electricity by using electrocatalytic systems. Fuel-cell is the kind of devices that are designed to take advantages of it.

1.3.2 Polyoxometalates in electrochemical reactions

Although a large number of polyoxometalates has been prepared and characterized, the number of polyoxometalates which have been used as electrocatalysts is limited[59]. The redox ability of polyxoxmetalate is closely related to it molecular structure, especially the MO_6 octahedra structures. Depending on the displacement of metal atom from the center of the MO_6 octahedra, polyoxometalates are categorized into the following two types[5]:

1. Type I or Mono-oxo. The metal atom displacement occurs towards one, always terminal oxygen atom.

2. Type II or cis-dioxo. The metal atom displacement occurs towards two cis, usually but not always, terminal oxygen atoms.

For type I polyoxometalate, the metal atom in the MO_6 octahedra can be with d^0, d^1 and d^2 electronic configurations. There is an absence of in-plane Π bonding and the LUMO are normally non-bonding and is metal centered (d_{xy} orbital) in these type I polyoxometalates. Thus the type I polyoxometalates can easily accept electrons.

In type II polyoxometalates, the metal atom in the MO_6 octahedra can only be d^0 metals. The LUMO is strongly antibonding with respect to terminal M-O bonds. Thus accepting electron will result in irreversible decomposition of these type II polyoxometalates.

Theoretically, all type I polyoxometalate can be used as electrocatalyst. However, only α-Keggin, α-Dawson types polyoxometalates, their mixed-addenda derivatives, and their transition metal-substituted derivatives are used as electrocatalysts in practical because of their stability and ease of preparation.

The type I hpolyoxometalates can undergo several rapid one and two-electron reversible reductions to produce the so-called “heteropoly blue”, which are the result of reduced mixed valence polyoxometalate species, and further irreversible multi-electron reductions leading to decomposition.

For α-Keggin, α-Dawson polyoxometalates, the electrons are accepted by the addenda ions of the heteropolyanions. If the addenda ions are all identical, the electrons are delocalized

on the addenda MO_6 octahedra at room temperature by rapid electron hopping (intramolecular electron transfer)[5]. The reduction-induced-increased-negative-charge-density is spread over the polyoxoanion and thus the stability of polyoxometalate itself can be retained.

In the case of mixed addenda α-Keggin, α-Dawson polyoxometalates, the electrochemical character of polyoxometalates can be widely changed. The oxidizing ability of polyoxometalates can be arranged based on oxidizing ability of addenda atoms in the following order: V(V) > Mo(VI) > W(VI). In a simplified example of reduction reactions that only one-electron is transferred, the transferred electron of the reduced mixed-addenda heteropolyanions is considered localized on the more reducible atom at room temperature[60,61].

In most transition metal-substituted α-Keggin, α-Dawson polyoxometalates, the incorporated metal is the active site for the catalytic reactions. The metals incorporated in the polyxoxanion network reside in an octahedral environment with five coordination site linked by oxygen atom of the polyoxoanion and one coordination site occupied by a solvent molecule. In the case of aqueous solution, the solvent molecule is a labile water molecule. In general, the redox ability of transition metal-substituted polyoxometalates are depending on the character of the incorporated metals. Take Rhenium substitudeted Keggin[62,63] as an example, the aquametal(III) is reducible to the aquametal(II) and oxidizable to the corresponding oxometal(IV), hydroxometal(IV), oxometal(V) oxometal(VI) and -(VII) stage derivatives, as shown in Figure 1.9.

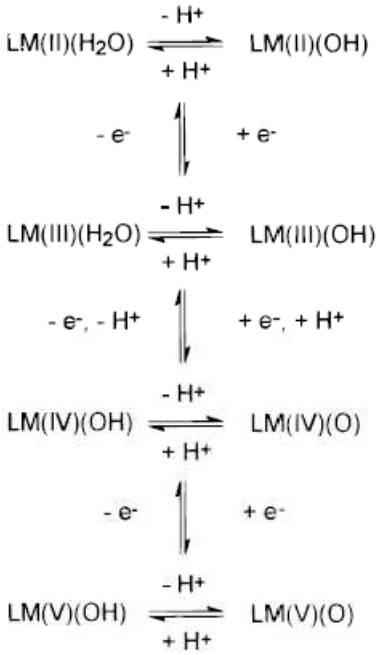

Figure 1.9 General Electrochemical Behavior of Transition Metal-Substituted Polyoxometalates. Taken from Ref. 59 with permission.

Applications of polyoxometalates as electrocatalysts and electron mediator will be explored in the following chapters. All four types of polyoxometalates described in this chapter are used in following studies. Specifically, the electron mediating behavior of Keggin, Wells-Dawson, Sandwich type, and giant polyoxometalates were studied in Chapter 2, 3, 4, and 5, respectively. In detail, Chapter 2 describes using TiO_2 and α-Keggin type Polyoxometalate co-catalysts in a photo-electrochemical system to boost the oxidation rate of methanol. Comparisons of co-catalysts system in the dark and under illumination, as well as single catalyst under light conditions were performed. The dependence of polyoxometalate concentrations, pH values, and polyoxometalate types was studied. In Chapter 3, positively charged poly-(diallyl-dimethyl-

ammonium)-stabilized Au nanoparticles and negatively charged Cobalt substituted α_2-Wells-Dawson-polyoxometalate ($CoP_2W_{17}O_{61}^{8-}$) were employed to prepare Au nanoelectrode arrays. And CuI, CdS and CdTe semiconductor thin films were synthesized onto the surface of Au nanoparticles using electrochemical codeposition and electrochemical atomic layer deposition (EC-ALD). The Au-semiconductor core-shell nanoparticles were characterized by electrochemistry, photoluminescence spectroscopy, Raman spectroscopy, and Mott-Schottky analysis using capacitance data from electrochemical impedance spectroscopy. Chapter 4 deals with dual-functional aspect of polyoxometalates in photosynthesis of Ag nanoparticles. The Ag nanoparticles prepared by simple α-Keggin-type polyoxometalate ($PW_{12}O_{40}^{3-}$) and sandwich type polyoxometalate ($[WZn_3(H_2O)_2(ZnW_9O_{34})_2]^{12-}$) are characterized by UV-vis, TEM and Dynamic light Scattering. The discrete size distribution of Ag nanoparticles is discussed. Chapter 5 presents a degradation phenomenon of giant Keplerate type mixed valence polyoxometalate $Mo^{VI}_{72}Mo^{V}_{60}O_{372}(CH_3COO)_{30}(H_2O)_{72}]^{42-}$ catalyzed by Cu^{2+}. The degradation is monitored by UV-vis spectroscopy. The decomposition of $Mo^{VI}_{72}Mo^{V}_{60}O_{372}(CH_3COO)_{30}(H_2O)_{72}]^{42-}$ is not sensitive to other divalent metal cations such as Co^{2+} and Ni^{2+}. Chapter 6 provides a brief conclusion of this research and recommendations for further research.

References

(1) http://www.energy.gov/energysources/fossilfuels.htm.

(2) Appleby, A. J., Electrocatalysis and fuel cells; *Catalysis Reviews* **1970**, 4, (2), 221-243.

(3) Smarsly, B.; Kaper, H., Liquid inorganic-organic nanocomposites: Novel electrolytes and ferrofluids.; *Angew. Chem. Int. Ed.* **2005**, 44, (25), 3809-3811.

(4) Savadogo, O., Chemically and electrochemically deposited thin films for solar energy materials.; *Solar Energy Materials and Solar Cells* **1998**, 52, (3-4), 361-368.

(5) Pope, M. T., *Heteropoly and Isopoly Oxometalates*; Springer-Verlag, 1983.

(6) Pope, M. T.; Müller, A., *Polyoxometalate Chemistry From Topology via Self-Assembly to Applications*; Kluwer Academic Publishers, 2002.

(7) Müller, A.; Serain, C., Soluble Molybdenum Blues “des Pudels Kern”; *Acc. Chem. Res.* **2000**, 33, (1), 2-10.

(8) Berzelius, J. J., Beitrag zur näheren Kenntniss des Molybdäs.; *Poggend. Ann. Phys. Chem.* **1826**, 6, 368-392.

(9) Galissard de Marignac J.-C.; *Ann. Chim. Phys.* **1864**, 4^{e} série, (3), 1.

(10) Werner, A., Untersuchungen über anorganische Konstitutions- und Konfigurations-Fragen; *Berichte der deutschen chemischen Gesellschaft* **1907**, 40, (1), 15-69.

(11) Miolati, A.; Pizzighelli, R., Zur Kenntnis der komplexen Säuren I. 1. Über die Leitfähigkeit von molybdänsäurehaltigen Gemischen; *Journal für Praktische Chemie* **1908**, 77, (1), 417-456.

(12) Baker, L. C. W.; Glick, D. C., Present General Status of Understanding of Heteropoly Electrolytes and a Tracing of Some Major Highlights in the History of Their Elucidation; *Chem. Rev.,* **1998**, 98, (1), 3-50.

(13) Pauling, L. C., The molecular structure of the tungstosilicates and relate compounds; *J. Am. Chem. Soc.* **1929**, 51, (10), 2868-2880.

(14) Keggin, J. F., Structure of the Molecule of 12-Phosphotungstic; *Nature* **1933**, 131, 908-909.

(15) Souchay, P.,Contribution à l'étude des hétéropolyacides tungstiques; PhD Thesis, Université De Paris, Paris, France 1945.

(16) Souchay, P.; *Annales de chimie* **1943**, 19, 102.

(17) Souchay, P., polarographie des polyanions; *Talanta* **1965**, 12, (12), 1187-1209.

(18) Souchay, P., *Polyanions et Polycations*; Gauthier-Villars: Paris, France, 1963.

(19) Souchay, P., *Ions minéraux condensés*; Masson & Cie: Paris France, 1969.

(20) Souchay, P.; Lefebvre, J., *Équilibres et Réactivité des Complexes en Solution*; Masson & Cie: Pari,s France, 1969.

(21) Pope, M. T.; Varga, G. M., Jr., Proton magnetic resonance of aqueous metatungstate ions. Evidence for two central hydrogen atoms; *Chem. Commun.* **1966**, (18), 653-654.

(22) Varga, G. M., Jr.; Papaconstantinou, E.; Pope, M. T., Heteropoly blues. IV. Spectroscopic and magnetic properties of some reduced polytungstates; *Inorg. Chem.* **1970**, 9, (3), 662-667.

(23) So, H.; Pope, M. T., Origin of some charge-transfer spectra. Oxo compounds of vanadium, molybdenum, tungsten, and niobium including heteropoly anions and heteropoly blues; *Inorg. Chem.* **1972**, 11, (6), 1441-1443.

(24) Pope, M. T.; O'Donnell, S. E.; Prados, R. A., Electron exchange between pairs of vanadium atoms in novel geometric isomers of heteropoly tungstates; *Adv. Chem. Ser.* **1976**, 150, (Inorg. Compd. Unusual Prop., Symp., 1975), 85-94.

(25) Leparulo-Loftus, M. A.; Pope, M. T., Vanadium-51 NMR spectroscopy of tungstovanadate polyanions. Chemical shift and line-width patterns for the identification of stereoisomers; *Inorg. Chem.* **1987**, 26, (13), 2112-2120.

(26) Kim, K.-C.; Pope, M. T., New plenary and lacunary polyoxotungstate structures assembled from nonatungstoarsenate(III) anions and uranyl cations; *J. Chem. Soc., Dalton Trans.* **2001**, (7), 986-990.

(27) Mbomekalle, I.-M.; Keita, B.; Lu, Y. W.; Nadjo, L.; Contant, R.; Belai, N.; Pope, M. T., Synthesis and electrochemistry of the monolacunary Dawson-type tungstoarsenate $[H_4AsW_{17}O_{61}]^{11-}$ and some first-row transition-metal ion derivatives; *Eur. J. Inorg. Chem.* **2004**, (20), 4132-4139.

(28) Khoshnavazi, R.; Eshtiagh-hosseini, H.; Alizadeh, M. H.; Pope, M. T., Syntheses and structural determination of new bis(9-tungstoarsenato)tris(dioxouranate(VI)) and its monooxovanadate(IV) derivative complexes; *Inorg. Chim. Acta* **2007**, 360, (2), 686-690.

(29) Dale, B. W.; Buckley, J. M.; Pope, M. T., Heteropoly-niobates and -tantalates containing manganese(IV); *J. Chem. Soc. A* **1969**, (2), 301-304.

(30) Pope, M. T., Heteropoly and isopolyanions as oxo complexes and their reducibility to mixed-valence blues; *Inorg. Chem.* **1972**, 11, (8), 1973-1974.

(31) Liu, J.; Liu, S.; Qu, L.; Pope, M. T.; Rong, C., Derivatives of the 21-tungsto-9-antimonate heteropolyanion. Part 1. Inclusion of lanthanide cations; *Transition Met. Chem.* **1992**, 17, (4), 311-313.

(32) Creaser, I.; Heckel, M. C.; Neitz, R. J.; Pope, M. T., Rigid nonlabile polyoxometalate cryptates $[ZP_5W_{30}O_{110}]^{(15-n)-}$ that exhibit unprecedented selectivity for certain lanthanide and other multivalent cations; *Inorg. Chem.* **1993**, 32, (9), 1573-1578.

(33) Liu, J.-F.; Chen, Y.-G.; Meng, L.; Guo, J.; Liu, Y.; Pope, M. T., Synthesis and characterization of novel heteropoly-tungstoarsenates containing lanthanides $[LnAs4W_{40}O_{140}]^{25-}$ and their biological activity; *Polyhedron* **1998**, 17, (9), 1541-1546.

(34) Sadakane, M.; Dickman, M. H.; Pope, M. T., Controlled assembly of polyoxometalate chains from lacunary building blocks and lanthanide-cation linkers; *Angew. Chem., Int. Ed.* **2000**, 39, (16), 2914-2916.

(35) Wassermann, K.; Pope, M. T., Large Cluster Formation through Multiple Substitution with Lanthanide Cations (La, Ce, Nd, Sm, Eu, and Gd) of the Polyoxoanion $[(B\text{-}\alpha\text{-}AsO_3W_9O_{30})_4(WO_2)_4]^{28-}$. Synthesis and Structural Characterization; *Inorg. Chem.* **2001**, 40, (12), 2763-2768.

(36) Zimmermann, M.; Belai, N.; Butcher, R. J.; Pope, M. T.; Chubarova, E. V.; Dickman, M. H.; Kortz, U., New Lanthanide-Containing Polytungstates Derived from the Cyclic

P_8W_{48} Anion: $\{Ln_4(H_2O)_{28}[K\subset P_8W_{48}O_{184}(H_4W_4O_{12})_2Ln_2(H_2O)_{10}]^{13-}\}_x$, Ln = La, Ce, Pr, Nd; *Inorg. Chem.* **2007**, 46, (5), 1737-1740.

(37) Pope, M. T.; Müller, A., Polyoxometalate Chemistry : An Old Field with New Dimensions in Several Disciplines; *Angew. Chem. Int. Ed.* **1991**, 30, (1), 34-38.

(38) Kepert, D. L., *The Early Transition Elements*; Academic Press: New York, 1972.

(39) Tézé, A.; Hervé, G., Relationship between structures and properties of undecatungstosilicate isomers and of some derived compounds; *J. Inorg. Nucl. Chem.* **1977**, 39, (12), 2151-2154.

(40) Pope, M. T.; O'Donnell, S. E.; Prados, R. A., Identification of stereoisomers of mixed heteropoly anions. Mixed valence and triplet state electron spin resonance spectra of vanadium(IV); *J. Chem. Soc., Chem. Commun.* **1975**, (1), 22-23.

(41) Kozhevnikov, I.; Roberts, S. M., *Catalysis by polyoxometalates*; John Wiley and Sons, 2002.

(42) Kehrmann, F., Zur Kenntnis der komplexen anorganischen Säuren. III. Abhandlung; *Zeitschrift für anorganische Chemie* **1892**, 1, (1), 423-441.

(43) Dawson, B., The structure of the 9(18)-heteropoly anion in potassium 9(18)-tungstophosphate, $K_6(P_2W_{18}O_{62}).14H_2O$; *Acta Cryst.* **1953**, 6, (2), 113-126.

(44) Weakley, T. J. R.; Evans, H. T.; Showell, J. S.; Tourné, G. F.; Tourné, M. C. M., 18-Tungstotetracobalto(II)diphosphate and related anions: a novel structural class of heteropolyanions; *J. Chem. Soc., Chem. Commun.* **1973**, (4), 139-140.

(45) Neumann, R.; Khenkin, A. M., Noble Metal (Ru^{III}, Pd^{II}, Pt^{II}) Substituted "Sandwich" Type Polyoxometalates: Preparation, Characterization, and Catalytic Activity in Oxidations of Alkanes and Alkenes by Peroxides; *Inorg Chem* **1995**, 34, (23), 5753-5760.

(46) Neumann, R.; Dahan, M., Molecular Oxygen Activation by a Ruthenium-Substituted "Sandwich" Type Polyoxometalate; *J. Am. Chem. Soc.* **1998**, 120, (46), 11969-11976.

(47) Neumann, R.; Dahan, M., Ruthenium substituted Keggin type polyoxomolybdates: synthesis, characterization and use as bifunctional catalysts for the epoxidation of alkenes by molecular oxygen; *Polyhedron* **1998**, 17, (20), 3557-3564.

(48) Neumann, R.; Dahan, M., A ruthenium-substituted polyoxometalate as an inorganic dioxygenase for activation of molecular oxygen; *Nature* **1997**, 388, (6460), 353-355.

(49) Hall, N., Bringing inorganic chemistry to life; *Chem. Commun.* **2003**, 803-806.

(50) Müller, A.; Krickemeyer, E.; Meyer, J.; Bogge, H.; Peters, F.; Plass, W.; Diemann, E.; Dillinger, S.; Nonnenbruch, F.; Randerath, M.; Menke, C., $[Mo_{154}(NO)_{14}O_{420}(OH)_{28}(H_2O)_{70}]^{(25 \pm 5)-}$: A Water-Soluble Big Wheel with More than 700 Atoms and a Relative Molecular Mass of About 24000; *Angew. Chem. Int. Ed.* **1995**, 34, (19), 2122-2124.

(51) Müller, A.; Krickemeyer, E.; Bögge, H.; Schmidtmann, M.; Peters, F., Organizational Forms of Matter: An Inorganic Super Fullerene and Keplerate Based on Molybdenum Oxide; *Angew. Chem. Int. Ed.* **1998**, 37, (24), 3360-3363.

(52) Müller, A.; Beckmann, E.; Bögge, H.; Schmidtmann, M.; Dress, A., Inorganic Chemistry Goes Protein Size: A Mo_{368} Nano-Hedgehog Initiating Nanochemistry by Symmetry Breaking; *Angew. Chem. Int. Ed.* **2002**, 41, (7), 1162-1167.

(53) Mizuno, N.; Misono, M., Heterogeneous Catalysis; *Chem. Rev.*, **1998**, 98, (1), 199-217.

(54) Ito, T.; Yashiro, H.; Yamase, T., Regular Two-Dimensional Molecular Array of Photoluminescent Anderson-type Polyoxometalate Constructed by Langmuir-Blodgett Technique; *Langmuir* **2006**, 22, (6), 2806-2810.

(55) Lehmann, J.; Gaita-Arino, A.; Coronado, E.; Loss, D., Spin qubits with electrically gated polyoxometalate molecules; *Nature Nanotechnology* **2007**, 2, 312-317.

(56) Gaspar, A. R.; Gamelas, J. A. F.; Evtuguin, D. V.; Neto, C. P., Alternatives for lignocellulosic pulp delignification using polyoxometalates and oxygen: a review; *Green Chem.* **2007**, 9, 717-730.

(57) Rhule, J. T.; Hill, C. L.; Judd, D. A.; Schinazi, R. F., polyoxometalates in medicine; *Chem. Rev.*, **1998**, 98, (1), 327-357.

(58) Appleby, A. J., *Comprehensive Treatise of Electrochemistry*; Plenum Press, 1983; Vol. 8.

(59) Sadakane, M.; Steckhan, E., Electrochemical Properties of Polyoxometalates as Electrocatalysts; *Chem. Rev.*, **1998**, 98, (1), 219-237.

(60) Hill, C. L.; Prosser-McCartha, C. M., Homogeneous catalysis by transition metal oxygen anion clusters *Coordination Chemistry Reviews* **1995**, 143, 407-455.

(61) Altenau, J. J.; Pope, M. T.; Prados, R. A.; So, H., Models for heteropoly blues. Degrees of valence trapping in vanadium(IV)- and molybdenum(V)-substituted Keggin anions; *Inorg Chem* **1975**, 14, (2), 417-421.

(62) Ortéga, F.; Pope, M. T.; Howard T. Evans, J., Tungstorhenate Heteropolyanions. 2. Synthesis and Characterization of Enneatungstorhenates(V), -(VI), and -(VII); *Inorg. Chem.*, **1997**, 36, (10), 2166-2169.

(63) Ortega, F.; Pope, M. T., Polyoxotungstate anions containing high-valent ruhenium. 1. Keggin anion derivatives; *Inorg Chem* **1975**, 23, (21), 3292-3297.

(64) Romo, S.; Fernandez, J. A.; Maestre, J. M.; Keita, B.; Nadjo, L.; de Graaf, C.; and Poblet, J. M. Density Functional Theory and ab Initio Study of Electronic and Electrochemistry Properties of the Tetranuclear Sandwich Complex $[Fe^{III}_4(H_2O)_2(PW_9O_{34})_2]^{6-}$ *Inorg Chem* **2007**, 46, (10), 4022-4027.

Chapter 2.

Investigation of the Photocatalytic Activity of TiO_2–Polyoxometalate Systems for the Oxidation of Methanol

2.1 Introduction

2.1.1 Direct methanol fuel cell

Fuel cells are environmentally benign and versatile alternative power sources that are currently under active development. Fuel cells consume reactant from an external source, which can be replenished continuously, making them a thermodynamically open system. In contrast, electrochemical cell batteries store electrical energy chemically inside the batteries and hence represent a thermodynamically closed system. Fuel cells can produce electricity from fuel and an oxidant. Many combinations of fuels and oxidants are possible. A hydrogen fuel cell uses hydrogen as its fuel and oxygen (usually from air) as its oxidant. Other fuels include hydrocarbons and alcohols. Other oxidants include chlorine and chlorine dioxide.

There are two types of fuel cells using methanol as fuels. One is Direct Methanol Fuel Cell (DMFC), in which the methanol fuels are fed directly to the fuel cell. The other one is Reformed Methanol Fuel Cell (RMFC) or Indirect Methanol Fuel Cell (IMFC), in

which methanol fuels are reformed to H_2 before being fed into the device. In a DMFC, methanol is oxidized in the presence of water to produce CO_2 and protons at the anode. Electrons flow through the external circuit while hydrogen ions cross a proton exchange membrane (PEM) to combine with oxygen at the cathode to form water, as shown in Figure 2.1.

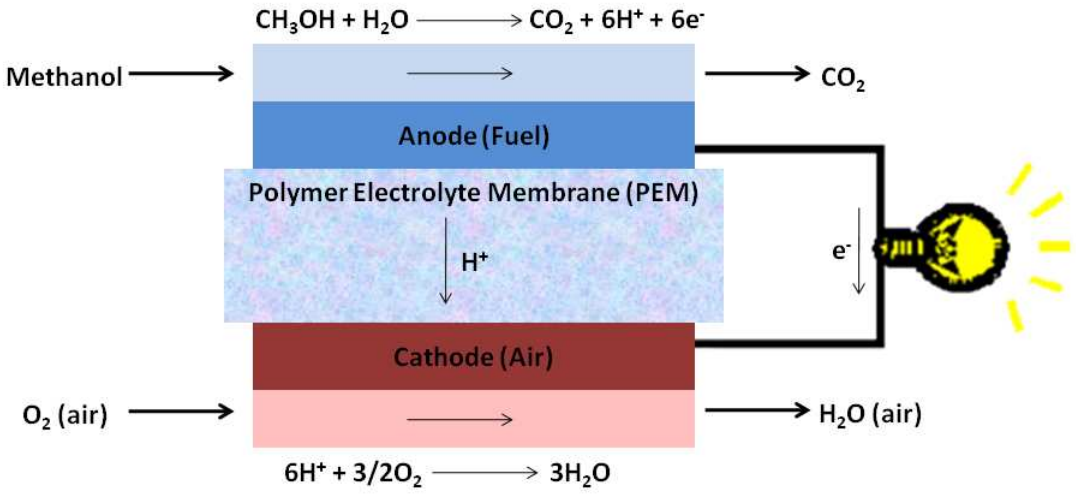

Figure 2.1 Schematic structure of Direct Methanol Fuel Cell (DMFC)

In direct methanol fuel cell, steam reforming is not required. Storage and transportation of methanol is much safer and easier than that of hydrogen as methanol does not need high pressures or low temperatures, because methanol is a liquid under normal pressure and room temperature. What's more, the energy density of methanol is an order of magnitude greater than even highly compressed hydrogen. Combining the three factors discussed above, Direct Methanol Fuel Cell (DMFC) can achieve very small device size comparable to conventional

batteries, making them ideal for consumer goods such as mobile phones, digital cameras or laptops.

Existing DMFC technologies are mainly limited by two factors. One is low cell voltage, which restricts them from high-power applications. The other limiting factor comes from the catalysts. The use of precious metals such as platinum in both the anode and cathode makes DMFC expensive. Carbon monoxide is an inevitable intermediate product during methanol oxidation. Thus the poisoning of the catalyst by CO adsorption is inevitable, leading to low catalytic efficiency.

2.1.2 TiO_2 in DMFC

Several strategies have been explored in an attempt to improve the overall efficiency of DMFCs. For example, efforts have been made to minimize the use of Pt in the catalyst either by increasing the electrode surface area or by exploring alternative catalyst materials[1]. More recently, several groups have looked into ways of incorporating photocatalysts such as TiO_2 on the anode side of the DMFC to further improve device performance and reduce the amount of precious metals in the catalyst. The use of photons to boost DMFC performance may be practical in applications where the fuel cell is operated outdoors under ambient illumination. In such a hybrid device, UV photons absorbed by the TiO_2 would generate electron–hole pairs by promotion of an electron from the valence band to the conduction band of the Titanium dioxide[2]. If the electrons can be collected efficiently, thereby minimizing the rate of electron–hole recombination, the holes can be used to carry out oxidative chemistry. This basic approach has

been used successfully for many years to oxidize methanol at wide band gap semiconductors using UV irradiation[3-9], for CO_2 fixation[10], and for the remediation of environmental pollutants[11].

Electron–hole recombination is always a critical issue in the efficiency of TiO_2 photocatalyst systems, regardless of the application. The solution to this problem has typically been to use a sacrificial oxidant, such as dioxygen, to scavenge the photogenerated conduction band electrons, but this is not always an efficient process[12]. Another approach is to adsorb the TiO_2 photocatalyst directly onto the surface of an electrode where the electrons can be collected by applying a suitable voltage. Kamat and co-workers recently have shown that such an approach is workable in principle in a hybrid Direct Methanol Fuel Cell[13]. These workers deposited TiO_2 particles onto an anode formed from carbon fibers and showed that photocurrents arising from the photooxidation of methanol could indeed be collected. Interestingly, improved performance in the dark was also observed, which might be due to the mitigation of poisoning effects by adsorbed TiO_2. A possible drawback to this approach, however, is that there must be a robust electrical contact between the anode and the photocatalyst. For example, if there is any kinetic barrier existing at the junction between the anode and the TiO_2, the electron collection efficiency of the anode will be reduced and device performance will suffer due to increased electron–hole recombination rates in the semiconductor.

An alternative approach would be to employ an electron scavenger such as a polyoxometalate (POM) to transport electrons from suspended TiO_2 particles in the supporting electrolyte to the anode. This would offer the additional advantage of being able to turn over a larger fraction of the incident photons by using more TiO_2 than could be directly adsorbed onto the surface of the anode. The ability of polyoxometalates to accept electrons readily has been known for many years. Upon chemical or electrochemical reduction, many polyoxometalates

form stable, highly colored mixed-valence species generically termed 'heteropoly blues'[14,15]. Ozer and Ferry have investigated the use of POMs such as $PW_{12}O_{40}^{3-}$, $SiW_{12}O_{40}^{4-}$, and $W_{10}O_{32}^{4-}$ to facilitate the transfer of photogenerated TiO_2 conduction band electrons to dioxygen as a means of increasing the efficiency of the photodegradation of 1,2-dichlorobenzene[16]. Using TiO_2–POM mixed systems, these workers observed an eight-fold increase in the apparent degradation rate of 1,2-dichlorobenzene compared to TiO_2 alone. Zhao and co-workers have reported similar findings, but also discovered that different product distributions can result when using TiO_2 alone or in tandem with POMs[17]. POM systems have also been shown to be viable in fuel cell applications. For instance, Dumesic and co-workers have demonstrated that it is possible to use polyoxometalates such as $PMo_{12}O_{40}^{3-}$ to drive a fuel cell by oxidizing CO to CO_2, thus bypassing the water gas shift reaction[18]. Electrons were stored in the form of reduced polyoxometalate $PMo_{12}O_{40}^{5-}$ and later collected at a gold electrode.

With these results in mind, we decided to investigate the possibility of using POMs to catalyze the transfer of photogenerated electrons in TiO_2 to a Pt anode in an electrochemical cell. The operation of these 'soluble photoanodes' as a component of a DMFC is illustrated in Figure 2.2.

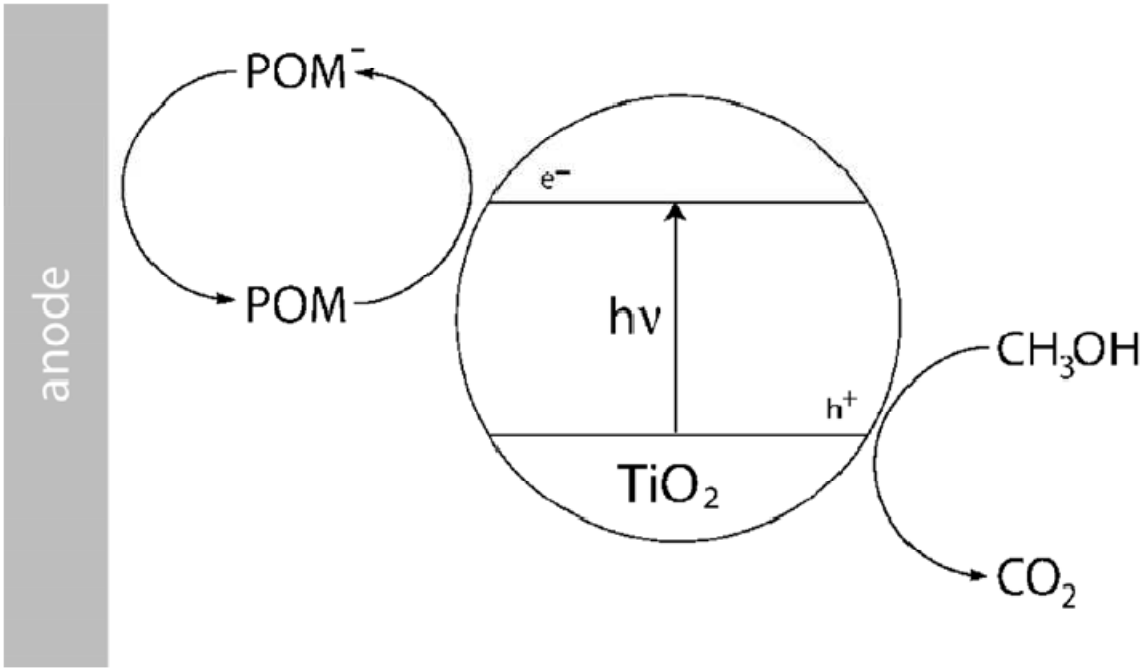

Figure 2.2 POM-mediated electron transfer from the conduction band of TiO_2 to a Pt anode. Taken from Ref. 30 with permission.

In this study, we employed a simple α-Keggin-type polyoxometalate ($Na_3PW_{12}O_{40}$) to scavenge electrons from photoexcited TiO_2 particles suspended in solution. The reduced polyoxotungstates were subsequently oxidized back to the parent Keggin complex at the Pt anode, resulting in a photocurrent. And the recycled parent $PW_{12}O_{40}^{3-}$ can perform the electron mediation again. By using a POM to collect and store photogenerated electrons from TiO_2, we have observed a 50-fold increase in the methanol oxidation photocurrent as compared to the use of TiO_2 alone. Indeed, the photocurrent densities we measured were higher than those reported by Kamat and co-workers[13] due to higher light accepting areas.

2.2 Experimental

2.2.1 Materials and reagents

TiO_2 powder (Degussa P-25), with an anatase to rutile ratio of 8:2, a surface area of $50 m^2/g$ and average particle diameter of 30 nm, was used as received without further purification. Methanol (99.9%, Fisher Chemical), perchloric acid (Fisher Chemical) with a nominal composition of 69–72% $HClO_4$, acetic acid (Fisher Chemical), formic acid (Fisher Chemical), and $Na_3PW_{12}O_{40}$ (>99.9%, Sigma–Aldrich) were used as received without further purification. Millipore-Q purified distilled water (18MΩ·cm) was used to clean electrodes and make up all solutions.

2 2.2 Electrode preparation

Pt electrodes were cleaned by rinsing sequentially with distilled water, absolute ethanol, piranha solution (1:3 (v/v) 30% H_2O_2, 18M H_2SO_4), distilled water, and absolute ethanol. After being dried in a stream of flowing nitrogen, the clean Pt was annealed in a H_2 flame for several minutes. The cleanliness of the Pt electrodes was verified by cyclic voltammetry prior to making measurements.

2.2.3 Photoelectrochemistry

Photoelectrochemical measurements were carried out in a Rayonet Photochemical reactor (RPR-100, Southern New England Ultraviolet Company) equipped with RPR 3500 lamps (ca. 500 $\mu W/cm^2$ for λ = 350 nm). The temperature inside the reactor was maintained at 35 °C with a cooling fan in operation. A 20mL vessel made of Pyrex glass was used as the

photoelectrochemical cell. A schematic diagram of the whole experimental setup is shown in Figure 2.3. The photoelectrochemical cell was put in the center of the Photochemical reactor so that it can absorb UV-irradiation from all directions.

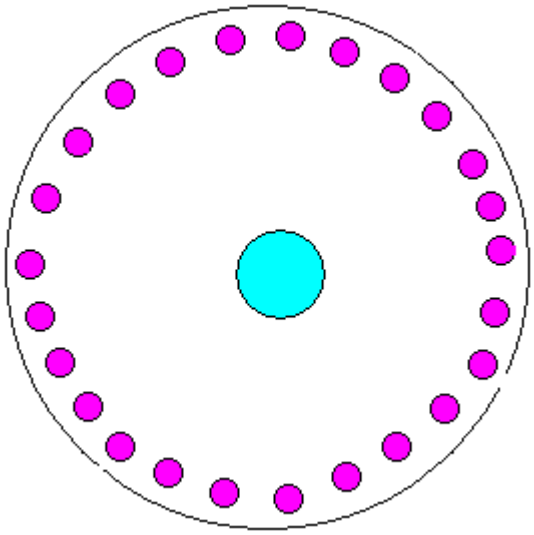

Figure 2.3 Schematic diagram of experimental setup. Blue: photoelectrochemical cell. Purple: UV-lamps with lamps λ_{max} = 350 nm

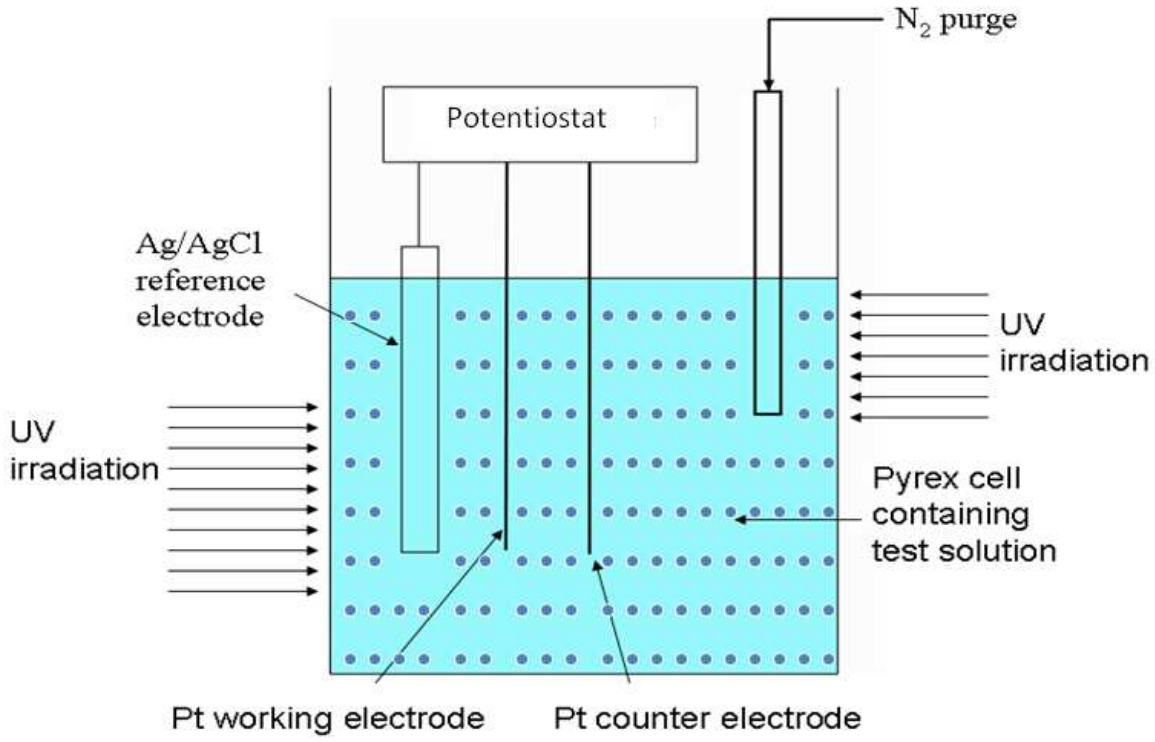

Figure 2.4 Photoelectrochemical cell setup. Blue dots: TiO_2 particles

The electrochemical measurements were performed using a conventional three electrode setup, as shown in Figure 2.4. Titanium dioxide particles were dispersed all over the solution to maximize the UV irradiation area. The pH of the reaction suspension/solution was adjusted to 1.0 before reaction (after the addition of $Na_3PW_{12}O_{40}$). A platinum flag electrode (approximately 0.77 cm^2), a Ag|AgCl (sat) electrode and a platinum gauze electrode were used as the working, reference, and counter electrodes, respectively. Nitrogen gas (>99.9%) was used to purge the suspension during the experiment. The Pt anode was held at a potential of +0.60V versus Ag|AgCl(sat) to measured the generated photocurrent. The potential of the working electrode

was controlled using a potentiostat (Pine Instruments, AFRDE-4) connected to a computer. Data was acquired using Lab View.

2.3 Results and discussion

2.3.1 Photocurrent

Representative photocurrent–time data for a series of four experiments are presented in Figure 2.5. In all cases, the concentration of methanol was fixed at 0.2M and the pH was adjusted to a value of 1.0 using perchloric acid, which also served as the supporting electrolyte. The solutions were rigorously purged with N_2 prior to all experiments and N_2 was flowed continuously through the photoelectrochemical cell during data acquisition to prevent reaction of the reduced POMs with dioxygen. The anode (Pt, 0.077 cm^2 geometrical surface area) was poised at a potential of 0.6V versus Ag|AgCl(sat) to ensure efficient collection of the reduced POM. In the first experiment, Figure 2.5D, a solution containing 1mM POM and 0.05 mg/mL TiO_2 was held at a potential of 0.6V in the dark. The data clearly indicated that there was no significant electrochemical oxidation of any of the solution components occurs under these experimental conditions.

We then performed an experiment in which a 0.2M CH_3OH + 0.1M $HClO_4$ solution containing 0.05 mg/mL TiO_2 but no POM was irradiated at 350 nm. This concentration of TiO_2 was chosen to ensure that there was no significant settling of particles during the course of the experiment. Typical data are shown in Figure 2.5C and are characterized by a very slow increase of current as a function of time over the course of many hours. We estimated the steady state photocurrent to be about 0.81$mA \cdot cm^{-2}$ for this experiment. The low photocurrents measured

under these experimental conditions are a result of the poor efficiency of photo-oxidation processes in the absence of an electron scavenger.

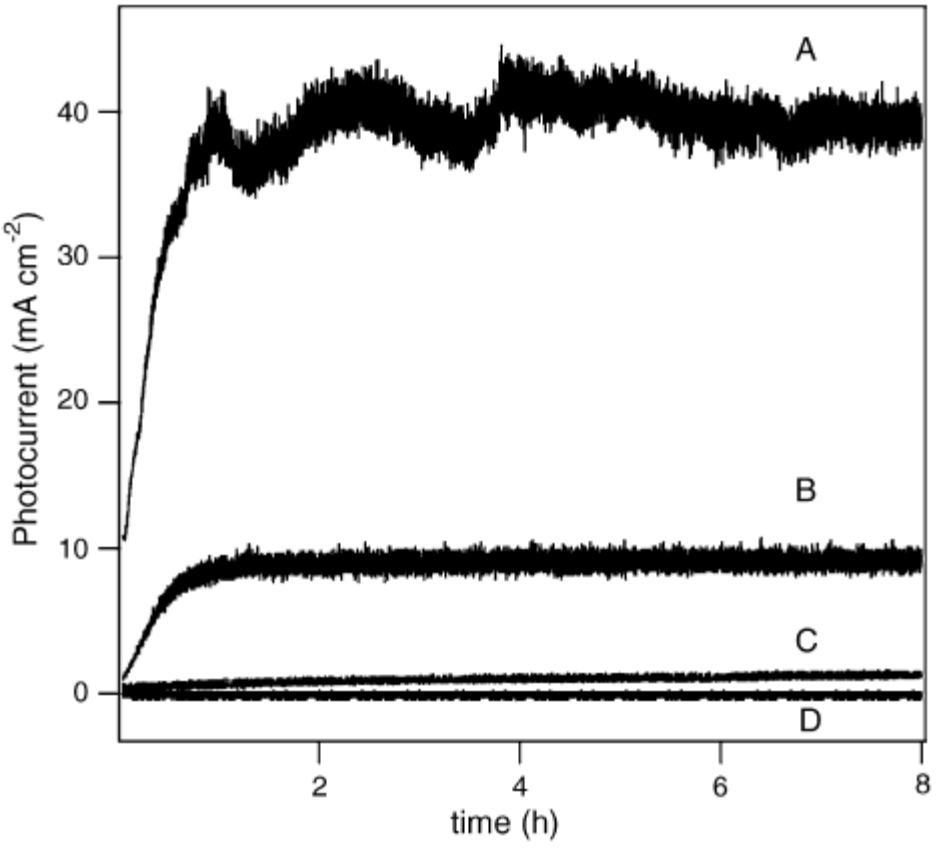

Figure 2.5 Photocurrent vs. time plots for samples irradiated at 350 nm. (A) 0.2M CH_3OH + 0.1M $HClO_4$ solution with 0.05 mg/mL TiO_2 and 1mM $PW_{12}O_{40}^{3-}$. (B) 0.2M CH_3OH + 0.1M $HClO_4$ solution with 1mM $PW_{12}O_{40}^{3-}$ (no TiO_2). (C) 0.2M CH_3OH + 0.1M $HClO_4$ solution with 0.05 mg/mL TiO_2 (no POM). (D) 0.2M CH_3OH + 0.1M $HClO_4$ solution with 0.05 mg/mL TiO_2 and 1mM $PW_{12}O_{40}^{3-}$ in the dark. Taken from Ref. 30 with permission.

Next, we carried out an experiment in which a 0.2M CH_3OH + 0.1M $HClO_4$ solution was irradiated in the presence of 1mM $PW_{12}O_{40}^{3-}$, Figure 2.5B. In this experiment, the photocurrent increased rapidly and monotonically over the course of the first hour or so of irradiation at 350 nm, finally reaching a steady state value of 9.0mA·cm^{-2} after about 2 hours. Interestingly, the steady-state photocurrent we observed in this experiment is significantly larger than in the case of TiO_2 alone. This result provides clear experimental evidence that the $PW_{12}O_{40}^{3-}$ anion itself displays significant photocatalytic activity toward methanol oxidation, consistent with previous research on the photooxidation of alcohols by polyoxometalates[19]. Furthermore, our observation that $PW_{12}O_{40}^{3-}$ is a better photocatalyst than TiO_2 in the absence of O_2 parallels the results reported by Hill and Chambers, who compared the ability of semiconductor- and polyoxometalate-based photocatalysts to photodegrade a series thioethers[20]. In addition, the solution was observed to turn blue under UV irradiation, indicating the formation of a significant concentration of reduced polyoxometalate. Finally, when methanol was replaced with either acetic acid or formic acid, no color change was observed and no significant photocurrents were detected at the Pt anode.

The reason that a photocurrent is observed when methanol is used as the substrate but not in the other cases is that while the oxidized form of the polyoxometalate can oxidize methanol, it is not able to oxidize either formic acid or acetic acid under our experimental conditions. There is some debate in the literature about the exact nature of the POM that facilitates electron transfer to the anode. On one hand, Park and Choi claim that both ground state and excited state polyoxometalate can serve as effective electron acceptors[21]. In their view, photoexcited polyoxometalates can accept an electron from a donor species in solution to produce POM^-, which can then be oxidized back to polyoxometalate at the anode. Photocurrent data obtained by

these workers from solutions containing polyoxometalate alone and compared to data from solutions containing mixtures of polyoxometalate and TiO_2 appear to bear this out. On the other hand, Ozer and Ferry assert that the electron mediator is exclusively ground state polyoxometalate, presumably on the basis of the weak absorption of the polyoxometalate at the narrower band of wavelengths region used in their experiments[16]. Our results clearly show the ability of the photoexcited state of the polyoxometalates to oxidize methanol, although the oxidizing power of the polyoxometalate excited state holes does not match that of the photogenerated holes in TiO_2.

Finally, we irradiated a 0.2M CH_3OH + 0.1M $HClO_4$ solution that also contained 0.05 mg/mL TiO_2 and 1mM $PW_{12}O_{40}^{3-}$, as shown in Figure 2.5A. As in the previous experiments, the photocurrent increases almost linearly over the course of about two hours and then reaches a plateau value. In the case of the mixed TiO_2–POM system, however, the rate of increase of the photocurrent with respect to time appears to be somewhat greater than in the previous measurements. In this experiment, a steady state current of about 40mA·cm^{-2} was observed. This is about 50 times greater than the steady state photocurrent we observed for TiO_2 alone and about a factor of four greater than in the case of POM alone. As before, the solution turned blue upon irradiation, demonstrating that reduced polyoxomtalates are formed. When methanol is replaced with either acetic acid or formic acid, photocurrents similar to those previously reported by Park and Choi were observed[21]. These findings confirm our earlier assertions about the oxidizing power of the photoexcited POM as compared to TiO_2. Taken together, our observations are consistent with a mechanism whereby methanol is oxidized by the TiO_2 excited state as shown in Figure 2.2. Mechanisms proposed for Figure 2.5 A, B and C is shown in Figure 2.6.

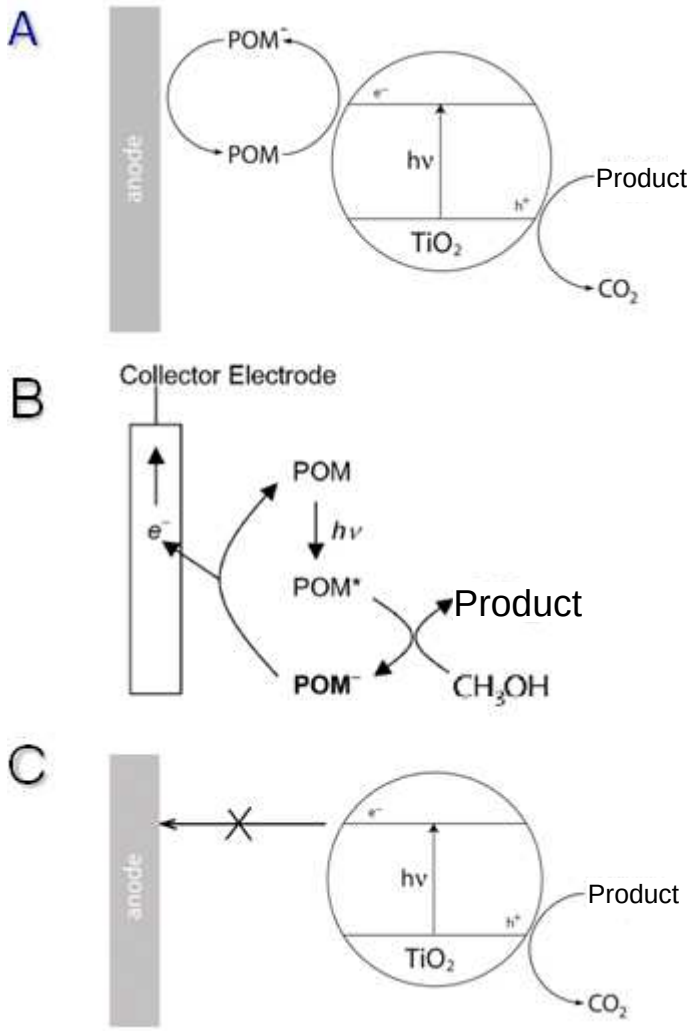

Figure 2.6 Proposed mechanisms for Figure 2.5 A, B and C

Even though we tried to get rid of interference of O_2 by Nitrogen gas purging in our system, we still cannot rule out the existence of other, parallel reaction pathways and products, such as the formation of formaldehyde[22]. In a similar POM system, Fox et al. showed that, in the presence of dioxygen, methanol is oxidized to formaldehyde using phosphotungstate photocatalysts[23].

2.3.2 Polyoxometalate concentration dependence

Perhaps most importantly, however, the blue color of the solution persists for several minutes after the light is turned off. This observation is an unambiguous demonstration of the fact that the conduction band electrons from photoexcited TiO_2 are scavenged so efficiently by the POM that the rate of oxidation of reduced POM^- at the anode now represents the kinetic bottleneck in the system. The highly efficient electron transfer from the conduction band of TiO_2 to POM is in great part due to the fact that POMs such as $PW_{12}O_{40}^{3-}$ adsorb strongly to the surface of TiO_2 particles, which are positively charged at pH 1. As noted earlier, Ozer and Ferry compared a series of POMs to dioxygen as electron scavengers in the photodegradation of 1,2-dichlorobenzene using TiO_2 suspensions under UV irradiation[16]. The binding constants between the electron acceptor (either dioxygen or POM) and TiO_2 correlated reasonably well with the Langmuir–Hinshelwood kinetic data that they measured for 1,2-dichlorobenzene decomposition. Specifically, by assuming a Langmuir adsorption isotherm, the binding constants for $PW_{12}O_{40}^{3-}$ and O_2 adsorption on TiO_2 surface at pH 1 were found to be 467 and 84.6M^{-1}, respectively, a ratio of 5.5:1. The apparent rate constants for 1,2-dichlorobenzene degradation were reported to be 0.638 and 0.0818 min^{-1}, a ratio of 7.8:1. More recently, Zhao and coworkers have carried out a detailed mechanistic study of the TiO_2−$PW_{12}O_{40}^{3-}$ system as it pertains to the photodegradation of organic compounds[17]. These workers measured the adsorption of $PW_{12}O_{40}^{3-}$ onto TiO_2 under conditions similar to those of Ferry et al. using similar experimental methods. However, the binding constant reported by these workers is 7.1×10^4 m^{-1}, which is more than two orders of magnitude greater than that reported by Ferry and co-workers. It should be noted that accurate measurement of Langmuir adsorption parameters can be notoriously difficult, especially in cases

where the kinetics of adsorption and/or desorption are slow, owing to the fact that the measurement system may not be at thermodynamic equilibrium. In addition, other factors, particularly ion pairing interactions, are expected to play a critical role in the adsorption of POM on the TiO_2 surface, and these effects will be strongly dependent on the nature of the supporting electrolyte[24]. Another useful predictor of electron acceptor activity is the free energy change for the one electron reduction of the electron acceptor by TiO_2 conduction band electrons. The redox potential of $PW_{12}O_{40}^{3-}$ and the flatband potential of the TiO_2 (particle) conduction band are +0.218 and –0.189V versus NHE, respectively[25,26]. Thus, electron transfer between the conduction band of TiO_2 and $PW_{12}O_{40}^{3-}$ is thermodynamically favored by about 39 kJ/mol. It should be noted, however, that such arguments do not take into account many complicating factors that may be important in POM systems, including the diversity of electron acceptor states, the possibility that more than one electron may be transferred simultaneously and the fact that the acceptor and donor energy levels may be perturbed upon adsorption of polyoxometalate to TiO_2.

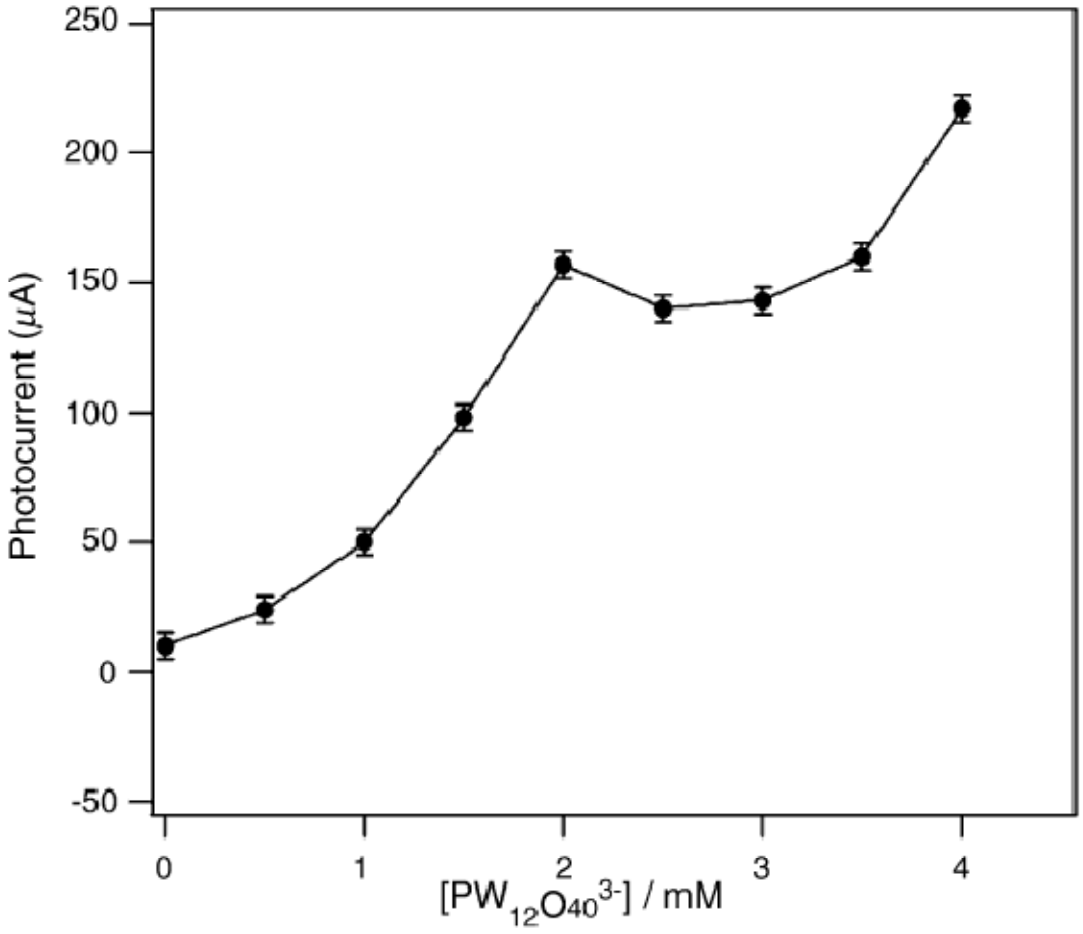

Figure 2.7 Dependence of the steady state photocurrent on [$PW_{12}O_{40}^{3-}$]. The filled circles are experimental data points, while the line is a guide to the eye. Taken from Ref. 30 with permission.

To further investigate the scavenging of electrons from photoexcited TiO_2 by $PW_{12}O_{40}^{3-}$, we performed concentration dependent studies in which [$PW_{12}O_{40}^{3-}$] was varied at a constant TiO_2 concentration of 0.05 mg/mL. As seen in Fig. 2.7, the steady state photocurrent increases with increasing POM concentration, reaching a maximum when [$PW_{12}O_{40}^{3-}$] is about 2 mM. At

higher [$PW_{12}O_{40}^{3-}$] , the steady state photocurrent decreases slightly, and then begins to increase again above ca. 3 mM. The observation of a local maximum suggests that interactions between the POM electron scavenger and the surface of the TiO_2 nanoparticles are important. Previous researchers have suggested that such behavior is due to competition between $PW_{12}O_{40}^{3-}$ and methanol for the finite number of surface sites on the TiO_2 particles[16]. Assuming a Langmuir adsorption isotherm, and using Ferry's previously reported binding constants, a POM concentration of 2mM corresponds to roughly 50% surface coverage.

Zhao and coworkers have reported behavior similar to what we have observed; however, they offer a different interpretation[17]. These workers suggest that at elevated [POM], POMs in solution act as an 'inner filter', absorbing a significant fraction of the incident UV, and effectively blocking that radiation from being absorbed by the TiO_2 particles. This model predicts that if TiO_2 particles become encapsulated by POM, the adsorbed POM would essentially behave as a local UV 'filter', resulting in a lower absorbance of UV irradiation by the TiO_2. This is not an entirely unreasonable possibility; for instance, it is well known that POMs readily adsorb to metal surfaces[27]. Nevertheless, such a filter effect seems not to be important in the case of methanol photooxidation, as evidenced by the increase of in steady state photocurrent when [$PW_{12}O_{40}^{3-}$] > 3 mM. This increase may be due to increased absorption of UV by the POM relative to the TiO_2 at these concentrations, leading to direct oxidation of methanol by the POM excited state.

2.3.3 pH dependence

Generally speaking, the electron mediation properties of polyoxometalates are greatly dependent on proton concentrations of surrounding media. To further investigate the scavenging of electrons from photoexcited TiO_2 by $PW_{12}O_{40}^{3-}$, we performed pH dependent studies at a constant TiO_2 concentration of 0.05 mg/mL and a constant $PW_{12}O_{40}^{3-}$ concentration of 1mM, as shown in Figure 2.8.

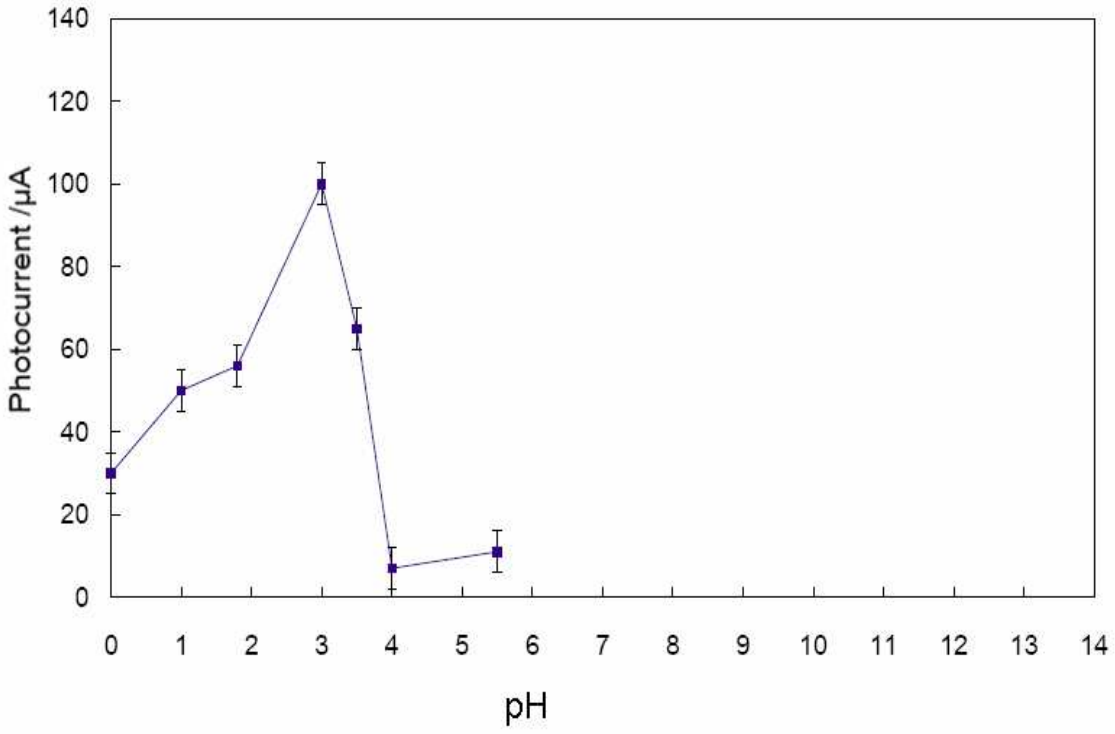

Figure 2.8 Dependence of the steady state photocurrent on pH. The filled squares are experimental data points, while the line is a guide to the eye.

The electron shuttling behavior of polyoxometalates between the conduction band of TiO_2 and the Pt anode can be broken down to two cycling sequential steps. The first step is that the POM gets an electron from the conduction band of TiO_2 and become reduced POM^-. This step favors a lower pH due to two factors. The $PW_{12}O_{40}^{3-}$ reduction works at highest speed when pH is close to 1. Thus this step works faster when pH is more close to 1. The TiO_2 surface is partial positively charged at lower pH, which will facilitate the electron transfer from the conduction band of TiO_2 to POM, as well. The second step is the reduced POM^- pass the electron back to the Pt anode, resulted in photocurrent and re-generation of the parent Keggin heteropolyanion, which can be used back in the polyoxometalate reduction step. The reduced polyoxometalates would be protonated thermodynamically at lower pH[28]. The protontation will decrease the charge density of the reduced POM, and as a result, slow down the rate of reduced POM^- reoxidation at the electrode. Another obvious explanation for the second step is that the $PW_{12}O_{40}^{3-}$ polyanion may start to decompose at higher pH, which is usually true for most keggin type polyoxometalates. Thus, the electron shuttling behavior of polyoxometalates between the conduction band of TiO_2 and the Pt anode is a balance of two reactions in favor of high and low pH respectively. A peak performance of the TiO_2-POM photoelectrochemical catalytic system is expected to be observed in between pH 1, where the POM reduction by the conduction band electron of TiO_2 is fastest, and pH 6, where the most basic environment that the polytungstate can withstand. Our experimental result, as shown in Figure 2.8, displays a peak photocurrent at around pH 3, which falls in the expectated region. The existence of peak performance confirms that the balance of two reactions in favor different pH. It should be noted that the photocurrent at the higher pH side of the peak is lower than the one at the lower pH side, suggesting that the

redox reversibility of $PW_{12}O_{40}^{3-}$ is gradually decreased at higher pH due to structural distortion or decomposition.

2.3.4 Electrothermodynamic Study

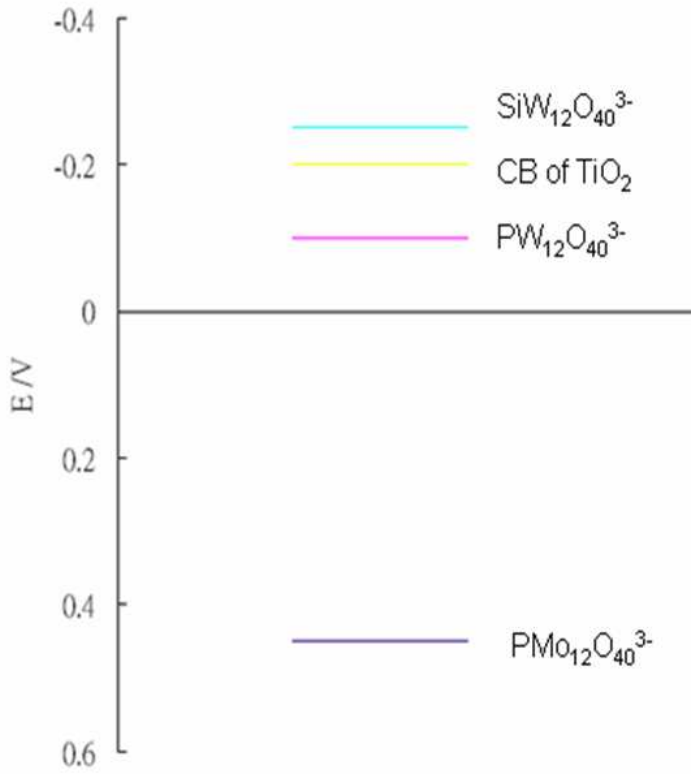

Figure 2.9 Comparison of E_0 of three different polyoxometalates and conduction band of TiO_2 vs Ag/AgCl

For better understanding of this TiO_2-POM co-catalytic system in methanol oxidation, $PW_{12}O_{40}^{3-}$ was substituted by two other different polyoxometalates, $SiW_{12}O_{40}^{3-}$ and $PMo_{12}O_{40}^{3-}$. The reason to choosing these two polyoxometalates is that they have similar size, molecular weight, charge density but dramatically different redox potential. Their redox potentials and the conduction band energy of TiO_2 are summarized in Figure 2.9.

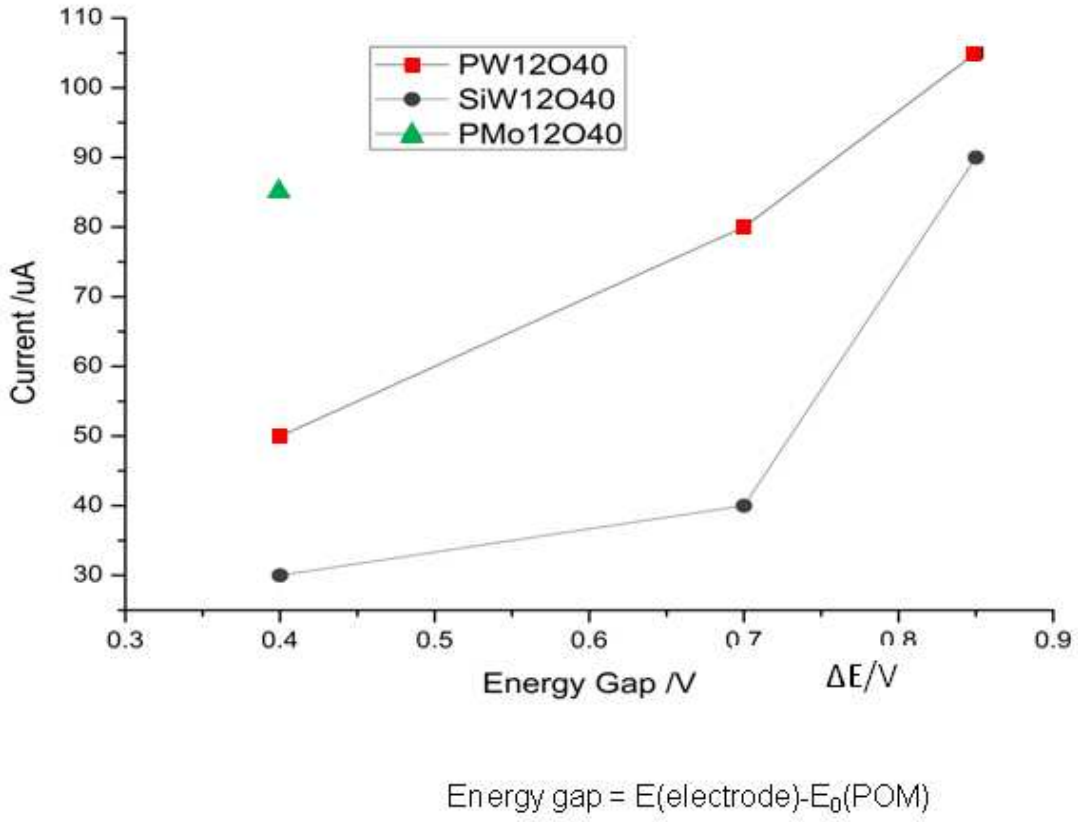

Figure 2.10 Photocurrent of TiO_2-POM co-catalytic system with different POMs and different applied potential on electrode.

It is predicted that the photocurrent produced by TiO_2−$SiW_{12}O_{40}^{3-}$ is smaller than the one by TiO_2−$PW_{12}O_{40}^{3-}$, while TiO_2−$PMo_{12}O_{40}^{3-}$ system can generate higher current density than TiO_2−$PW_{12}O_{40}^{3-}$. The redox potential of $SiW_{12}O_{40}^{3-}$ is negatively higher than the TiO_2 conduction band energy. Thus, electrons on TiO_2 conduction band have less probability the jump to $SiW_{12}O_{40}^{3-}$ polyanion. In contrast, the redox potential of $PW_{12}O_{40}^{3-}$ and $PMo_{12}O_{40}^{3-}$ are lower than the TiO_2 conduction band energy, which should result in higher photocurrent than $SiW_{12}O_{40}^{3-}$. And E^0 of $PMo_{12}O_{40}^{3-}$ is lower than the one of $PW_{12}O_{40}^{3-}$. As we have discussed in the previous paragraphs, the electron shuttling behavior of polyoxometalates between the conduction band of TiO_2 and the Pt anode can be broken down to 2 sequential steps. The first step is the POM get an electron from the conduction band of TiO_2 and become reduced POM^-. And the second step is the reduced POM^- pass the electron to the Pt anode, resulted in photocurrent and re-generation of the parent Keggin POM. Substituting the POM species with different redox potential is in fact manipulating the reaction speed of the first step. And we can also vary the potential applied on the anode to change the reaction speed of the second step. If we apply higher positive potential on the electrode, we get higher photocurrents, as shown in Figure 2.10. Please note that the data for $PMo_{12}O_{40}^{3-}$ have only one point because it would go into the potential region of hydrogen evolution if we increase the applied potential on electrode. If we keep the energy gap, which is defined as the difference between electrical voltage applied on the Pt anode and standard redox potential of the POM, constant, we can assume that the reaction rate of the second step are the same. Thus the intensities of photocurrents in that scenario are mainly related to the rate of the first step, the polyoxometalate reduction. We can predict that the intensity of photo current should be in the following order: $I_{photo}(PMo_{12}O_{40}^{3-}) > I_{photo}(PW_{12}O_{40}^{3-}) > I_{photo}(SiW_{12}O_{40}^{3-})$. Our results shown in Figure 2.10 have confirmed our

prediction. The assumption here we made is oversimplified. Several parameters, such as electrostatic attraction between reduced polyoxometalate and positively charged electrode, are not considered. However, the results based on this assumption are good enough to get qualitative conclusion.

2.4 Conclusions

We have developed a TiO_2–polyoxometalate co-catalyst system for use in a hybrid photo-electrochemical cell for the oxidation of methanol. Although the photocatalytic behavior of polyoxometalate and TiO_2 photocatalysts are nominally quite similar[29], the use of a co-catalyst dramatically improves the separation of photogenerated electron–hole pairs in suspended TiO_2 nanoparticles, leading to a 50-fold increase in the photocurrent compared to the use of TiO_2 alone. Thus, the problem of efficient electron transfer out of the conduction band of the semiconductor appears to have been solved in our co-catalyst system. The use of Pt(0) clusters to improve the rate of electron transfer to and from polyoxometalates has been explored by several groups[19]. Such a strategy might lead to improved electron transfer between the reduced polyoxometalates and the anode in our photoelectrochemical system and will be explored in future studies. There also appears to be an optimum concentration of $PW_{12}O_{40}^{3-}$ = 2 mM, probably result from the competition for limited surface site of TiO_2 between methanol and POM, above which direct oxidation of methanol by the photoexcited state of the polyoxometalate competes with the oxidation of methanol by TiO_2. A pH dependence study was also performed. The balance of two processes favoring low and high pH respectively result in an optimum pH value in the media. In our system, the optimum pH = 3. Thermodynamic experimental data

match theoretical predicted order, which also confirms the two-step electron shuttling mechanism.

References

(1) Chen, C. Y.; Yang, P.; Lee, Y. S.; Lin, K. F., Fabrication of electrocatalyst layers for direct methanol fuel cells *Journal of Power Sources* **2005**, 141, (1), 24-29.

(2) Grätzel, M., Photoelectrochemical cells; *Nature* **2001**, 414, 338-344.

(3) Oosawa, Y., Photocatalytic hydrogen evolution from an aqueous metanol solution over ceramics-electrocatalyst/ TiO_2; *Chemistry Letters* **1983**, 12, (4), 577-580.

(4) Fan, F. R. F.; Liu, H. Y.; Bard, A. J., Integrated chemical systems: photocatalysis at titanium dioxide incorporated into Nafion and clay; *J. Phys. Chem.* **1985**, 89, (21), 4418-4420.

(5) Sobczynski, A., Photoassisted hydrogen production from a methanol-water mixture on platinized Cr_2O_3-DOPED TiO_2; *J. Mol. Catal.* **1987**, 39, (1), 43-53.

(6) Ulmann, M.; Augustynski, J., The involvement of surface-bonded intermediates in the competitive photo-oxidation of methanol and hydroxyl ions at a TiO_2 electrode *Chem. Phys. Chem.* **1987**, 141, (1-2), 154-158.

(7) Micic, O. I.; Zhang, Y.; Cromack, K. R.; Trifunac, A. D.; Thurnauer, M. C., Photoinduced hole transfer from titanium dioxide to methanol molecules in aqueous solution studied by electron paramagnetic resonance; *J. Phys. Chem.* **1993**, 97, (50), 13284–13288.

(8) Yamakata, A.; Ishibashi, T.; Onishi, H., Electron- and Hole-Capture Reactions on Pt/TiO_2 Photocatalyst Exposed to Methanol Vapor Studied with Time-Resolved Infrared Absorption Spectroscopy; *J. Phys. Chem. B* **2002**, 106, (35), 9122–9125.

(9) Peller, J.; Wiest, O.; Kamat, P. V., Hydroxyl Radical's Role in the Remediation of a Common Herbicide, 2,4-Dichlorophenoxyacetic Acid (2,4-D); *J. Phys. Chem. A* **2004**, 108, (50), 10925–10933.

(10) Heleg, V.; Willner, I., Photocatalysed CO_2-fixation to formate and H_2-evolution by eosin-modified Pd–TiO_2 powders; *J. Chem. Soc., Chem. Commun.* **1994**, (18), 2113 - 2114.

(11) Calhoun, R. L.; Winkelmann, K.; Mills, G., Chain Photoreduction of CCl_3F Induced by TiO_2 Particles; *J. Phys. Chem. B* **2001**, 105, (40), 9739–9746.

(12) Navío, J. A.; Marchena, F. J.; Roncel, M.; Rosa, M. A. D. l., A laser flash photolysis study of the reduction of methyl viologen by conduction band electrons of TiO_2 and Fe-Ti oxide photocatalysts; *Journal of Photochemistry and Photobiology A: Chemistry* **1991**, 55, (3), 319-322.

(13) Drew, K.; Girishkumar, G.; Vinodgopal, K.; Kamat, P. V., Boosting Fuel Cell Performance with a Semiconductor Photocatalyst: TiO_2/Pt−Ru Hybrid Catalyst for Methanol Oxidation; *J. Phys. Chem. B* **2005**, 109, (24), 11851–11857.

(14) Pope, M. T., Polyoxo anions: synthesis and structure; *Compr. Coord. Chem. II* **2004**, 4, 635-678, 635 Plates.

(15) Hill, C. L., Polyoxometalates: Reactivity; *Compr. Coord. Chem. II* **2004**, 4, 679-759.

(16) Ozer, R. R.; Ferry, J. L., Investigation of the Photocatalytic Activity of TiO_2−Polyoxometalate Systems; *Environ. Sci. Technol.* **2001**, 35, (15), 3242–3246.

(17) Chen, C.; Lei, P.; Ji, H.; Ma, W.; Zhao, J.; Hidaka, H.; Serpone, N., Photocatalysis by Titanium Dioxide and Polyoxometalate/TiO_2 Cocatalysts. Intermediates and Mechanistic Study; *Environ. Sci. Technol.* **2004**, 38, (1), 329-337.

(18) Kim, W. B.; Voitl, T.; Rodriguez-Rivera, G. J.; Dumesic, J. A., Powering Fuel Cells with CO via Aqueous Polyoxometalates and Gold Catalysts; *Science* **2004**, 305, (5688), 1280-1283.

(19) Papaconstantinou, E., Photochemistry of polyoxometallates of molybdenum and tungsten and/or vanadium; *Chem. Soc. Rev.* **1989**, 18, (1), 1-31.

(20) Chambers, R. C.; Hill, C. L., omparative study of polyoxometalates and semiconductor metal oxides as catalysts. Photochemical oxidative degradation of thioethers; *Inorg Chem* **1991**, 30, (13), 2776–2781.

(21) Park, H.; Choi, W., Photoelectrochemical Investigation on Electron Transfer Mediating Behaviors of Polyoxometalate in UV-Illuminated Suspensions of TiO_2 and Pt/TiO_2; *J. Phys. Chem. B* **2003**, 107, (16), 3885–3890.

(22) Hill, C. L.; Prosser-McCartha, C. M. In *Photosensitization and Photocatalysis Using Inorganic and Organometallic Complexes*; Kalyanasundaram, K., Grätzel, M., Eds.; Kluwer Academic Publishers, Inc.: Dordrecht, Netherlands, 1993, p 307-326.

(23) Fox, M. A.; Cardona, R.; Gaillard, E., Photoactivation of metal oxide surfaces: photocatalyzed oxidation of alcohols by heteropolytungstates; *J. Am. Chem. Soc.* **1987**, 109, (21), 6347–6354.

(24) Grigoriev, V. A.; Cheng, D.; Hill, C. L.; Weinstock, I. A., Role of Alkali Metal Cation Size in the Energy and Rate of Electron Transfer to Solvent-Separated 1:1 $[(M^+)(\text{Acceptor})]$ ($M^+ = Li^+, Na^+, K^+$) Ion Pairs; *J. Am. Chem. Soc.* **2001**, 123, (22), 5292–5307.

(25) Akid, R.; Darwent, J. R., Heteropolytungstates as Catalysts for the Photochemical Reduction of Oxygen and Water; *J. Chem. Soc., Dalton Trans.* **1985**.

(26) Dimitrijevic, N. M.; Savic, D.; Micic, O. I.; Nozik, A. J., Interfacial electron-transfer equilibria and flatband potentials of .alpha.-ferric oxide and titanium dioxide colloids studied by pulse radiolysis; *J. Phys. Chem.* **1984**, 88, (19), 4278–4283.

(27) Barteau, M. A.; Lyons, J. E.; Song, I. K., Surface chemistry and catalysis on well-defined oxide surfaces: nanoscale design bases for single-site heterogeneous catalysts *J. Catal.* **2003**, 216, (1-2), 236-245.

(28) Sadakane, M.; Steckhan, E., Electrochemical Properties of Polyoxometalates as Electrocatalysts; *Chem. Rev.*, **1998**, 98, (1), 219-237.

(29) Hiskia, A.; Mylonas, A.; Papaconstantinou, E., Comparison of the photoredox properties of polyoxometallates and semiconducting particles; *Chem. Soc. Rev.* **2001**, 30, 62 - 69.

(30) Gu, C. and Shannon, C., Investigation of the photocatalytic activity of TiO_2–polyoxometalate systems for the oxidation of methanol, *J. Mol. Catal. A,* **2007,** 262, (1-2) 185-189.

Chapter 3.

Synthesis of Metal-Semiconductor Core-Shell Nanoparticles Using Electrochemical Surface-Limited Reactions

3.1 Introduction

3.1.1 Core-Shell nanoparticles

Core-shell nanoparticles refers to nanomaterials consisted of a core nanoparticles encapsulated by a thin shell of a second material. A wide range of chemical and physical properties can be realized in these systems depending on the choice of the two components. For example, a narrow band gap semiconductor nanoparticle can be capped with a wide gap material to prevent the formation of surface traps, leading to enhanced band edge luminescence in the core-shell system[1-6]. Alternatively, the shell material can be chosen to improve the chemical stability of the core, which is important for medical imaging applications[7,8]. Metal-semiconductor core-shell nanoparticles in particular are the focus of intensive research due to their enhanced optical properties[9-17]. For instance, it is believed that if the surface plasmon resonance excitation energy of the metal nanoparticle core can be tuned to match the band gap energy of the semiconductor shell, the energy transfer between the semiconductor coating and the metal cores will be more efficient[9-11].

Typically, metal-semiconductor core-shell nanoparticles are synthesized using wet chemical methods. A common synthetic strategy involves harvesting seed crystals of the core material and treating them to induce growth of the shell material[9-13]. This conventional synthesis method has several disadvantages. It is usually carried out in toxic organic solvent at elevated temperatures. The thickness of semiconductor shell is usually predetermined by the amount of precursor added into the system, which makes it somewhat difficult to control[17,18].

3.1.2 Electrochemical Atomic layer deposition of metal-semiconductors core-shell nanoparticles

Electrochemical synthesis of metal and semiconductor nanometer-scale films is attractive for a number of reasons, including the ability to use aqueous rather than organic solvents, formation of conformal deposits, room-temperature deposition, low cost, and precise control of composition and thickness of semiconductor coating on metal nanoparticles. Electrochemical atomic layer deposition (EC-ALD) and electrochemical atomic layer epitaxy (EC-ALE) are techniques in which electrochemical surface limited reactions such as underpotential deposition (UPD) and surface redox replacement reactions are used to deposit elements from molecular precursors in solution. These techniques have been successfully used by a number of research groups to deposit binary semiconductor nanofilms[19-21], semiconductor heterojunctions[22], superlattices[20,23-26], and, more recently, metal nanofilms[27,28].

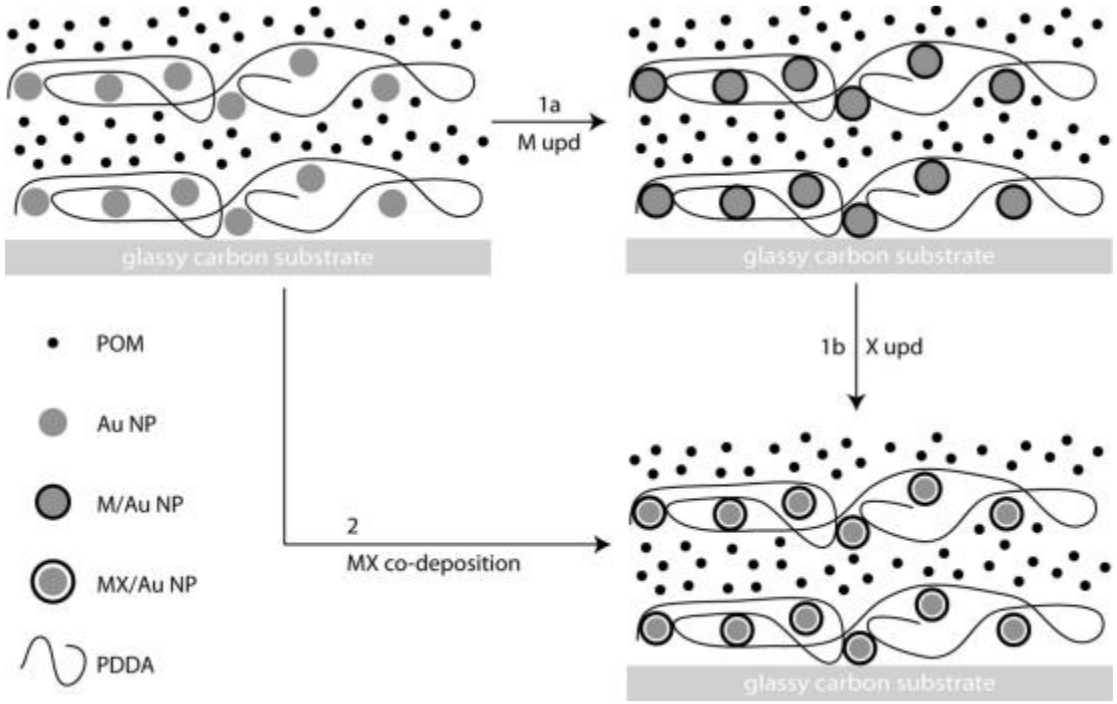

Figure 3.1 Formation of Metal-Semiconductor Core-Shell Nanoparticle Films Using Surface Limited Electrochemical Reactions. Route 1: deposition of a binary semiconductor, MX, using electrochemical atomic layer deposition (EC-ALD). Route 2: atom-by-atom co-deposition of MX. Taken from ref. 88 with permission.

To our knowledge, the use of electrochemical techniques to produce core-shell nanoparticles has not been explored to any significant extent, primarily owing to the difficulty of

preparing electrically addressable arrays of nanoparticles. Recently, we have developed a method for depositing conductive thin films composed of polyelectrolyte stabilized metal nanoparticles onto glassy carbon electrodes using layer-by-layer self-assembly methods. We have shown that the metal nanoparticles in these films can participate in electron transfer reactions, behaving as an array of nanoscopic electrodes. Herein, we discuss how EC-ALD and deposition techniques based on surface limited reactions can be used to modify the surfaces of these adsorbed nanoparticle electrodes with thin layers of semiconductors (Figure 3.1). The resulting semiconductor coated Au core-shell nanoparticle films are characterized using photoluminescence (PL) and Raman spectroscopies.

3.2 Experimental

3.2.1 Chemicals

Sodium borohydride (98+% $NaBH_4$, Acros Organics), poly-(diallyldimethylammonium chloride) (PDDA) (very low molecular weight, 35 wt % in water, Aldrich), Sodium hydroxide (98.4% NaOH, Fisher), and Chloroauric acid (30 wt% $HAuCl_4$ solution in dilute hydrochloric acid, 99.99%, Aldrich) were used as received to synthesize gold nanoparticles. $Na_2WO_4 \cdot 2H_2O$ (99.995%, Sigma–Aldrich) and Phosphoric acid (85 wt. % H_3PO_4 in H_2O, 99.99% trace metals basis, Sigma–Aldrich), $KHCO_3$ (≥99.5%, Sigma-Aldrich), KCl (≥ 99.0%, Fisher), Ethanol (99.5%, Fisher), Diethyl Ether (anhydrous, Arcos), Hydrochloric acid (Fisher) with a nominal composition of 36.5-38.0% HCl, Cobalt nitrate hexahydrate (99.999% trace metals basis, Aldrich) were used as received to synthesize α_2-$K_8CoP_2W_{17}O_{61}$. Sodium acetate (99.9% CH_3COONa, Fisher) and glacial acetic acid (100.0% CH_3COOH, Fisher) were used to prepare the acetate

buffer described below. Sulfuric acid (Fisher) with a nominal composition of 95-98% H_2SO_4, Copper Sulfate Pentahydrate (99.4% $CuSO_4 \cdot 5H_2O$, Fisher), Potassium Iodide (100.4% KI, Fisher), Cadmium Sulfate (99% $CdSO_4$, Sigma-Aldrich), Sodium Sulfide (98+% Na_2S, Sigma-Aldrich), and ethylenediaminetetraacetic acid disodium salt (EDTA) (99+% $Na_2C_{10}H_{14}N_2O_8 \cdot 2H_2O$, Sigma), Tellurium dioxide (≥99% TeO_2, Sigma-Aldrich) was used as received for semiconductor depositions. Tetraethylammonium perchlorate (≥ 99.0% $(C_2H_5)_4N \cdot ClO_4$, electrochemical grade, Fluka) and Acetonitrile (99.8% CH_3CN, Sigma-Aldrich) are used to prepare supporting electrolyte in Electrochemical Impedance Spectroscopy (EIS). Millipore-Q purified deionized (DI) water (18.2 MΩ/cm^3) was used to make up all solutions and to rinse electrodes.

3.2.2 Synthesis of α_2-$K_8CoP_2W_{17}O_{61}$

α_2-$K_8P_2CoW_{18}O_{61} \cdot 15H_2O$ was synthesized according to the procedure described by Finke[29]. The precursor α-$K_6P_2W_{18}O_{62} \cdot 15H_2O$ was synthesized by dissolving of 100 g $Na_2WO_4 \cdot 2H_2O$ (0.303 mol) in 350 mL of refluxing H_2O in a 1000-mL Erlenmeyer flask. Phosphoric acid (150 mL, 0.772 mol) was added dropwisely over 30 min, and the resulting light green solution was refluxed for 8 h. The crude product was precipitated by the addition of 100 g (1.34 mol) of solid KCl and recrystallized by dissolving the precipitate in about 500 mL of boiling H_2O and cooling to 5°C overnight. The product was collected on a medium frit and washed with 150 mL (3 X 50 mL) of H_2O, 150 mL (3 X 50 mL) of 95% ethanol, and 150mL (3 X 50 mL) of anhydrous diethyl ether. The solid was dried under vacuum at room temperature for

8 hours. The final product was a mixture of α- and β-isomers of $K_6P_2W_{18}O_{62}\cdot 10H_2O$, which requires further purification.

Further purification can be achieved by dissolving α/β- $K_6P_2W_{18}O_{62}\cdot 10H_2O$ (70 g, 0.015 mol) into a 250 mL of 80 °C water in a 1500-mL flask, with magnetic stirring. $KHCO_3$ (400 mL of a 1 M solution, 0.4 mol) was added over 5 min, causing a white precipitate of $P_2W_{17}O_{61}^{10-}$ (This precipitate continues to evolve over about 30 min.) HCI (150 mL of a 6 M solution, 0.9 mol) was then added over about 10 min, regenerating a clear yellow solution of α-$P_2W_{18}O_{62}^{6-}$. Solid KCl (100 g, 1.34 mol) was then added to the solution, and it was cooled to 5 °C overnight. The compound was then recrystallized from a minimum of boiling H_2O (about 150 mL) and again cooled to 5 °C overnight, result in a pure form of α-$K_6P_2W_{18}O_{62}\cdot 14H_2O$.

To get the desired α_2-$K_8P_2CoW_{18}O_{62}\cdot 15H_2O$, in a 1000-mL Erlenmeyer flask, 135 g (0.0293 mmol) of α-$K_6P_2W_{18}O_{62}\cdot 14H_2O$ was dissolved in 300 mL of 40 °C H_2O. $KHCO_3$ (500 mL of a 1 M solution, 0.5 mol) is added with vigorous stirring. A white precipitate begins to form after about 50 mL of the base has been added. After the base addition was complete, the mixture was stirred for an additional 30 min. The white precipitate is collected on a coarse glass frit. The crude white solid was recrystallized by dissolving it in 200 mL of boiling H_2O and cooling to 5 °C overnight. The resulting white crystals were collected on a medium glass frit and washed with 150 mL (3 X 50 mL) of H_2O, 150 mL (3 X 50 mL) of 95% ethanol, and 150 mL (3 X 50 mL) of anhydrous diethyl ether. The solid is dried under vacuum at room temperature for 8 h. The crystals collected are the lacunary precursor α_2-$K_6P_2W_{17}O_{61}\cdot 15H_2O$. In a 500-mL flask, the lacunary precursor α_2-$K_6P_2W_{17}O_{61}\cdot 15H_2O$ (51.0 g, 10.6 mmol) was dissolved in 200 mL of 90 °C H_2O. A solution of 3.36 g (1.15 mmol) of $Co(NO_3)_2\cdot 6H_2O$ in 40 mL of H_2O was added with vigorous stirring, giving a dark red solution. After 15 min, solid KCl (30 g, 0.40 mmol) was

added, and the solution was cooled to room temperature. The resulting light red crystals were collected on a medium glass frit and recrystallized twice from a minimum amount (about 50mL) of boiling H_2O. The product was collected on a medium glass frit, washed with 50 mL of H_2O, and dried under vacuum at room temperature for 6 hours. The collected crystals were light red color, which is the desired compound α_2-$K_8P_2CoW_{18}O_{61}\cdot 15H_2O$.

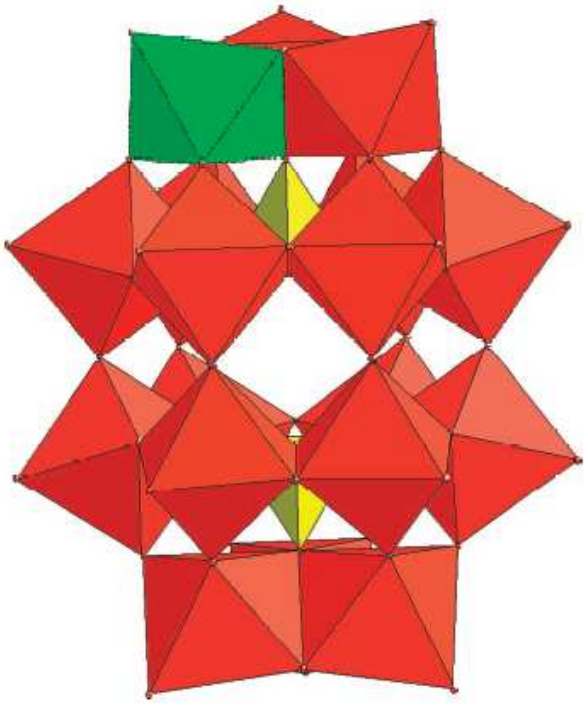

Figure 3.2 structure of α_2-$P_2CoW_{18}O_{61}^{8-}$

The structure of α_2-$K_8P_2CoW_{18}O_{61}\cdot 15H_2O$, as shown in Figure 3.2, is confirmed by Infrared, Raman, UV-vis spectroscopy, and powder X-ray diffraction by comparing to published papers[29].

3.2.3 Fabrication of Gold nanoparticles Multilayer Films.

NaOH was added dropwisely into a 5 mL solution containing 0.004 mM $HAuCl_4$ and 1.75 wt % poly-(diallyldimethylammonium chloride) (PDDA) until the yellow precipitate disappear. Then a 0.1 mL of 0.5 M $NaBH_4$ was immediately added into the solution under vigorous stirring. The resulting Au nanoparticles have an average size of $\sim 10 \pm 3$ nm, as determined by transmission electron microscopy (TEM). PDDA, with its structure shown in Figure 3.3, is a positively charged chain polyelectrolyte that is playing a role as a stabilizer for the Au nanoparticles. Thus the Au nanoparticles are positively charged.

The glassy carbon substrate was carefully polished before use and then pretreated in 1 M NaOH solution by applying a potential of +1300 mV for 10 min to render it negatively charged. The pretreated glassy carbon electrode was then immersed into the Au nanoparticle containing solution to allow the positively charged PDDA stabilized Au nanoparticles to adsorb onto the negatively charged glassy carbon surface. After 30 min, the electrode was removed, rinsed with DI water, and dried in a stream of N_2 gas. Next, the electrode was immersed in a solution containing 0.2 mM α_2-$K_8P_2CoW_{18}O_{62}$, and the negatively charged polyanions were allowed to adsorb onto the positively charged PDDA-stabilized Au nanoparticle film for 30 min. Finally, the electrode was removed from this solution, rinsed with DI water, and dried in a stream of

flowing N_2 gas. By repeating this series of steps, we are able to produce a film of any desired thickness, as shown in Figure 3.4.

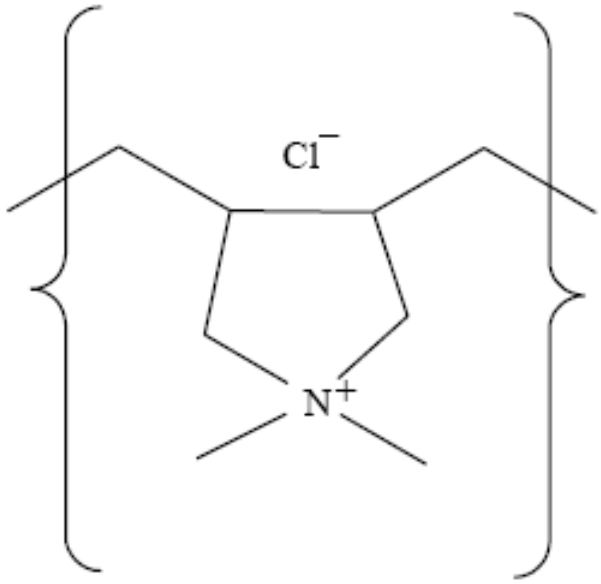

Figure 3.3 structure of poly-(diallyldimethylammonium chloride) (PDDA)

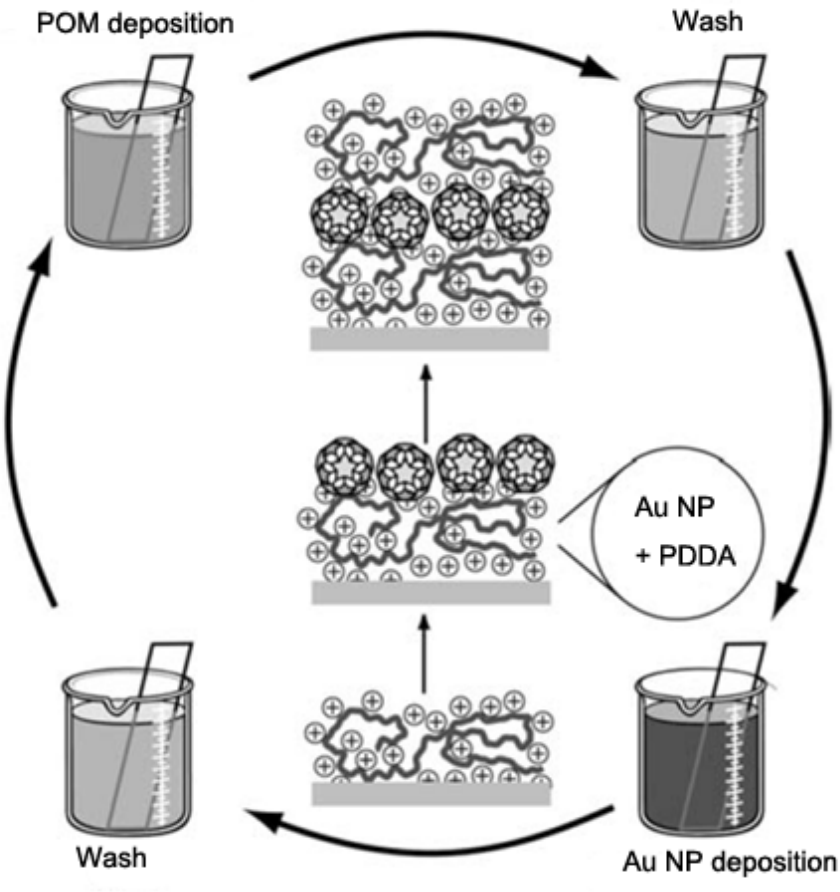

Figure 3.4 Fabrication of Gold nanoparticles Multilayer Films

For the experiments described here, 10 AuNP/polyoxometallate (POM) bilayers were deposited. The electrochemically active surface area of the films was determined by scanning from 0.20 to 1.3 V in 0.1 M $HClO_4$ and integrating the peak current associated with oxide stripping at ~800 mV, yielding a value of 0.015 cm^2.

3.2.4 Electrodeposition of Semiconductors onto Gold Nanoparticles

Cuprous Iodide (CuI) Electrodeposition

In a typical experiment, the 10 AuNP/polyoxometallate (POM) bilayers electrode ($GC/\{AuNP/POM\}_{10}$), a Ag/AgCl(sat) electrode , and a platinum gauze electrode were used as the working, reference, and counter electrodes, respectively. A Cu atomic layer was first deposited at underpotential onto the surface of the Au nanoparticles by applying a potential of +100 mV in a solution containing 10 mM $CuSO_4$ and 0.5 M H_2SO_4. The deposition time was 5 min to ensure full monolayer coverage. The electrode was then removed from the solution under potential control, rinsed with DI water, and dried with N_2 gas. An iodine atomic layer was then underpotentially deposited onto the Cu monolayer by applying a potential of +200 mV for 5 min in a solution containing 1 mM KI and 5 mM H_2SO_4.

Cadmium Sulfide (CdS) Deposition

The electrode configuration used for CdS deposition was the same as that used for CuI deposition. However, instead of using a traditional EC-ALD deposition program, we adopted the electrochemical atom-by-atom codeposition method developed by Demir and co-workers[30] so that the growth could be carried out from a single solution. The CdS deposition solution contained 0.05 M $CdSO_4$, 0.15 M EDTA, and 0.005 M Na_2S. The pH of the solution was adjusted to 5.0 using an acetate buffer. CdS was grown onto the surface of gold nanoparticles by applying a potential of -600 mV for 1.0 h.

Cadmium Telleride (CdTe) Deposition

The CdTe co-deposition was performed in a similar way to CdS co-deposition. The CdTe co-deposition solution contained 0.1 M $CdSO_4$, 0.0001 M TeO_2, and 0.1M $HClO_4$. CdTe was grown onto the surface of gold nanoparticles by applying a potential of -10 mV for 1.0 h.

3.2.5 Characterization of Semiconductor Gold Core-Shell Nanoparticle Films.

Electrochemistry

A glassy carbon electrode (3.0 mm diameter, Bioanalytical Systems, Inc.), a homemade copper electrode (1.2 mm diameter), and a gold electrode (1.6 mm diameter, Bioanalytical Systems, Inc.) were used as working electrodes. A Ag/AgCl(sat) electrode (Bioanalytical Systems, Inc.) was used as the reference electrode. A homemade platinum gauze electrode (0.77 cm^2) was used as the counter electrode. The electrochemical cell was controlled using an Epsilon electrochemistry workstation (Bioanalytical Systems, Inc.).

Photoluminescence Spectroscopy

Photoluminescence was excited using the 325 nm line (20mW)from a HeCd laser (Kimmon Electric Co., Ltd.). The photoluminescence spectra were dispersed by a Jobin-Yvon spectrometer and detected by a thermoelectrically cooled charge-coupled device (CCD) detector.

Raman Spectroscopy

Raman spectroscopy was performed using the 785 nm (300 mW) line from a wavelength-stabilized high power laser diode system (model SDL-8530, SDL Inc.) or the 514 nm line (20 mW) from an air-cooled ion laser (model 163-C42, Spectra-Physics Lasers, Inc.) as the excitation source. Raman spectra were collected and analyzed using a Renishaw inVia Raman microscope system.

Electrochemical Impedance Spectroscopy

Electrochemical Impedance Spectroscopy was performed using the BAS 100B/W Electrochemical Workstation (Bioanalytical Systems, Inc.) with the AC Impedance Module (Bioanalytical Systems, Inc.) at a fixed frequency of 1000 Hz. A glassy carbon electrode (3.0 mm diameter, Bioanalytical Systems, Inc.) was used as working electrodes. A Ag/AgCl(sat) electrode (Bioanalytical Systems, Inc.) was used as the reference electrode. A homemade platinum gauze electrode (0.77 cm^2) was used as the counter electrode. The electrochemical cell was placed in a C3 Cell Stand (Bioanalytical Systems, Inc.) to minimize electrical interference. N_2 gas was purged into the solution for 15 min before each measurement. Data was analyzed by software package 100B/W Version 2.0.

3.3 Results and Discussions

3.3.1 Au/CuI Core-Shell Nanoparticles

Cuprous Iodide (CuI) is a semiconductor with a direct band gap of about 3.1 eV. As-grown γ-CuI is generally a p-type material and consequently is of interest as a hole transport

layer in solar cells. A variety of synthetic approaches have been developed to produce CuI thin films, including several electrochemical routes. For example, Penner and co-workers showed that β-CuI nanoparticles can be grown on glassy carbon (GC) surfaces using a hybrid electrochemical/chemical method in which electrodeposited Cu nanocrystals are chemically converted to CuI via a surface metathesis reaction[31]. Several groups have reported on the interaction of I^- with single crystal Cu electrode surfaces. In an early combined electrochemistry/ultrahigh vacuum study, Itaya et al. discovered the existence of ordered monolayers of iodide on Cu(111) electrode surfaces[32]. The $(\sqrt{3} \times \sqrt{3})R30°$ structures were found to be stable as a function of electrode potential. More recently, Broekmann and co-workers reported on the formation of stable 2D CuI phases on Cu(100) surfaces during the initial phase of the anodic dissolution of Cu in iodide-containing electrolytes. Interestingly, the presence of CuI did not appear to inhibit Cu dissolution; indeed, at higher dissolution rates, 3D CuI phases were observed to form on the surface.[33,34]

In this study, we adapted the approach pioneered by the Stickney group[35] to develop a straightforward two-step EC-ALD cycle for CuI deposition. First, an atomic layer ofCuwas deposited at underpotential onto Au. The Cu-modified Au substrate was then transferred to an iodide-containing electrolyte where the UPD layer was converted to CuI at a constant applied potential of 0.20 V. It should be noted that this potential is cathodic of the Cu stripping potential, ensuring that the Cu UPD layer and resulting CuI film remains adsorbed on the Au substrate.

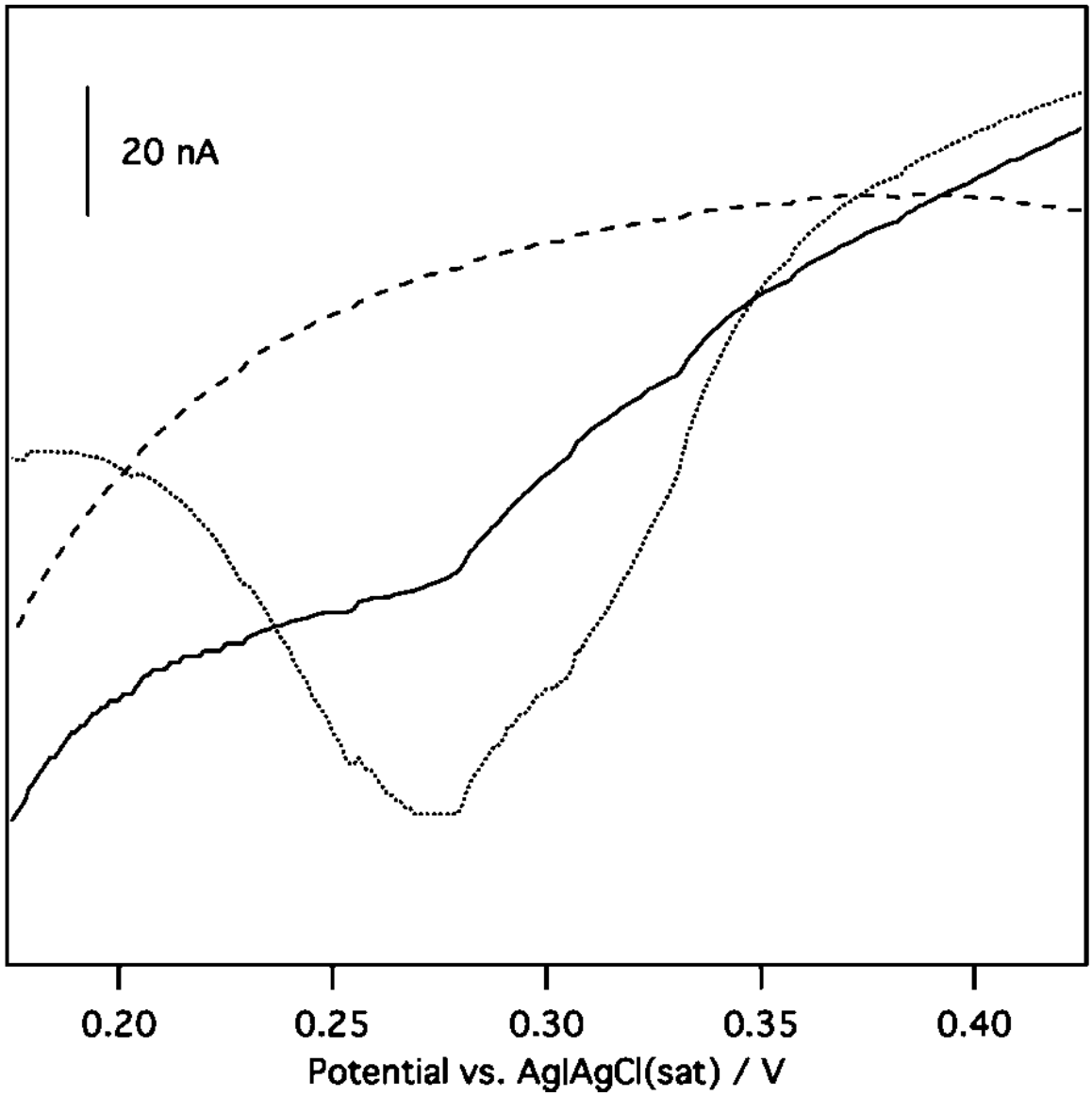

Figure 3.5 Underpotential deposition of Cu at polycrystalline Au (dotted line), GC/(AuNP/POM)$_{10}$ (solid line), and glassy carbon (dashed line). Scan rate: 1 mV/sec. Taken from ref. 88 with permission.

Cyclic voltammetric curves obtained using glassy carbon, polycrystalline Au, and GC/(AuNP/POM)$_{10}$ working electrodes immersed in a solution containing 10 mM $CuSO_4$ and 0.5 M H_2SO_4 are shown in Figure 3.5. As the potential of a polycrystalline Au electrode is scanned cathodically from an initial value of +0.40 V, a broad, well-defined UPD peak is observed at ~0.27 V (dotted line). The integrated charge density of the Cu UPD peak is ~260 μC/cm^2. These results are in excellent agreement with previous measurements of Cu UPD on polycrystalline Au electrodes[36].

It should be noted that the polyoxometallates used in these films are electrochemically silent in this potential window and have no apparent effect on the Cu UPD voltammetry. A relatively small UPD peak is seen at the same position for the GC/(AuNP/POM)$_{10}$ electrode (solid line), corresponding to a total charge density of ~75 μC/cm^2. This result is consistent with previous reports of Copper UPD on Au nanoparticles[37]. And as expected, no peaks are observed in the Cu UPD region on a bare glassy carbon electrode (dashed line) under these experimental conditions, indicating no Cu was deposited onto bare glassy carbon.

Following conversion of the Cu UPD layer to CuI as described above, PL spectroscopy was employed to determine the existence and phase of the as-deposited CuI thin films, as shown in Figure 3.6.

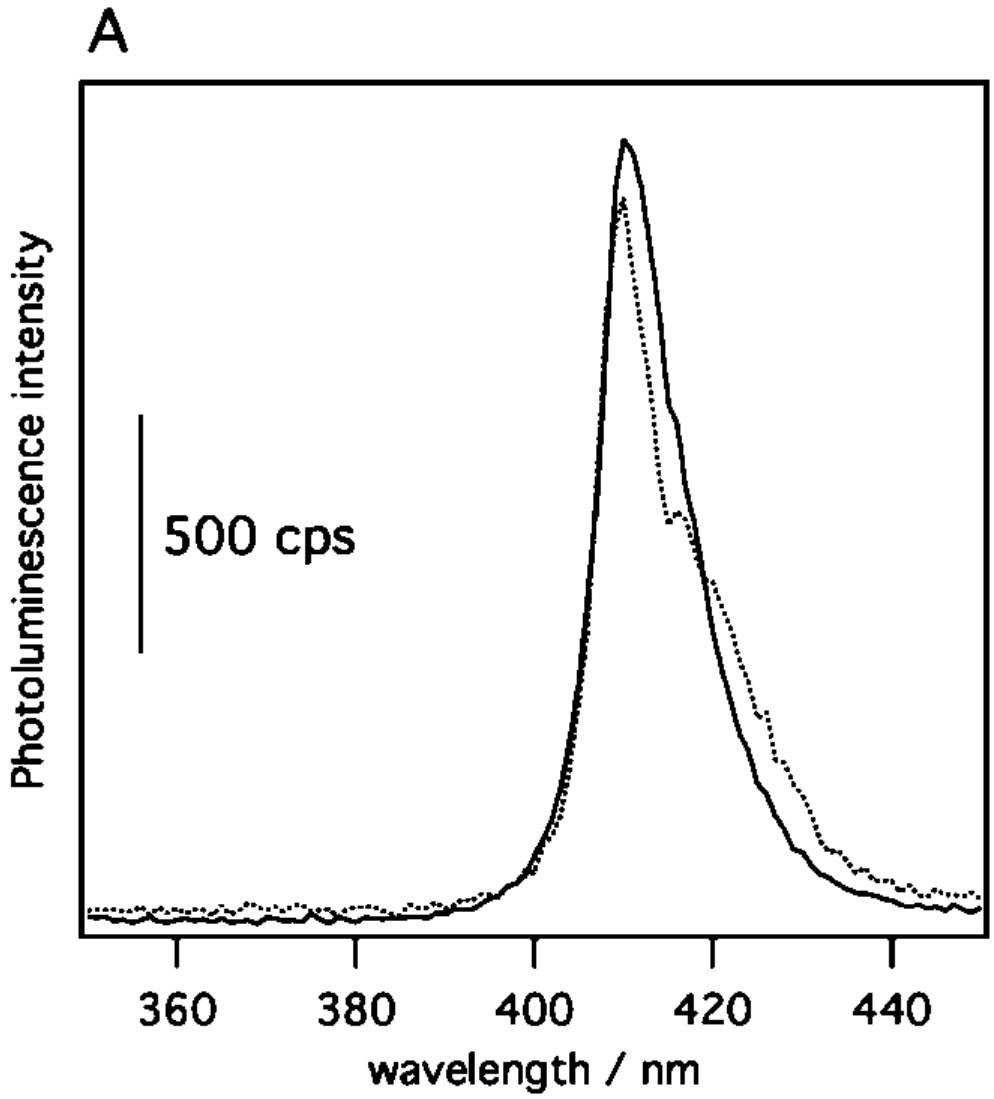

Figure 3.6a Photoluminescence spectra of electrodeposited CuI films: Bulk CuI film formed on polycrystalline Cu (solid line); CuI thin film deposited on a polycrystalline Au foil using EC-ALD (dotted line). Taken from ref. 88 with permission.

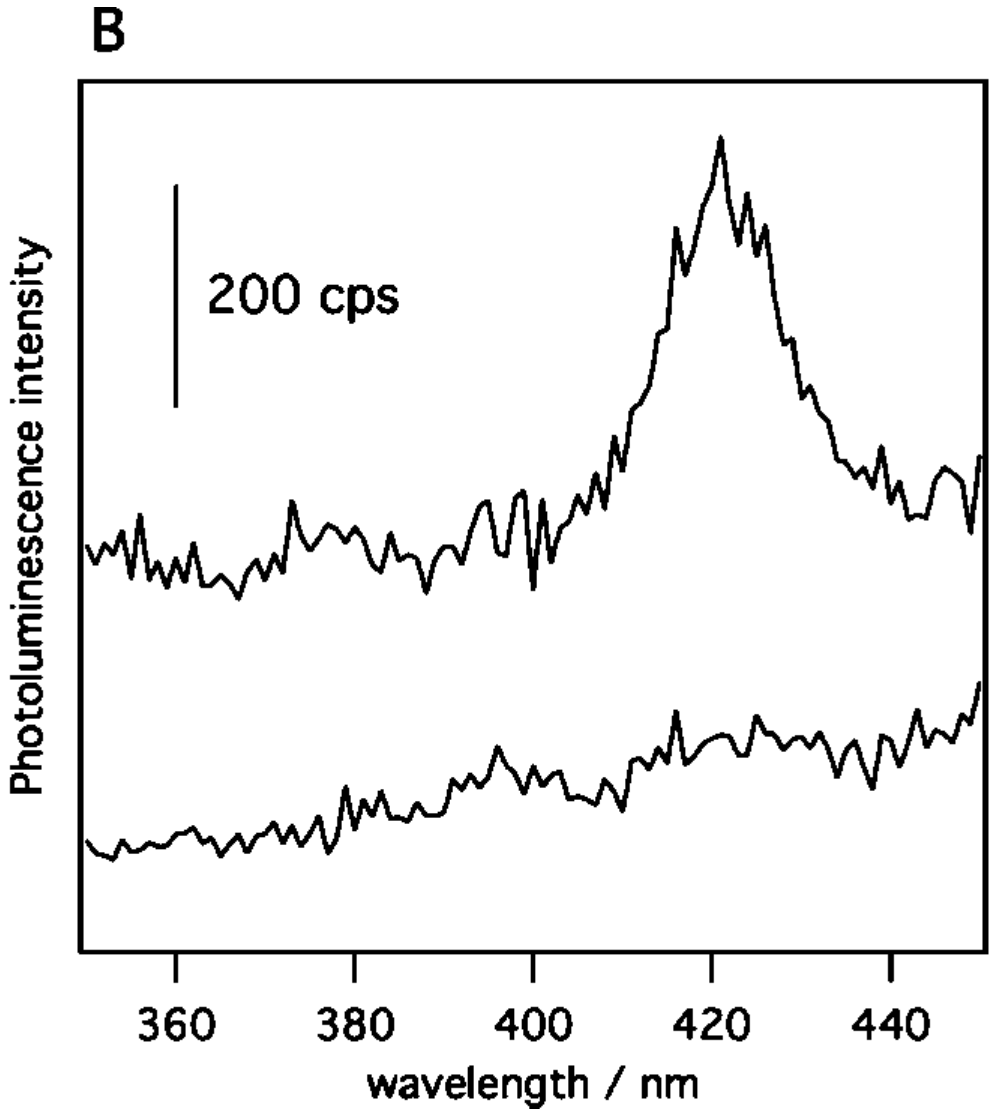

Figure 3.6b Photoluminescence spectra of electrodeposited CuI films: CuI deposited on a GC/$(AuNP/POM)_{10}$ electrode using EC-ALD; glassy carbon subjected to an EC-ALD cycle. Taken from ref. 88 with permission.

For comparison, a thick CuI film was grown onto polycrystalline Cu. As shown in Figure 3.6A (solid line), the thick CuI layer grown on a polycrystalline Cu electrode is characterized by

a strong band edge PL feature centered at ~410 nm, consistent with published literature. Next, we deposited a CuI monolayer film onto the surface of a polycrystalline Au electrode using EC-ALD. The photophysical properties of this specimen are quite similar to what we observed for the CuI(bulk)/Cu sample; in particular, the main band edge PL peak appears at the same wavelength, as shown in Figure 3.6A (dotted line). In addition, there is a distinct shoulder peak centered at ~420 nm. Zheng and co-workers attribute these two distinct PL peaks to different CuI orientations[38]. Specifically, the PL peak at 410 nm is believed to originate from CuI(110) crystallites, while the broad band at 420 nm is due to films composed primarily of CuI(111) grains. The PL spectrum obtained from a CuI film deposited on a GC/$(AuNP/POM)_{10}$ electrode is shown in Figure 3.6B (upper trace). The overall luminescence intensity is greatly diminished and consists of a single broad peak positioned at ~420 nm, consistent with the formation of a deposit comprised of predominantly CuI(111) grains. It is often possible to identify pseudomorphic heteroepitaxial conditions for growth on atomically flat single crystal substrates (for example, in the case of CuI/Cu(111), 3aCuI~5aCu). On the other hand, it is harder to rationalize heteroepitaxial deposition onto the more disordered, curved surface of AuNPs. In this case, formation of the thermodynamic product is the most likely outcome. Since such core-shell structures grow epitaxially and the shell can be considered as an extension of core structure with different chemical compositions. In addition, the growth of core and shell in these systems are very closely related[39].

Interestingly, we do not observe strong confinement shifts in the CuI PL data. In contrast, Penner et al.[31] observed confinement shifts in the PL of CuI quantum dots deposited onto graphite electrodes. Two factors account for the different behavior. First, in our system, the nanoparticle PL spectra are red shifted with respect to the bulk data due to the preferred

crystallite orientation. Since the maximum possible red shift is not known, our observation does not rule out the existence of small confinement effects in these systems.

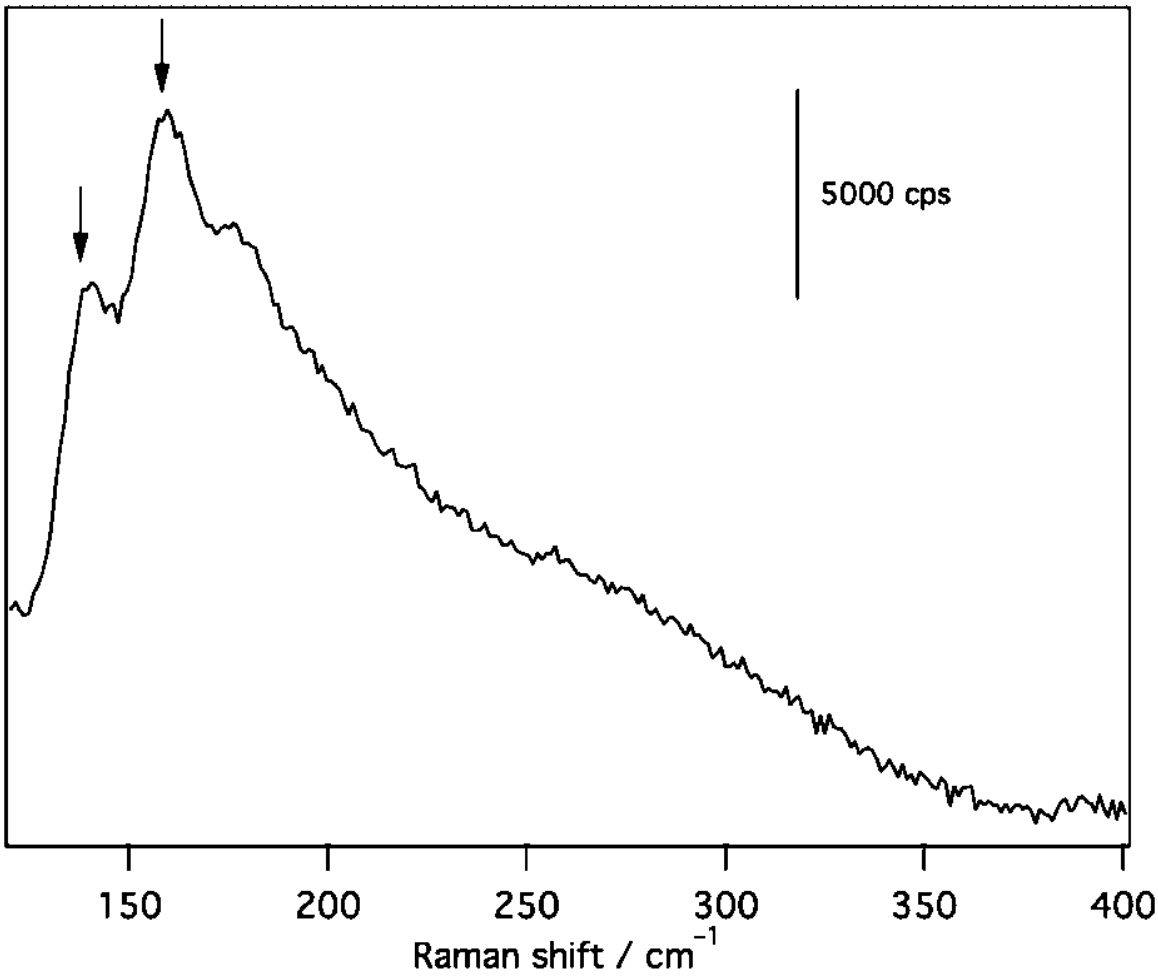

Figure 3.7 Raman spectrum of CuI deposited on a GC/(AuNP/POM)$_{10}$ electrode. Excitation wavelength: 514 nm. Taken from ref. 88 with permission.

Second, we have previously shown that electronic coupling between CdS and Au reduces the magnitude of quantum confinement effects compared to isolated CdS nanocrystals[40]. On the

other hand, substrate-nanoparticle electronic coupling is expected to be much weaker for quantum dots adsorbed on graphite, as in the case of the Penner study. Finally, we subjected a naked GC electrode to the same EC-ALD cycle we used for the Cu monolayer on Au and for the GC/(AuNP/POM)$_{10}$ electrode. The PL spectrum shown in Figure 3.6B (lower trace) displays no obvious PL peak because Cu UPD does not occur on GC under these conditions, and hence, no CuI can form. This result also indicates that no significant amounts of CuI precipitate under the experimental conditions employed for EC-ALD.

Additional evidence for CuI formation comes from Raman spectroscopy. A representative Raman spectrum (514 nm excitation wavelength) of the CuI layer deposited on the GC/(AuNP/POM)$_{10}$ electrode is shown in Figure 3.7 and consists of two strong Raman bands centered at ~141 cm^{-1} and ~158 cm^{-1} superimposed on a broad, intense luminescent background. These bands are assigned as the transverse optical (TO) and longitudinal optical (LO) phonon modes of CuI, respectively[41]. Similar spectra (data not shown) were obtained for bulk CuI films.

Taken together, our voltammetric and spectroscopic data indicate the formation of a CuI layer on the surface of Au nanoparticles embedded in the polyelectrolyte layers. Next, we wished to investigate whether another class of surface limited reaction could be used to modify the surface of the embedded Au nanoparticles. CdS is an ideal candidate for this investigation because it can be deposited electrochemically and its surface spectroscopy is well explored.

3.3.2 Au/CdS Core-Shell Nanoparticle Thin Films.

Cadmium sulfide (CdS) is a direct band gap semiconductor with 2.42 eV band gap energy and has many applications for example in light detectors. CdS was deposited onto AuNP

surfaces from a solution containing 0.05 M $CdSO_4$, 0.15 M EDTA, and 0.005 M Na_2S buffered to pH 5.0 using an acetate buffer. To determine the appropriate applied potential for the codeposition of CdS, we first studied the voltammetric response of a GC/$(AuNP/POM)_{10}$ electrode in separate solutions containing the Cd and S precursors, as shown in Figure 3.8.

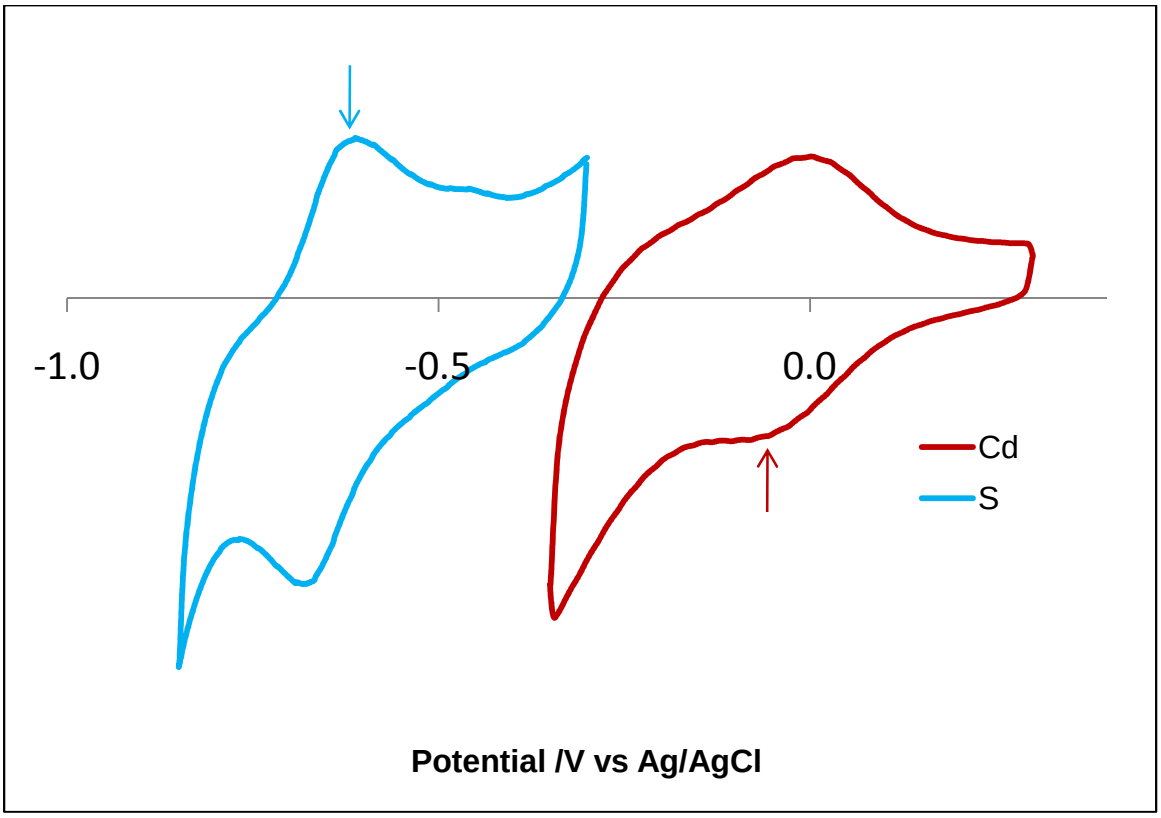

Figure 3.8 Cyclic voltammetry of Cd and S electrodepositionin separate solutions. The arrows denote for UPD peaks.can rate: 100 mV/sec.

Both cyclic voltammetric behavior of Cd and S agree well to that observed in previous electrochemical studies of this system. The UPD peaks of Cd and S are around -0.05 and -0.61 V, respectively. Obviously, the UPD peak position of sulfur is more negative than the bulk deposition peak of Cadmium, and the underpotential deposition peak of Cd is more positive than the bulk deposition position of S. Thus, in the S UPD region, Cd bulk deposition will occur and in the Cd UPD region, S bulk deposition will occur. We can conclude that, under the EDTA-free environment, the desired co-UPD of Cd and S is not likely to happen.

A representative CV obtained in a 0.005 M Na_2S and 0.15 M EDTA solution at pH 5 is shown in Figure 3.9. Both S and Cd UPD peak shift negatively in the presence of EDTA, which was also reported by Demir and co-workers[30]. The S UPD peak is centered at approximately -0.62 V on the anodic scan (dashed vertical line), and the S monolayer stripping peak is centered at approximately -0.65 V on the cathodic scan, consistent with previous research. Figure 3.9 also shows the cyclic voltammetric response of a GC/$(AuNP/POM)_{10}$ electrode immersed in a 0.05 M $CdSO_4$ and 0.15 M EDTA solution at pH 5. EDTA is used to chelate Cd^{2+} and thus prevent precipitation of CdS in the codeposition solution; as a consequence, the Cd UPD peak is shifted negative to a potential of approximately-0.58V (dashed vertical line). Actually both S and Cd UPD peak shift negatively in the presence of EDTA, though the shift of S UPD is very small, which was also reported by Demir and co-workers[30].

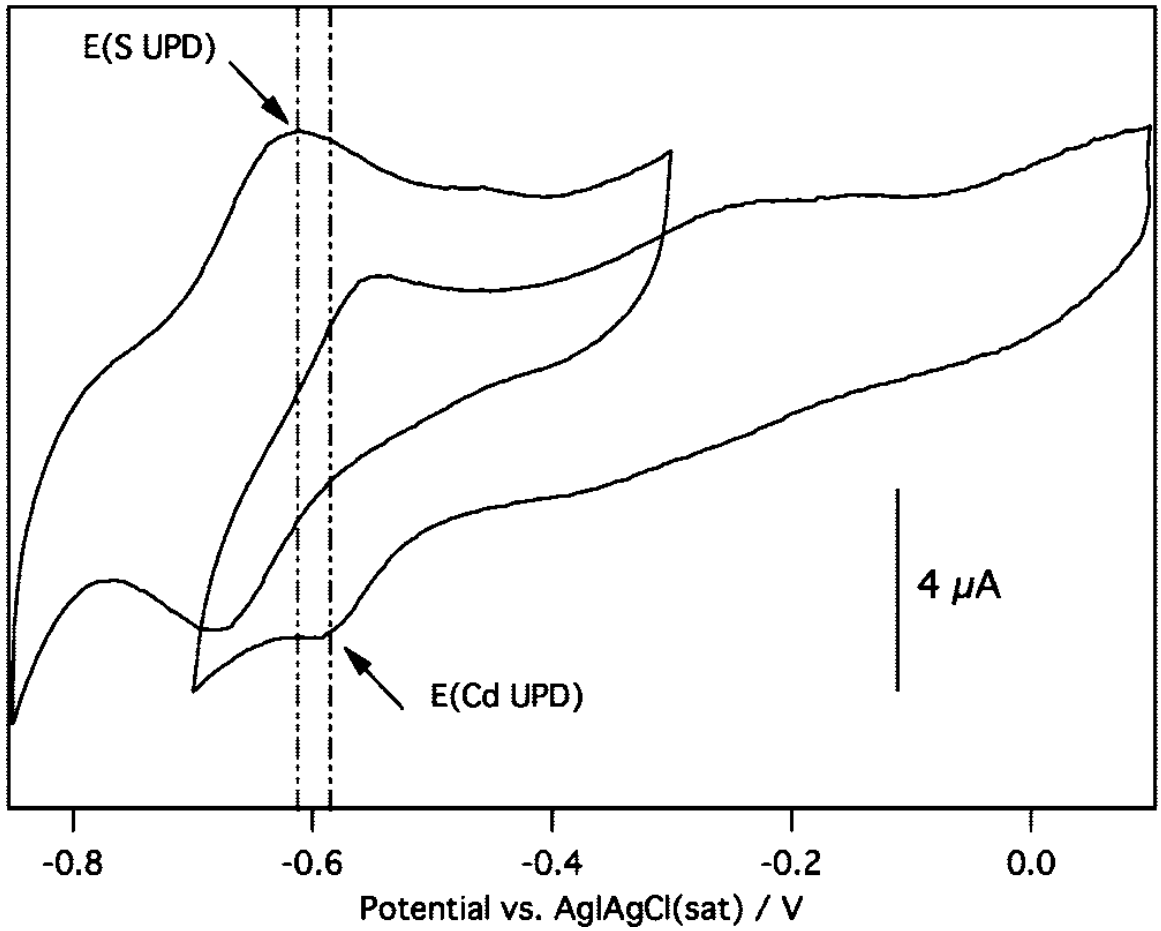

Figure 3.9 Cyclic voltammetry of Cd and S electrodeposition, showing the potential window for CdS codeposition. Scan rate: 100 mV/sec. Taken from ref. 88 with permission.

Under these experimental conditions, a narrow range of potentials exists where Cd and S can simultaneously be deposited at underpotential onto Au. The codeposition window lies between the two vertical dashed lines in Figure 3.9 (between -0.58 and -0.62 V).

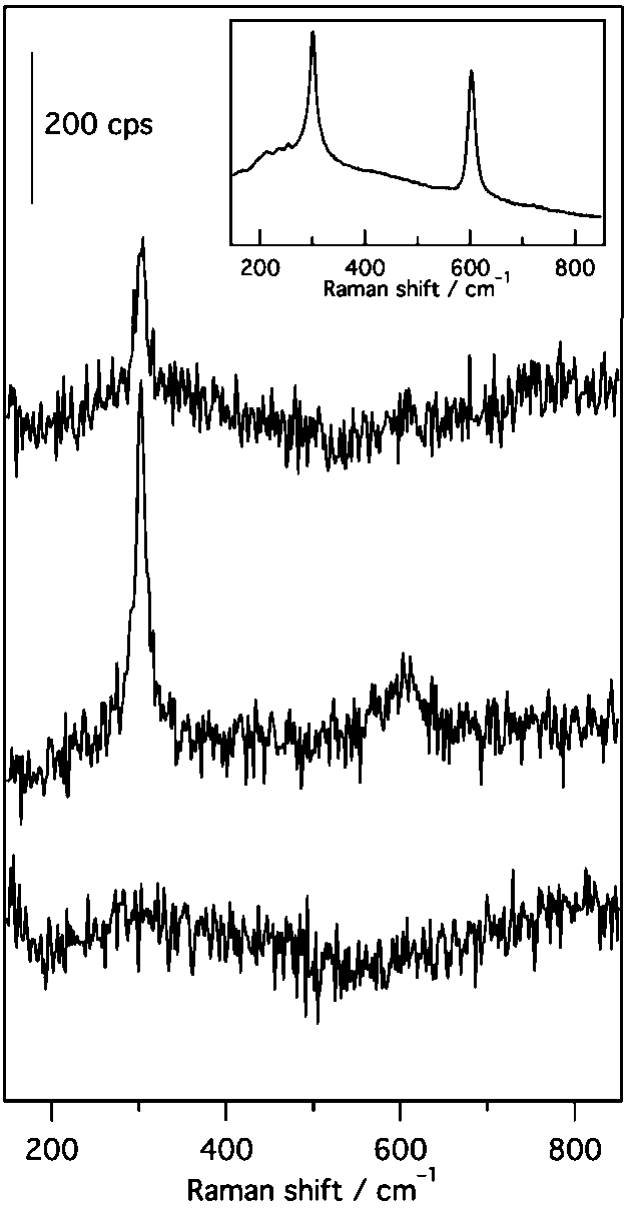

Figure 3.10 Raman spectroscopy of CdS nanofilms. Lower trace, glassy carbon; middle trace, polycrystalline Au; upper trace, GC/(AuNP/POM)$_{10}$ electrode. The inset shows the Raman spectrum of a CdS single crystal. The excitation wavelength was 514 nm. Taken from ref. 88 with permission.

It should be pointed out that deposition of Cd^{2+} onto UPD Cd or HS^- onto UPD S will not take place in the codeposition window, since the bulk deposition potentials are never reached. In our experiments, we applied a -0.60 V potential to the working electrode. Although polyoxometalates such as the Wells-Dawson anions used here can be reduced at negative potentials, the cyclic voltammetric behavior illustrated in Figure 3.9 is virtually identical to what has been previously reported for Cd and S upd on Au electrodes in electrolytes that do not contain POMs. Thus, while the POMs may act as a sink for electrons, they do not appear to significantly alter the UPD of Cd or S on Au nanoparticle surfaces.

3.3.3 Au/CdTe Core-Shell Nanoparticle Thin Films.

Cadmium telluride (CdTe) is a crystalline compound formed from cadmium and tellurium. It is a direct band gap semiconductor with a 2.42 eV band gap energy and has many applications for example in light detectors. Because both Cd and Te deposition are reductive deposition, the co-deposition of CdTe is different from that of CdS.

To determine the appropriate applied potential for the codeposition of CdTe, we first studied the voltammetric response of a GC/$(AuNP/POM)_{10}$ electrode in separate solutions containing the Cd and Te precursors at various concentrations, to find a good concentration pair that Cd and Te UPD peaks aligned. A cyclic voltammetric result of a solution containing 0.1 M $CdSO_4$, and 0.1M $HClO_4$ is shown as red curve in Figure 3.11.

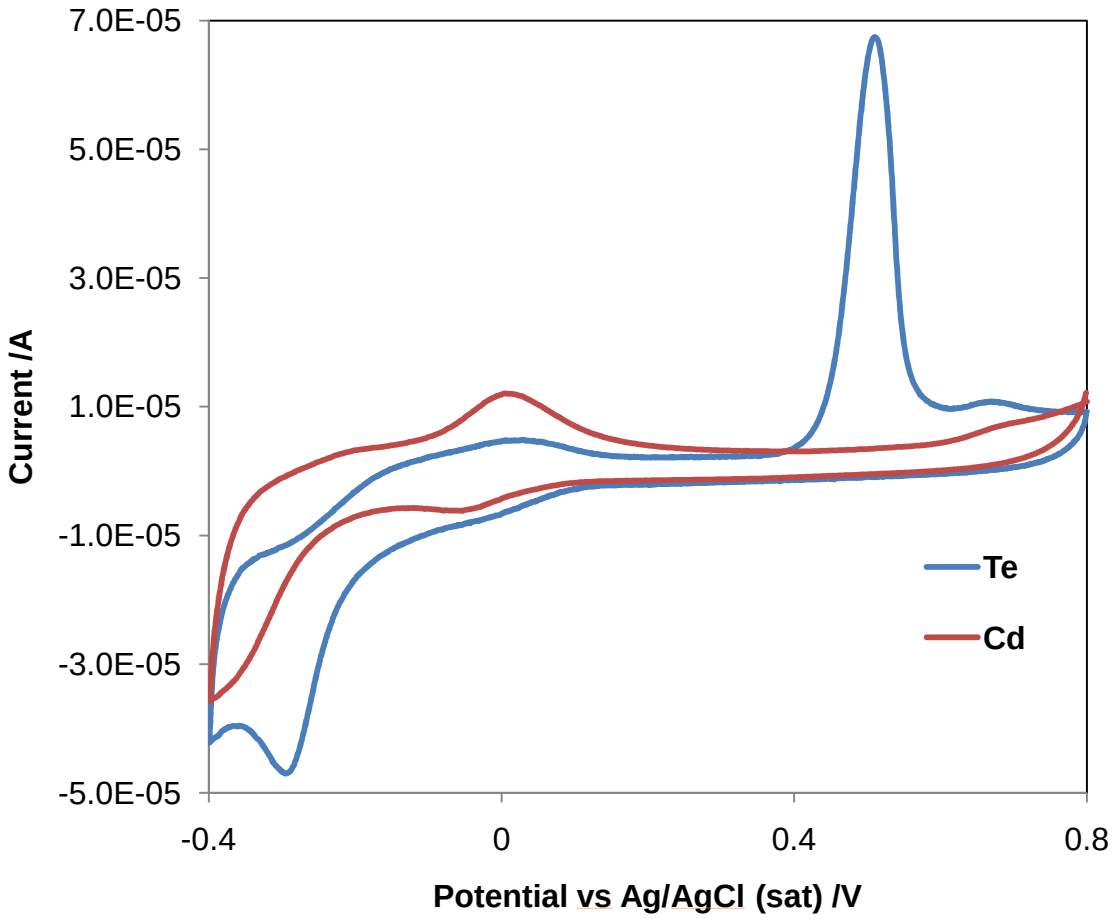

Figure 3.11 Cyclic voltammetry of Cd and Te electrodepositionin separate solutions.

Scan rate: 100 mV/sec.

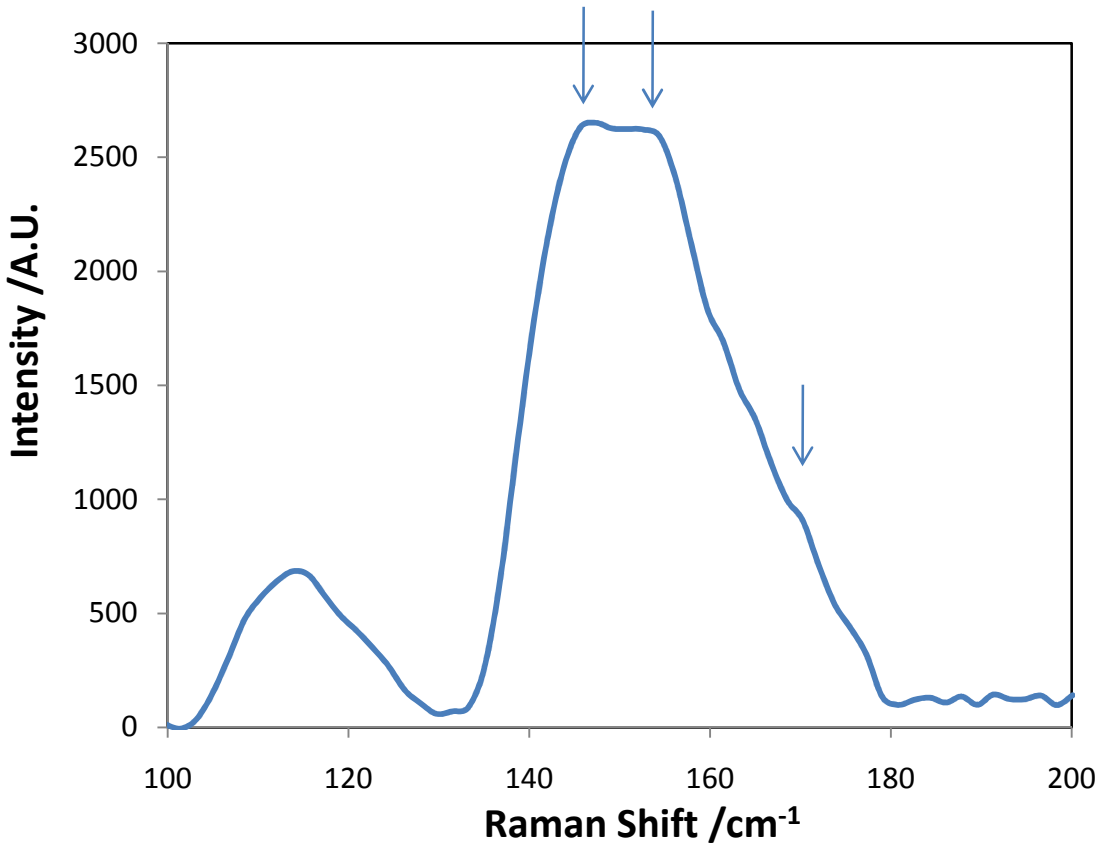

Figure 3.12 Raman spectroscopy of CdTe nanofilms on GC/$(AuNP/POM)_{10}$ electrode. The excitation wavelength was 514 nm.

The Cd UPD peak is about -50 mV versus Ag/AgCl, and the Cd bulk deposition is about -300 mV versus Ag/AgCl. A cyclic voltammetric result of a solution containing 0.0001 M TeO_2, and 0.1M $HClO_4$ is shown as blue curve in Figure 3.11. The Te UPD peak is about -20 mV versus Ag/AgCl, and the Cd bulk deposition is about -200 mV versus Ag/AgCl.Thus, for this concentration pair of Cd^{2+} and $HTeO_2^+$, a co-UPD region can be found between 0 and -100 mV

versus Ag/AgCl. We should note that the UPD current for Te is slightly higher than that for Cd at this concentration pair. Overdeposition of Te can be foreseen.

Raman spectroscopy result of CdTe nanofilms on GC/$(AuNP/POM)_{10}$ electrode is shown in Figure 3.12. Two strong Raman bands centered at ~146 cm^{-1} and ~154 cm^{-1} can be assigned as the transverse optical (TO) and surface optical (SO) phonon modes of CdTe, respectively[43], and a shoulder peak centered around 170 cm^{-1} can be assigned as longitudinal optical (LO) phonon of CdTe. All three bands confirm the existence of CdTe. However, in the case of CdTe nanoparticles[43], the intensities of three different phonon modes are in the following order: $I_{LO}>I_{SO}\approx I_{TO}$. However, in our result, the intensities of phonon modes are: $I_{SO}\approx I_{TO}>I_{LO}$. This inverse intensity order can be attributed to the doping effect of the gold core. Another explaination is that most semiconductor are on the surface, which shows a strong surface optical (SO) phonon modes.

Also, there is a mid-intensity band centered at 114 cm^{-1}, which can be assigned as Te A1 phonon mode, indicating there are excess Te deposited, which confirms our prediction of Te overdeposition.

3.3.4 Mott-Schottky analysis

Generally, electrochemical systems can be treated as a combination of several resistances and capacitors. Both real and imaginary component of impedance (Z) can be obtained from electrochemical impedance spectroscopy. The capacitance C can be calculated from the imaginary component of the impedance (Z") using the relationship $Z'' = 1/2\pi fC$. The model is adequate provided the frequency is high enough (on the order of kHz). The overall capacitance for electrochemical systems consists of double layer capacitance and dielectric capacitance. In metal electrodes, double layer capacitance is the major contribution of the overall capacitance. While in semiconductor or polymeric electrodes, the dielectric capacitance becomes important[44]. In the case of semiconductors, dielectric capacitance is all from the space charge region of semiconductor. Since these capacitances are in series, the total capacitance is the sum of their reciprocals. As the space charge capacitance is much smaller than double layer capacitance (2-3 orders of magnitude), the contribution of the double layer capacitance to the total capacitance is negligible. Therefore, the capacitance value calculated from this model is assumed to be the value of the space charge capacitance[45].

Mott-Schottky relationship was initially used to characterize metal-semiconductor junctions. It can be adopted into solution-semiconductor system as well[46-48]. The Mott-Schottky equation describes the relationship between inverse square of space charge layer capacitance, $\frac{1}{C_{sc}^2}$, and semiconductor electrode potential E, as shown in the following equation:

$$\frac{1}{C_{sc}^2} = \frac{2}{e\varepsilon\varepsilon_0 N}\left(E - E_{FB} - \frac{kT}{e}\right)$$

Where

C_{sc} – capacitance of the space charge region

ε = dielectric constant of the semiconductor

ε_0 – permittivity of free space

N = donor density (electron donor concentration for an *n*-type semiconductor or hole acceptor concentration for a *p*-type semiconductor)

E = applied potential

E_{fb} = flatband potential

By using the well-accepted value of parameters, such as $e = 1.602 \times 10^{-19}$ C, $\varepsilon_0 = 8.854 \times 10^{-12}$ F·m^{-1}, the slope of the Mott-Schottky plot, $\frac{2}{e\varepsilon\varepsilon_0 N}$, can be used to calculate the majority carrier concentration of the semiconductor. And the sign of the slope implies the type of semiconductors. If the slope is positive, the semiconductor is N type. And if the slope is negative, the semiconductor is P type.

The flatband potential of semiconductor can be determined by extrapolation the Mott-Schottky plot to $\frac{1}{C^2} = 0$.

To further investigate the metal-semiconductor core-shell structure by Electrochemical Surface-Limited Reactions. Mott-Schottky analysis was performed by measuring the dielectric

capacitance by electrochemical impedance spectroscopy for our three gold-semiconductors nanofilms.

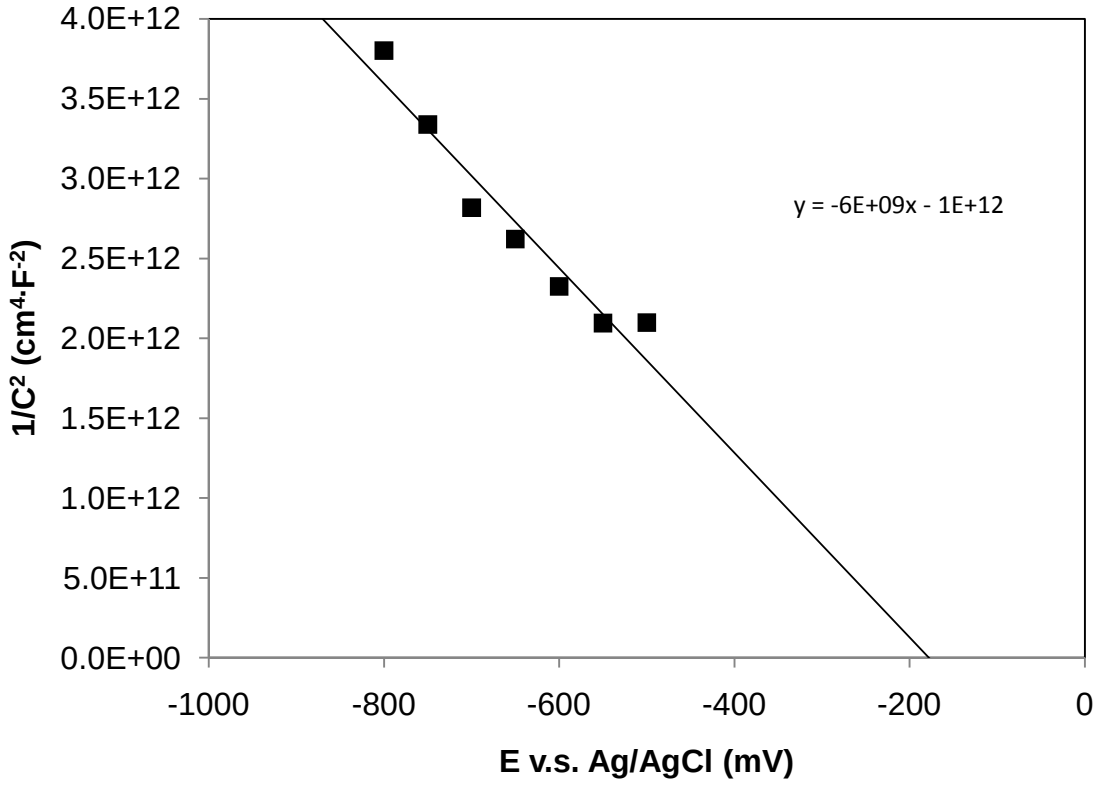

Figure 3.13 Mott-Schottky plot of Au-CuI nanofilms

In a typical experiment, the semiconductor deposited GC/(AuNP/POM)$_{10}$ electrode was used as working electrodes. A Ag/AgCl(sat) electrode was used as the reference electrode. A homemade platinum gauze electrode was used as the counter electrode. The electrochemical

inactive supporting electrolyte made of 0.1 M Tetraethylammonium perchlorate in Acetonitrile is used to preclude the contribution od faradic currents.

Typical Mott-Schottky plot of Au-CuI nanofilms is shown in Figure 3.13. It's a P type semiconductor since the slop is negative. The majority carrier (hole) concentration are calculated as $N = 4.86 \times 10^{21}$ cm^{-3} by adopting dielectric constant $\varepsilon = 4.84$ form the work of Madelung and co-workers[49]. And the flatband potential of electrochemical deposited Au-CuI nanofilms is -170 mV.

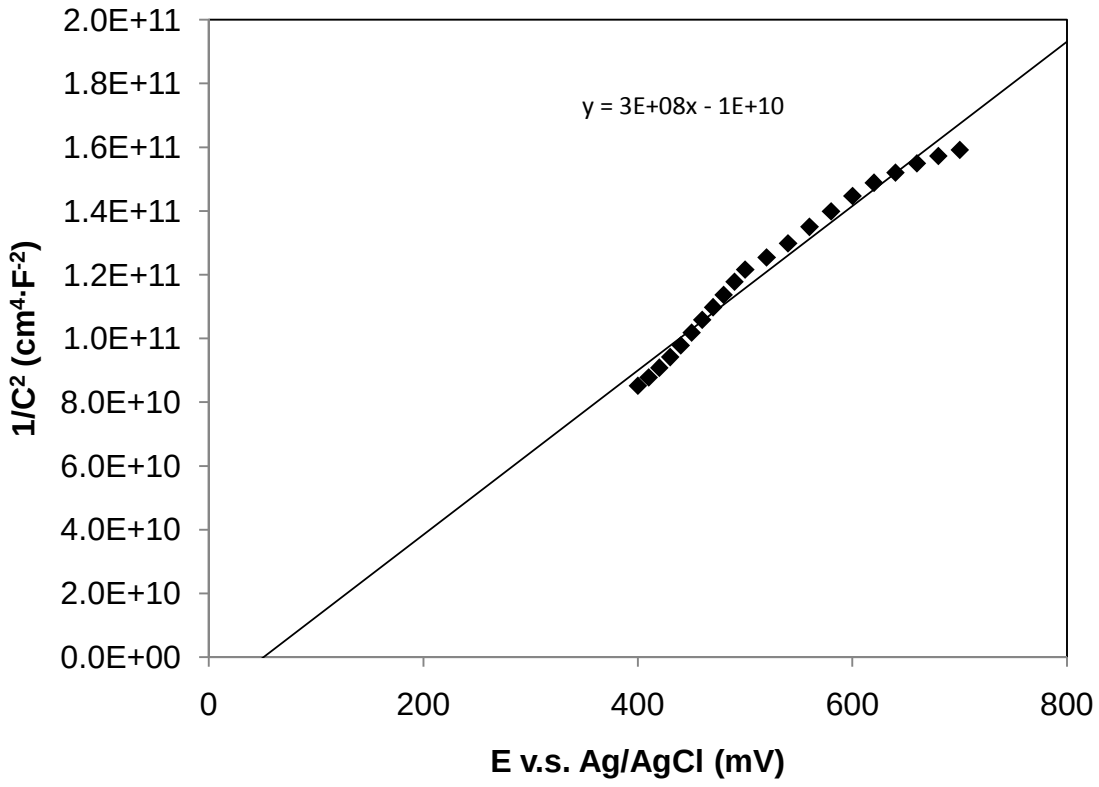

Figure 3.14 Mott-Schottky plot of Au-CdS nanofilms

Typical Mott-Schottky plot of Au-CdS nanofilms is shown in Figure 3.14. It's a N type semiconductor since the slop is positive. The majority carrier (electron) concentration are calculated as $N = 2.03 \times 10^{19}$ cm^{-3} by adopting dielectric constant $\varepsilon = 29.57$ form the work of Zhou[50] for chemically grown CdS nanoparticles. And the flatband potential of electrochemical deposited Au-CdS nanofilms is +40 mV.

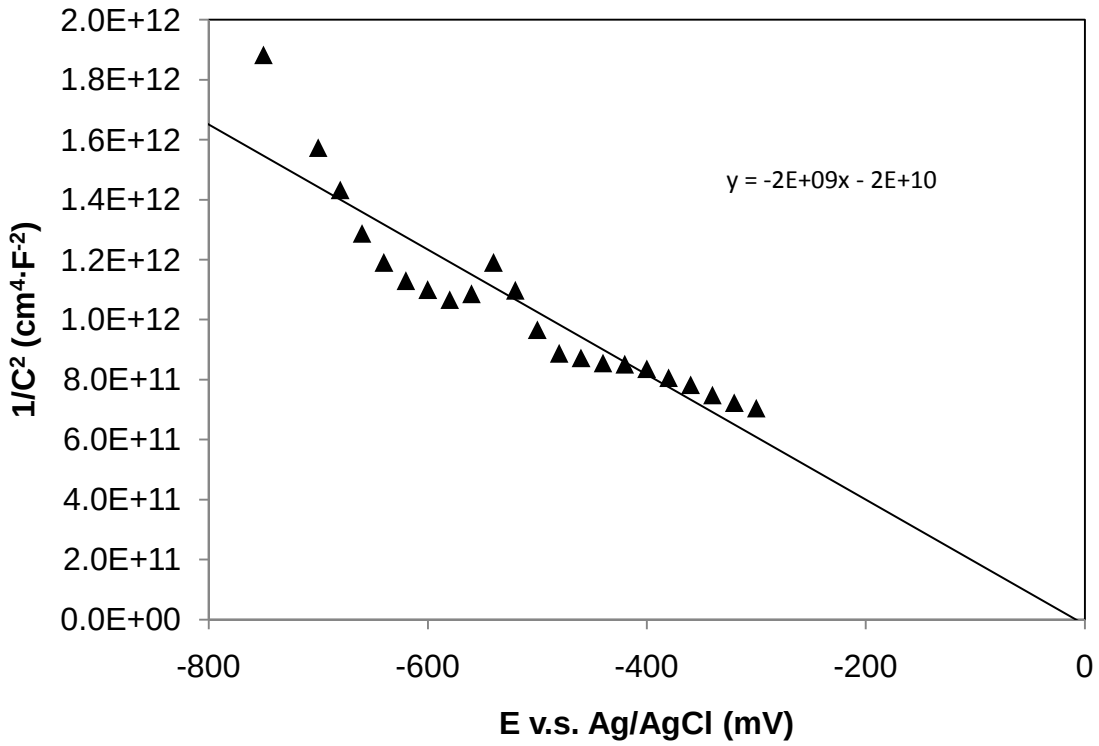

Figure 3.15 Mott-Schottky plot of Au-CdTe nanofilms

Typical Mott-Schottky plot of Au-CdTe nanofilms is shown in Figure 3.15. It's a P type semiconductor since the slop is positive. The majority carrier (hole) concentration are calculated as $N = 1.06 \times 10^{22}$ cm^{-3} by adopting dielectric constant $\varepsilon = 6.615$ form the work of Mathew and co-workers[51] for electrodeposited CdTe on stainless steel foil. And the flatband potential of electrochemical deposited Au-CdTe Core-shell nanostructure is -10 mV.

A summary of the Mott-Schottky analysis for all three semiconductors is listed in Table 3.1. For CuI and CdTe, the majority carrier concentrations greatly exceed the reported value. And for CdS, the majority carrier concentration is close to those with highest values. The high

majority carrier concentration measured by Mott-schottky can be explained by several factors. One is the low dielectric constant ε measured from the single crystal or micrometer thick thin-film semiconductors cannot represent the nanometer thick semiconductor coating on the gold nanoparticles. On one hand, the dielectric constant ε of semiconductors increase inversely with size[50], due to the high surface-volume-ratio in the nanomaterials. The interfaces with high surface-volume-ratio in the nanosized samples may contain a great deal of defects such as nanoporosities, vacancy clusters, vacancies and dangling bonds[85]. These defects can result in a change of positive and negative space-charge distributions in the nanomaterials surface when exposed to an external electric field.

Meanwhile, a great number of dipole moments are unavoidably formed after they have been trapped by defects. Consequently, space-charge polarization occurs in the interfaces of semiconductor nanoparticles, which results in the much larger dielectric constant ε for semiconductor nanoparticles. In contrast, macro-scale semiconductors mainly show their bulk properties. Thus the space charge polarization is hardly observed on them.

On the other hand, these compound semiconductors have a specific surface with a high density of disordered ions. For examples, there are many S vacancies with negative ions in the CdS nanoparticles. There are also a great number of dense Cd gaps at high bands with positive ions on the interfaces acting as shallow donors. In consequence, Cd gaps together with S vacancies lead to many dipole moments. When these dipole moments are under the influence of an external electric field many of them rotate. In this case, rotation-direction polarization happens in the interfaces of the nanoparticles.

Table 3.1 Summary of Mott-Schottky analysis for all three semiconductors

	Type	Carrier Concentration /cm^{-3}	Published values	E_{fb} /mV v.s. Ag/AgCl	Published values
CuI	P	4.86×10^{21}	9.30×10^{16} (ref 52) 4.9×10^{18} (ref 53)	-170	+ 68 (ref 54)
CdS	N	2.03×10^{19}	1.3×10^{15} (ref 55) 2×10^{17} (ref 56) 2.8×10^{19} (ref 57) 1.62×10^{14} (ref 58) 1.8×10^{17} (ref 59,60) 1.02×10^{17} (ref 61) 1.86×10^{16} (ref 62) 4.82×10^{19} (ref 63) 2.90×10^{16} (ref 64) 7.5×10^{18} (ref 65) 6.1×10^{18} (ref 66)	+ 40	-1050 (ref 56) + 400 (Ref 67) -850 (Ref 68) -1250 (Ref 69) -700 (Ref 70)
CdTe	P	1.06×10^{22}	7.6×10^{15} (ref 71) 4.0×10^{7} (ref 72) 2.4×10^{13} (ref 73) 1.0×10^{17} (ref 74,77) 1.2×10^{17} (ref 75) 1.72×10^{13} (ref 76) 2.1×10^{11} (ref 78) 1.36×10^{13} (ref 79) 2×10^{16} (ref 80) $10^{14} – 10^{15}$ (ref 81) 1.5×10^{17} (ref 82) 2.5×10^{15} (ref 83)	- 10	+640 (Ref 67) -650 (Ref 84) -350 (Ref 83)

Considering that conventional CdS single crystals that do not have such large specific surfaces and high-density gaps, the rotation-direction polarization disappears on the interfaces of conventional CdS single crystals. Since this rotation-direction polarization has an important

contribution to higher values of the dielectric constant ε, this is another reason why ε of nanosized CdS is much higher than that of macro-sized CdS. One way to eliminate the effects of space-charge polarization and rotation-direction polarization on the dielectric constant ε measurement of semiconductors nanoparticles is to increase the measurement frequency. Under the circumstance when measurement frequency is high enough, the two polarization discussed above will not exist[50], according to the theory of dielectric polarization and space-charge polarization.

Another factor can be attributed to the high majority carrier concentrations is the pinholes of the semiconductor thin film on top of the gold nanoparticles. The concept of electrochemical atomic layer deposition is based on the fact that the interaction between materials deposited and the substrate surface (M-S interaction) is stronger than the interaction between each atom of materials deposited (M-M interaction). If the substrate cannot establish such interactions, or the M-S interaction is weaker than the M-M interaction, the electrochemical atomic layer deposition will not occur at the underpotential. Thus, semiconductor cannot be deposited on the defect sites of substrate, which is gold nanoparticle in our case, leaving out uncovered gold surface and forming semiconductor pinholes. In the electrochemical impedance spectroscopy, the pinholes are filled with electrolytes and play as conducting or semiconducting if taking the small pore-size into account, pathways. Thus, the pinhole can increase the overall conductance of the semiconductors and as a result, attributed to the calculated high majority carrier concentrations.

Flatband potential, E_{fb}, refers to the potential where the potential drop associated with the space charge in the semiconductor, vanishes as the charge on the semiconductor becomes zero. At E_{fb}, the Fermi level of the semiconductor, which can be changed by the applied potential, matches the Fermi level of the electrolyte, and there is no band bending in the semiconductor.

Thus, flatband potential is solution determined. That is the reason why all the reported values of flatband potentials are scattered from each other, as well as from our results.

One of the two premises of using Mott-Schottky analysis on the semiconductor/solution interface is that the double-layer capacitance is much larger (at least 2-3 orders of magnitude) than the semiconductor space charge capacitance so the inverse square of the double-layer capacitance is much smaller than the inverse square of the space charge capacitance. Then the contribution from double-layer capacitance to the inverse square of the total capacitance is negligible. It is usually true in marco-scale system. However, the validity of this assumption in nanomaterials remains at stake. In the marco-scale systems, the double-layer capacitance can be expressed using a parallel-plate capacitor model.

$$C = \epsilon_r \epsilon_0 \frac{A}{d}$$

The parallel-plate capacitor is constructed of two parallel plates both of area A separated by a distance d. As the size decreases into nano-scale, the area A becomes very small, while the thickness of Helmholtz layer d remains unchanged. Thus the double layer capacitance C can be regarded as a linear function of area A. Using the same theory to examine the thin film semiconductor space charge capacitance, as the size decreases into nano-scale, the area A becomes very small, as well. But the thickness of space charge region d also becomes very thin, at most as thick as the semiconductor film. Thus the space cahrge capacitance C can be regarded as both a linear function of area A and an inverse linear function of depletion depth d. Thus, in a

nano-sized system, the semiconductor space charge capacitance is large, and the double-layer capacitance is no longer much larger than the semiconductor space charge capacitance.

Back in our gold-semiconductor core-shell nanoparticles, the measured high majority carrier concentrations (10^{19}-10^{22} cm^3) also backs the thin space charge region theory[86,87] up. Thus, the contribution from double-layer capacitance to the inverse square of the total capacitance may not be neglected and the expected capacity/voltage relationship for this case is[86], where C_H demotes for the double-layer capacitance (Helmholtz layer capacitance):

$$\frac{1}{C_{sc}^2} = \frac{1}{C_H^2} + \frac{2}{e\varepsilon\varepsilon_0 N}\left(E - E_{FB} - \frac{kT}{e}\right)$$

Due to the interference of double-layer capacitance, the flat band potential measured by Mott-Schottky plot is shifted. For n-type semiconductor, it shifts to negative direction, and for p-type semiconductor, it shifts to positive direction.

3.4 Conclusions

Gold nanoparticles are electroactive sites on POM/Au nanoparticle electrode layer-by-layer assemblies. POM function as electron shuttle transporting e^- between Au nanoparticles layers. EC-ALD and electrochemical atom-by-atom codeposition have been used to grow three different semiconductor nanofilms, namely CuI, CdS, and CdTe, onto the surfaces of metal nanoparticles embedded in polyelectrolyte thin films. By utilizing underpotential deposition and

atom-by-atom deposition, semiconductor growth is limited to the metal nanoparticle surface. The semiconductor nanofilms show similar spectroscopic response to those bulk materials. The slight differences of characterizations between bulk semiconductors and semiconductors on gold nanoparticles can be attributed to unique properties of metal nanoparticles surface. These core-shell nanoparticle thin films are promising candidates for a number of energy conversion and optoelectronic applications.

References

(1) Kim, D.; Miyamoto, M.; Mishima, T.; Nakayama, M., Strong enhancement of band-edge photoluminescence in CdS quantum dots prepared by a reverse-micelle method; *J. Appl. Phys.* **2005**, 98, 083514.

(2) Guo, L.; Yang, S.; Yang, C.; Yu, P.; Wang, J.; Ge, W.; Wong, G. K. L., Highly monodisperse polymer-capped ZnO nanoparticles: Preparation and optical properties; *Appl. Phys. Lett.* **2000**, 76, (20), 2901-2903.

(3) Tamborra, M.; Striccoli, M.; Comparelli, R.; Curri, M. L.; Petrella, A.; Agostiano, A., Optical properties of hybrid composites based on highly luminescent CdS nanocrystals in polymer; *Nanotechnology* **2004**, 15, S240-S244

(4) Harada, Y.; Hashimoto, S., Enhancement of band-edge photoluminescence of bulk ZnO single crystals coated with alkali halide; *Phys. Rev. B* **2003**, 68, (4), 045421.

(5) Okamoto, Y.; Ishizuka, S.; Kato, S.; Sakurai, T.; Fujiwara, N.; Kobayashi, H.; Akimoto, K., Passivation of defects in nitrogen-doped polycrystalline Cu_2O thin films by crown-ether cyanide treatment; *Appl. Phys. Lett.* **2003**, 82, (7), 1060-1062.

(6) Xu, L.; Chen, K.; El-Khair, H. M.; Li, M.; Huang, X., Enhancement of band-edge luminescence and photo-stability in colloidal CdSe quantum dots by various surface passivation technologies; *Applied Surface Science* **2001**, 172, (1-2), 84-88.

(7) Menezes, F. D. d.; A.G. Brasil, J.; Moreira, W. L.; Barbosa, L. C.; Cesar, C. L.; Ferreira, R. d. C.; Farias, P. M. A. d.; Santos, B. S., CdTe/CdS core shell quantum dots for photonic applications *Microelectronics Journal* **2005**, 36, (11), 989-991

(8) Farias, P. M. A. d.; Santos, B. S.; Menezes, F. D.; Jr., A. G. B.; Ferreira, R.; Motta, M. A.; Castro-Neto, A. G.; Vieira, A. A. S.; Silva, D. C. N.; Fontes, A.; Cesar, C. L., Highly fluorescent semiconductor core–shell CdTe–CdS nanocrystals for monitoring living yeast cells activity *Applied Physics A: Materials Science & Processing* **2007**, 89, (4), 957-961.

(9) Lin, H. Y.; Chen, Y. F.; Wu, J. G.; Wang, D. I.; Chen, C. C., Carrier transfer induced photoluminescence change in metal-semiconductor core-shell nanostructures; *Appl. Phys. Lett.* **2006**, 88, 161911.

(10) Kamat, P. V.; Shanghavi, B., Interparticle Electron Transfer in Metal/Semiconductor Composites. Picosecond Dynamics of CdS-Capped Gold Nanoclusters; *J. Phys. Chem. B* **1997**, 101, (39), 7675–7679.

(11) Ma, G. H.; He, J.; Rajiv, K.; Tang, S. H.; Yang, Y.; Nogami, M., Observation of resonant energy transfer in Au:CdS nanocomposite; *Appl. Phys. Lett.* **2004**, 84, (23), 4684-4686.

(12) Yang, Y.; Nogami, M.; Shi, J.; Chen, H.; Liu, Y.; Qian, S., Ultrafast electron dynamics and enhanced optical nonlinearities of CdS-capped Au/$BaTiO_3$ composite film; *J. Appl. Phys.* **2005**, 98, 033528.

(13) Yang, Y.; Shi, J.; Chen, H.; Dai, S.; Liu, Y., Enhanced off-resonance optical nonlinearities of Au@CdS core-shell nanoparticles embedded in $BaTiO_3$ thin films; *Chem. Phys. Lett.* **2003**, 37, (1-2), 1-6.

(14) Honma, I.; Sano, T.; Komiyama, H., Surface-enhanced Raman scattering (SERS) for semiconductor microcrystallites observed in silver-cadmium sulfide hybrid particles; *J. Phys. Chem.* **1993**, 97, (25), 6692–6695.

(15) Lu, W.; Wang, B.; Zeng, J.; Wang, X.; Zhang, S.; Hou, J. G., Synthesis of Core/Shell Nanoparticles of Au/CdSe via Au−Cd Bialloy Precursor; *Langmuir* **2005**, 21, (8), 3684–3687.

(16) Sharma, A. K.; Gupta, B. D., Metal–semiconductor nanocomposite layer based optical fibre surface plasmon resonance sensor; *J. Opt. A: Pure Appl. Opt.* **2007**, 9, 180-185.

(17) Lu, Y.; Yin, Y.; Li, Z.-Y.; Xia, Y., Synthesis and Self-Assembly of Au@SiO_2 Core−Shell Colloids; *Nano Lett* **2002**, 2, (7), 785–788.

(18) Lu, Y.; Yin, Y.; Mayers, B. T.; Xia, Y., Modifying the Surface Properties of Superparamagnetic Iron Oxide Nanoparticles through A Sol−Gel Approach; *Nano Lett* **2002**, 2, (3), 183–186.

(19) Venkatasamy, V.; Jayaraju, N.; Cox, S. M.; Thambidurai, C.; Happek, U.; Stickney, J. L., Optimization of CdTe nanofilm formation by electrochemical atomic layer epitaxy (EC-ALE); *Journal of Applied Electrochemistry* **2006**, 36, (11), 1223-1229.

(20) Vaidyanathan, R.; Cox, S. M.; Happek, U.; Banga, D.; Mathe, M. K.; Stickney, J. L., Preliminary Studies in the Electrodeposition of PbSe/PbTe Superlattice Thin Films via Electrochemical Atomic Layer Deposition (ALD), Part of the Electrochemistry special issue.; *Langmuir* **2006**, 22, (25), 10590–10595.

(21) Muthuvel, M.; Stickney, J. L., CdTe Electrodeposition on InP(100) via Electrochemical Atomic Layer Epitaxy (EC-ALE): Studies Using UHV-EC; *Langmuir* **2006**, 22, (12), 5504–5508.

(22) Gichuhi, A.; Boone, B. E.; Shannon, C., Electrosynthesized CdS/HgS Heterojunctions; *Langmuir* **1999**, 15, (3), 763–766.

(23) Zhu, W.; Yang, J.-Y.; Zhou, D.-X.; Xiao, C.-J.; Duan, X.-K., Electrochemical Aspects and Structure Characterization of VA-VIA Compound Semiconductor Bi_2Te_3/Sb_2Te_3 Superlattice Thin Films via Electrochemical Atomic Layer Epitaxy; *Langmuir* **2008**, 24, (11), 5919–5924.

(24) Wade, T. L.; Vaidyanathan, R.; Happek, U.; Stickney, J. L., Electrochemical formation of a III–V compound semiconductor superlattice: InAs/InSb; *Journal of Electroanalytical Chemistry* **2001**, 500, (1-2), 322-332

(25) Torimoto, T.; Obayashi, A.; Kuwabata, S.; Yoneyama, H., Electrochemical preparation of ZnS/CdS superlattice and its photoelectrochemical properties; *Electrochem. Commun.* **2000**, 2, (5), 359-362.

(26) Zou, S.; Weaver, M. J., Surface-enhanced Raman spectroscopy of cadmium sulfide/cadmium selenide superlattices formed on gold by electrochemical atomic-layer epitaxy *Chemical Physics Letters* **1999**, 312, (2-4), 101-107

(27) Kim, Y.-G.; Kim, J. Y.; Thambidurai, C.; Stickney, J. L., Pb Deposition on I-Coated Au(111). UHV-EC and EC-STM Studies; *Langmuir* **2007**, 23, (5), 2539–2545.

(28) Kim, Y.-G.; Kim, J. Y.; Vairavapandian, D.; Stickney, J. L., Platinum Nanofilm Formation by EC-ALE via Redox Replacement of UPD Copper: Studies Using in-Situ Scanning Tunneling Microscopy; *J. Phys. Chem. B* **2006**, 110, (36), 17998–18006.

(29) Lyon, D. K.; Miller, W. K.; Novet, T.; Domaille, P. J.; Evitt, E.; Johnson, D. C.; Finke, R. G., Highly oxidation resistant inorganic-porphyrin analog polyoxometalate oxidation catalysts. 1. The synthesis and characterization of aqueous-soluble potassium salts of α_2-

$P_2W_{17}O_{61}(M^{n+}\cdot OH_2)^{(n-10)}$ and organic solvent soluble tetra-n-butylammonium salts of α_2-$P_2W_{17}O_{61}(M^{n+}\cdot Br)^{(n-11)}$ (M = Mn^{3+},Fe^{3+},Co^{2+},Ni^{2+},Cu^{2+}); *J. Am. Chem. Soc.* **1991**, 113, (19), 7209–7221.

(30) Şişman, İ.; Alanyalioglu, M.; Demir, Ü., Atom-by-Atom Growth of CdS Thin Films by an Electrochemical Co-deposition Method: Effects of pH on the Growth Mechanism and Structure; *J. Phys. Chem. C* **2007**, 111, (6), 2670–2674.

(31) Hsiao, G. S.; Anderson, M. G.; Gorer, S.; Harris, D.; Penner, R. M., Hybrid Electrochemical/Chemical Synthesis of Supported, Luminescent Semiconductor Nanocrystallites with Size Selectivity: Copper(I) Iodide; *J. Am. Chem. Soc.* **1997**, 119, (6), 1439–1448.

(32) Inukai, J.; Osawa, Y.; Itaya, K., Adlayer Structures of Chlorine, Bromine, and Iodine on Cu(111) Electrode in Solution: In-Situ STM and ex-Situ LEED Studies; *J. Phys. Chem. B* **1998**, 102, (49), 10034–10040.

(33) Broekmann, P.; Haia, N. T. M.; Wandelta, K., 2D compound formation during copper dissolution: An electrochemical STM study; *Surface Science* **2006**, 600, (18), 3971-3977

(34) Hai, N. T. M.; Huemann, S.; Hunger, R.; Jaegermann, W.; Wandelt, K.; Broekmann, P., Combined Scanning Tunneling Microscopy and Synchrotron X-Ray Photoemission Spectroscopy Results on the Oxidative CuI Film Formation on Cu(111); *J. Phys. Chem. C* **2007**, 111, (40), 14768–14781.

(35) Stickney, J. L.; Wade, T. L.; Flowers, B. H.; Vaidyanathan, R.; Happek, U. *Electrodeposition of compound semiconductors by electrochemical atomic layer epitaxy*; In *Encyclopedia of Electrochemistry, Volume 1, Thermodynamics and Electrified Interfaces*; Bard, A. J., Stratmann, M., Gileadi, E., Urbakh, M., Eds.; Wiley: New Yrok, 2003, p 516–560.

(36) Arrigan, D. W. M.; Iqbal, T.; Pickup, M. J., Underpotential Deposition of Copper at Mercaptoalkane Sulfonate-Coated Polycrystalline Gold; *Electroanalysis* **2001**, 13, (8-9), 751 - 754.

(37) Zhai, J.; Huang, M.; Dong, S., Electrochemical Designing of Au/Pt Core Shell Nanoparticles as Nanostructured Catalyst with Tunable Activity for Oxygen Reduction; *Electroanalysis* **2006**, 19, (4), 506 - 509.

(38) Zheng, Z.; Liu, A.; Wang, S.; Huang, B.; Wong, K. W.; Zhang, X.; Hark, S. K.; Lau, W. M., Growth of highly oriented (110) γ-CuI film with sharp exciton band; *J. Mater. Chem.* **2008**, 18, 852-854.

(39) Cao, G., *Nanostructures & Nanomaterials: Synthesis, Properties & Applications* Imperial College Press: London, UK, 2004.

(40) Gichuhi, A.; Boone, B. E.; Shannon, C., Resonance Raman scattering and scanning tunneling spectroscopy of CdS thin films grown by electrochemical atomic layer epitaxy—thickness dependent phonon and electronic properties; *Journal of Electroanalytical Chemistry* **2002**, 522, (1), 21-25

(41) Serrano, J.; Cardona, M.; Ritter, T. M.; Weinstein, B. A.; Rubio, A.; Lin, C. T., Pressure and temperature dependence of the Raman phonons in isotopic γ-CuI; *Phys. Rev. B* **2002**, 66, (24), 245202.

(42) Boone, B. E.; Shannon, C., Optical Properties of Ultrathin Electrodeposited CdS Films Probed by Resonance Raman Spectroscopy and Photoluminescence; *J. Phys. Chem.* **1996**, 100, (22), 9480–9484.

(43) Dzhagan, V.; Valakh, M. Y.; Kolny-Olesiak, J.; Lokteva, I.; Zahn, D. R. T., Resonant Raman study of phonons in high-quality colloidal CdTe nanoparticles; *Appl. Phys. Lett.* **2009**, 94, 243101.

(44) Orazem, M. E.; Tribollet, B., *Electrochemical Impedance Spectroscopy*; John Wiley & Sons, Inc: Hoboken, NJ, 2008.

(45) Bott, A. W., Electrochemistry of Semiconductors; *Current Separations* **1998**, 17, (3), 87-91.

(46) Myamlin, V. A.; Pleskov, Y. V., *Electrochemistry of Semiconductors*; Plenum Press: New York, NY, 1967.

(47) Morrison, S. R., *Electrochemistry at semiconductor and oxidized metal electrodes*; Plenum Press: New York, NY, 1980.

(48) Nozik, A. J.; Memming, R., Physical Chemistry of Semiconductor-Liquid Interfaces; *J. Phys. Chem.* **1996**, 100, (31), 13061-13078.

(49) Madelung, O.; Rössler, U.; Schulz, M. *Cuprous iodide (gamma-CuI) dielectric constants, refractive index*; In *II-VI and I-VII Compounds; Semimagnetic Compounds*; Springer-Verlag: 1999; Vol. 41, p 1-5.

(50) Zhou, S., Dielectric properties of phase-size-control CdS nanoparticles and conventional powders; *physica status solidi (a)* **2003**, 200, (2), 423 - 428.

(51) Mathew, X.; Sebastian, P. J.; Sanchez, A.; Campos, J., Structural and opto-electronic properties of electrodeposited CdTe on stainless steel foil; *Solar Energy Materials & Solar Cells* **1999**, 59, (1-2), 99-114.

(52) Hagihara, T.; Sakiyama, N.; Okushiba, H.; Hayashiuchi, Y., Characteristic charge transport processes in cuprous iodide crystals; *Osaka Kyoiku Daigaku Kiyo, Dai-3-bumon* **1989**, 38, (2), 87-95.

(53) Kokubun, Y.; Watanabe, H.; Wada, M., Electrical Properties of CuI Thin Films; *Japanese Journal of Applied Physics* **1971**, 10, (7), 864-867.

(54) Wang, Q.-Z.; Wang, Z.-H., Electrochemical Preparation and Properties of CuI Semiconductor Film; *Chinese Journal of Applied Chemistry* **2006**, 23, (10), 1161-1165.

(55) Yang, X.; Xu, C.; Giles, N. C., Intrinsic electron mobilities in CdSe, CdS, ZnO, and ZnS and their use in analysis of temperature-dependent Hall measurements; *J. Appl. Phys.* **2008**, 104, 073727.

(56) Murali, K. R.; Thilagavathy, K.; Oommen, R., Pulse plated CdS films and their characteristics; *ECS Trans.* **2008**, 11, (28, Electrodeposition of Nanoengineered Materials and Alloys 2), 75-81.

(57) Davila-Pintle, J. A.; Lozada-Morales, R.; Palomino-Merino, M. R.; Rivera-Marquez, J. A.; Portillo-Moreno, O.; Zelaya-Angel, O., Electrical properties of Er-doped CdS thin films; *J. Appl. Phys.* **2007**, 101, (1), 013712/013711-013712/013715.

(58) Liu, K.; Zhang, J. Y.; Wu, X.; Li, B.; Li, B.; Lu, Y.; Fan, X.; Shen, D., Fe-doped and (Zn, Fe) co-doped CdS films: Could the Zn doping affect the concentration of Fe2+ and the optical properties?; *Phys. B (Amsterdam, Neth.)* **2007**, 389, (2), 248-251.

(59) Abu-Safe, H. H.; Hossain, M.; Naseem, H.; Brown, W.; Al-Dhafiri, A., Chlorine-doped CdS thin films from CdCl2-mixed CdS powder; *J. Electron. Mater.* **2004**, 33, (2), 128-134.

(60) Vigil, O.; Zelaya-Angel, O.; Rodriguez, Y.; Morales-Acevedo, A., Electrical characterization of chemically deposited CdS thin films under magnetic field application; *Phys. Status Solidi A* **1998**, 167, (1), 143-150.

(61) Tomas, S. A.; Stolik, S.; Altuzar, V.; Zelaya, O.; Lozada, R.; Carmona, J. J.; Portillo, O.; Davila, J. A., Characterization of chemical-bath-deposited CdS thin films doped with methylene blue; *Rev. Sci. Instrum.* **2003**, 74, (1, Pt. 2), 569-571.

(62) Sankar, N.; Sanjeeviraja, C.; Ramachandran, K., Growth and characterization of CdS and doped CdS single crystals; *J. Cryst. Growth* **2002**, 243, (1), 117-123.

(63) Shahane, G. S.; Deshmukh, L. P., Structural and electrical transport properties of $CdS_{0.9}Se_{0.1}$:In thin films: effect of film thickness; *Mater. Chem. Phys.* **2001**, 70, (1), 112-116.

(64) Hong, K. J.; Jeong, T. S.; Yoon, C. J.; Shin, Y. J., The optical properties of CdS crystal grown by the sublimation method; *J. Cryst. Growth* **2000**, 218, (1), 19-26.

(65) Ramaiah, K. S.; Raja, V. S.; Sharon, M., Optical and structural investigations on spray-deposited CdS films; *J. Mater. Sci.: Mater. Electron.* **1998**, 9, (4), 261-265.

(66) Mohanchandra, K. P.; Uchil, J., Electrical properties of CdS and CdSe films deposited on vibrating substrates; *J. Appl. Phys.* **1998**, 84, (1), 306-310.

(67) Joshi, S. S.; Lokhande, C. D., Electrodeposited heterojunctions based on cadmium chalcogenide, CdX (X = S, Se, Te) and polyaniline; *J. Mater. Sci.* **2007**, 42, (4), 1304-1308.

(68) Matsumoto, H.; Uchida, H.; Matsunaga, T.; Tanaka, K.; Sakata, T.; Mori, H.; Yoneyama, H., Photoinduced Reduction of Viologens on Size-Separated CdS Nanocrystals; *J. Phys. Chem.* **1994**, 98, (44), 11549-11556.

(69) Finlayson, M. F.; Wheeler, B. L.; Kakuta, N.; Park, K. H.; Bard, A. J.; Campion, A.; Fox, M. A.; Webber, S. E.; White, J. M., Determination of flat-band position of cadmium

sulfide crystals, films, and powders by photocurrent and impedance techniques, photoredox reaction mediated by intragap states; *J. Phys. Chem.* **1985**, 89, (26), 5676-5681.

(70) Reeves, J. H.; Cocivera, M., Comparison of behavior of single-crystal and polycrystalline cadmium sulfide in photoelectrochemical cells; *J. Electrochem. Soc.* **1984**, 131, (9), 2042-2047.

(71) Errandonea, D.; Segura, A.; Martinez-Garcia, D.; Munoz-San Jose, V., Hall-effect and resistivity measurements in CdTe and ZnTe at high pressure. Electronic structure of impurities in the zinc-blende phase and the semimetallic or metallic character of the high-pressure phases; *Phys. Rev. B: Condens. Matter Mater. Phys.* **2009**, 79, (12), 125203/125201-125203/125206.

(72) Su, C.-H., Energy band gap, intrinsic carrier concentration, and Fermi level of CdTe bulk crystal between 304 and 1067 K; *J. Appl. Phys.* **2008**, 103, (8), 084903/084901-084903/084906.

(73) Vigil-Galan, O.; Sanchez-Meza, E.; Sastre-Hernandez, J.; Cruz-Gandarilla, F.; Marin, E.; Contreras-Puente, G.; Saucedo, E.; Ruiz, C. M.; Tufino-Velazquez, M.; Calderon, A., Study of the physical properties of Bi doped CdTe thin films deposited by close space vapor transport; *Thin Solid Films* **2008**, 516, (12), 3818-3823.

(74) Grushko, E. V.; Maslyanchuk, O. L.; Mathew, X.; Motushchuk, V. V.; Kosyachenko, L. A.; Streltsov, E. A., Spectral distribution of photoelectric quantum yield of thin-film Au-CdTe diode structure; *Semicond. Phys., Quantum Electron. Optoelectron.* **2007**, 10, (4), 15-20.

(75) Murali, K. R.; Jayasutha, B., Properties of CdTe films brush plated on high temperature substrates; *Mater. Sci. Semicond. Process.* **2007**, 10, (1), 36-40.

(76) Veeramani, P.; Haris, M.; Kanjilal, D.; Asokan, K.; Babu, S. M., Investigation of swift heavy ion irradiation effects in CdTe crystals; *J. Phys. D: Appl. Phys.* **2006**, 39, (13), 2707-2710.

(77) Abbas Shah, N.; Ali, A.; Aqili, A. K. S.; Maqsood, A., Physical properties of Ag-doped cadmium telluride thin films fabricated by closed-space sublimation technique; *J. Cryst. Growth* **2006**, 290, (2), 452-458.

(78) Arai, K.; Murase, K.; Hirato, T.; Awakura, Y., Effect of Chloride Ions on Electrodeposition of CdTe from Ammoniacal Basic Electrolytes; *J. Electrochem. Soc.* **2006**, 153, (2), C121-C126.

(79) Lovergine, N.; Prete, P.; Tapfer, L.; Marzo, F.; Mancini, A. M., Hydrogen transport vapour growth and properties of thick CdTe epilayers for RT X-ray detector applications; *Cryst. Res. Technol.* **2005**, 40, (10-11), 1018-1022.

(80) Belas, E.; Franc, J.; Grill, R.; Toth, A. L.; Horodysky, P.; Moravec, P.; Hoeschl, P., Regular and anomalous-type conversion of p-CdTe during Cd-rich annealing; *J. Electron. Mater.* **2005**, 34, (6), 957-962.

(81) Paranchych, S. Y.; Paranchych, L. D.; Makogonenko, V. N.; Tanasyuk, Y. V.; Andriichuk, M. D.; Romanyuk, V. R., The Physical Properties of CdTe Doped with V and Ge; *Semiconductors* **2005**, 39, (6), 712-715.

(82) Nikoniuk, E. S.; Zakharuk, Z. I.; Rarenko, I. M.; Kuchma, M. I.; Yurijchuk, I. M., Characterization of CdTe + Mn crystals depending on doping procedure; *Semicond. Phys., Quantum Electron. Optoelectron.* **2003**, 6, (2), 160-163.

(83) White, H. S.; Rlcco, A. J.; Wrighton, M. S., Characterization of p-type cadmium telluride electrodes in acetonitrile/electrolyte solutions. Nearly ideal behavior from reductive surface pretreatments. ; *J. Phys. Chem.* **1983**, 87, (25), 5140-5150.

(84) Licht, S., Developments in photoelectrochemistry: light-addressable photoelectrochemical cyanide sensors; *Colloids Surf., A* **1998**, 134, (1/2), 231-239.

(85) Halperin, W. P., Quantum size effects in metal particles; *Rev. Mod. Phys.* **1986**, 58, (3), 533-606.

(86) Gryse, R. D.; Gomes, W. P.; Cardon, F.; Vennik, J., On the Interpretation of Mott-Schottky Plots Determined at Semiconductor/Electrolyte Systems; *J. Electrochem. Soc.* **1975**, 122, (5), 711-712.

(87) Zimmer, A.; Stein, N.; Johann, L.; Terryn, H.; Boulanger, C., Characterizations of bismuth telluride films from Mott-Schottky plot and spectroscopic ellipsometry; *Surface and Interface Analysis* **2007**, 40, (3-4), 593 - 596.

(88) Gu, C.; Xu, H.; Park, M.; and Shannon, C., Synthesis of Metal-Semiconductor Core-Shell Nanoparticles Using Electrochemical Surface-Limited Reactions; *Langmuir*, **2009**, 25, (1), 410-414.

Chapter 4.

Large Nanostructures using Sandwich Polyoxometalates and Silver Nanoparticles as Building Blocks

4.1 Introduction

4.1.1 Nanoparticles

Nanoparticles are of great scientific interest because their unique properties similar to neither bulk materials nor atomic or molecular structures. Although they are often considered a modern invention, nanoparticles actually have been used long time ago by the 9th century ceramists for generating a glittering effect on the surface of pots. The formal scientific re-visit of nanoparticles started by Faraday in his 1857 paper[1], where he described the optical properties of nanometer-scale metals. However, there was no intensive investigation due to the lack of proper chemical and physical properties characterization instruments.

Bulk materials have constant physical properties regardless of its size. The properties change as the materials' size approaches the nano-scale and as the percentage of atoms at the surface of a material becomes significant. Unlike those bulk materials larger than one micrometer, nano-scale materials have size-dependent properties, such as quantum confinement in semiconductor particles, surface plasmon resonance in somemetal particles and superparamagnetism in magnetic materials. The interesting and sometimes unexpected properties

of nanoparticles are due to the surface-to volume ratio, which means that the aspects of the surface of the material dominating the properties instead of the bulk properties.

Silver nanoparticle is one of the most widely used substrates for surface enhanced spectroscopy (SERS). Its plasmon resonance frequencies fall within the wavelength ranges of visible and Near-Infrared, providing maximal enhancement to probe a single molecule[2]. Also, silver nanoparticle is of particular interest because of its good conductivity, chemical stability, catalytic and antibacterial activity[3].

4.1.2 Nanoparticles preparation using Polyoxometalates

There are two approaches are used in making nanoparticles. In the "bottom-up" approach, materials and devices are built from molecular components which assemble themselves chemically by principles of molecular recognition. A good example is chemical reduction. In the "top-down" approach, nano-objects are constructed from larger entities without atomic-level control, such as mechanical attrition. In chemical reduction, metal cation (M^{n+}) is reduced to its element form (M) by a reducing agent. As more and more of these metal atoms form, the solution becomes supersaturated, and metal gradually starts to precipitate in the form of sub-nanometer particles. The rest of the metal atoms will grow on the surface of the existing particles. To prevent these particles from aggregating, some sort of stabilizing agent that sticks to the nanoparticles surface is usually added.

Usually the reducing agent and the stabilizing agent are separate chemicals. But there are many single reagents that can perform dual functions, both reducing and stabilizing, which give great convenience in preparing and processing nanoparticles solutions. The selection of reducing

and the stabilizing agents are based on the fabrication environment and application purpose of the nanoparticles. Some polymer stabilizers are not suitable for making nanoparticles for electrochemical reactions because they block electron transfer.

Polyoxometalate is one of the dual-function reagents. It has been used in fabrication of Gold[4,5], Silver[4-7], Platinum[5,8-10], Palladium[5,8,9,11], Rhodium[12], Copper[7], Cadmium[7], Thallium[7], Lead[7], Cobalt[7], Nickel[7] and Iridium[13] nanoparticles. Apart from reducing and stabilizing, fast electron transfer capability and high proton conducting ability makes polyoxometalates as an attractive reagent to prepare nanoparticles, especially for those with electrochemical applications. Polyoxometalates can ensure enhanced availability and mobility of the protons as well as electrons at the nanostructure surface[14,15]. Also, preparing Silver nanoparticles using polyoxometalates is considered to be a "green method" [16].

In this chapter, silver nanostructure prepared by Keggin type and sandwich type polyoxometalates will be explored.

4.2 Experimental

4.2.1 Materials and reagents

Methanol (99.9%, Fisher Chemical), Nitric acid (Fisher Chemical) with a nominal composition of 68–70% HNO_3, $Na_3PW_{12}O_{40}\cdot 2H_2O$ (>99.9%, Sigma–Aldrich), $Na_2WO_4\cdot 2H_2O$ (99.995%, Sigma–Aldrich), $Zn(NO_3)_2\cdot 6H_2O$ (>99.9%, Sigma–Aldrich), $AgNO_3$ (99+%, Arcos Organics), and $NaBH_4$ (99%, Arcos Organics) were used as received without further purification. Millipore-Q purified distilled water (18MΩ/cm) was used to make up all solutions.

4.2.2 Preparation of sandwich polyoxometalate $Na_{12}[WZn_3(H_2O)_2(ZnW_9O_{34})_2]$:

The synthetic procedure developed by Tourné et al[17], was employed for the preparation of the zinc sandwich polyoxometalate $Na_{12}[WZn_3(H_2O)_2(ZnW_9O_{34})_2]$. A solution of $Na_2WO_4{\cdot}2H_2O$ (32 g) in water (87.5ml) was treated with nitric acid (14N, 0.5 ml) at 80-85º C with vigorous stirring, until the initial precipitate dissolved completely to form a dark yellow solution. Then a solution of zinc nitrate (7.5g) in water (25ml) was added very slowly, accompanied by continuous stirring and heating at 90-95ºC (without boiling). A burette with stopcock was used to control speed of zinc nitrate solution addition to about 15 second per drop. During the initial addition of zinc nitrate, a white precipitate was formed, which re-dissolved immediately, and after about 2/3 addition, the precipitate started to dissolve more slowly and hence the solution was added in the speed of ~20 seconds per drop, so that the mixture remained clear till the end. This addition requires about 2-3 hours and the final pH was about 7.5. On moderate cooling to about 40 ºC, a first batch of fine needles were crystallized. The liquid was evaporated to half the volume and was left unstirred overnight. More white needle-like crystals were formed and separated by filtration. The resulting cold filtrate was treated with an equal volume of acetone to produce two separate layers. The dense lower layer was further diluted and heated to 50 ºC and maintained at this temperature overnight to extract more products. The total yield was about 75-80%. The entire collected product was subjected to recrystallization from water to yield a uniformly hydrated product.

4.2.3 Preparation of Silver nanoparticles.

Photoreduction

Photopreparation of silver nanoparticles was carried out in a Rayonet Photochemical reactor (RPR-100, Southern New England Ultraviolet Company) equipped with RPR 3500 lamps (ca. 500 $\mu W/cm^2$ for λ = 350 nm). The temperature inside the reactor was maintained at ~35°C with a cooling fan in continuous operation. $AgNO_3$ and polyoxometalate were dissolved in to a solution containing 19mL water and 1mL methanol. Then the solution was irradiated at the center of the Rayonet Photochemical UV reactor for 30 minutes to ensure all silver ions were converted to nanoparticles.

Chemical reduction

For comparison, traditional chemical reduction of Ag^+ to silver nanoparticles was performed. In a chemical reduction reaction, $AgNO_3$ and polyoxometalate were dissolved in to a solution containing 19mL water and 1mL methanol. Then a solution containing 0.1M $NaBH_4$ was added drop by drop until the mixture shows characteristic heteropoly bluecolor of reduced polyoxtalate. The blue color should fade in one day and the solution should show the color of Ag nanoparticles.

4.2.4 Characterization

UV-visible spectra were recorded on an Agilent 8453 UV-Visible Spectrophotometer with Agilent UV-Visible ChemStation software. FT-IR analysis was done on loaded transparent KBr pellets on a Shimadzu spectrometer. Raman spectroscopy was performed using the 785 nm

(300 mW) line from a wavelength-stabilized high power laser diode system (model SDL-8530, SDL Inc.) or the 514 nm line (20 mW) from an air-cooled ion laser (model 163-C42, Spectra-Physics Lasers, Inc.) as the excitation source. Raman spectra were collected and analyzed using a Renishaw inVia Raman microscope system. Crystal is analyzed using an APEX single crystal X-ray diffractometer. TEM micrographs were obtained using a Zeiss EM10 transmission electron microscope. Dynamic light scattering (DLS) tests were performed with a Nicomp 380 submicron particle sizer at a fixed measurement angle of 90˚ (internal He-Ne laser, λ=633 nm). The DLS data were processed with the software package CW388 to yield the volume-weighted size distributions. Mie theory simulation is performed using MiePlot computer program version 3.5.01.

4.3 Result and discussion

4.3.1 Structural Characterization of $Na_{12}[WZn_3(H_2O)_2(ZnW_9O_{34})_2]$

Infrared spectroscopy was employed to determine the structural integrity of the synthesized polyoxometalate. Figure 4.1 clearly shows the FT-IR characteristics of $Na_{12}[WZn_3(H_2O)_2(ZnW_9O_{34})_2]$ sandwich polyoxometalate. The FT-IR spectrum shows five distinct bands in the fingerprint region. Three prominent bands, υ(W-O, terminal) at 927 cm^{-1}, υ(W-O-W, octahedral edge sharing) at 881 cm^{-1}, and υ(W-O-W, octahedral corner sharing) 777 cm^{-1}, denoted the W-O stretching in the terminal oxo group, corner sharing WO_6 octahedra, and edge sharing octahedra in the lacunary Keggin moiety of $[WZn_3(H_2O)_2(ZnW_9O_{34})_2]^{12-}$ respectively. A medium strength shoulder band at ~700 cm^{-1}, and a low intensity band at 576 cm^{-1} show the Zn-O stretching and O-Zn-O angle bending in the center ZnO_4 tetrahedron in the

lacunary Keggin moiety of sandwich polyoxometalate respectively. A following Raman measurement also revealed the characteristic W-O peak for the Keggin moiety. Compared to the FT-IR spectra of $ZnW_{12}O_{40}^{6-}$ Keggin polyoxometalate obtained by Nomiya[18], all three W-O stretching bands in WO_6 octahedra remained at similar position with no or little shift, indicating that the as-synthesized polyoxometalate conserve Keggin moiety. However, all three bands broadened to a significant degree, suggesting that the 18 WO_6 octahedra were not in the same chemical environment due to the symmetry reduction. The broadening of Zn-O stretching band in the center ZnO_4 tetrahedron can also be attributed to it. The O-Zn-O angle bending band is often considered as a direct indicator that the center ZnO_4 unit is in regular T_d or not[18]. The band intensity was weakened in $[WZn_3(H_2O)_2(ZnW_9O_{34})_2]^{12-}$ polyanion. Its peak position shifted dramatically, from a lower energy region, 440cm^{-1} in $ZnW_{12}O_{40}^{6-}$ Keggin, to a higher energy region, 576cm^{-1} in $[WZn_3(H_2O)_2(ZnW_9O_{34})_2]^{12-}$ sandwich polyoxometalate, suggesting that there is a distortion on the tetrahedron, which confirmed that reduction of symmetry.

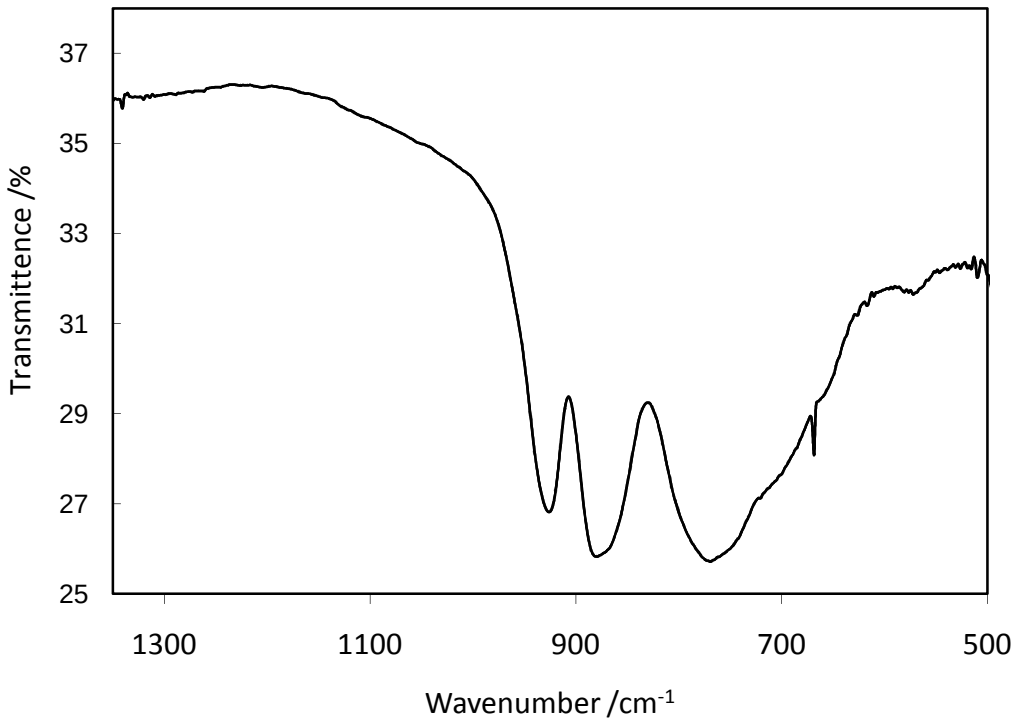

Figure 4.1 Transmission FT-IR spectrum of $Na_{12}[WZn_3(H_2O)_2(ZnW_9O_{34})_2]$ sandwich polyoxometalate in a KBr pellet.

In order to further confirm the structure, white needle shaped single crystals obtained from recrystallization of raw products were submitted for single crystal XRD analysis. Reproducible results were obtained, as shown in Figure 4.2. Two α-B-$[ZnW_9O_{34}]^{12-}$ moieties linked by a four metal atom belt. The two lobes of the sandwich are related through a center of inversion. Two zinc centers [Zn (1) and Zn (1')] at the four atom belt are five coordinate to the two α-B-$[ZnW_9O_{34}]^{12-}$ fragments, and their sixth sites are coordinated by a water molecule. W

and another Zn atom that are disordered by the inversion center occupy the remaining two positions on the belt.

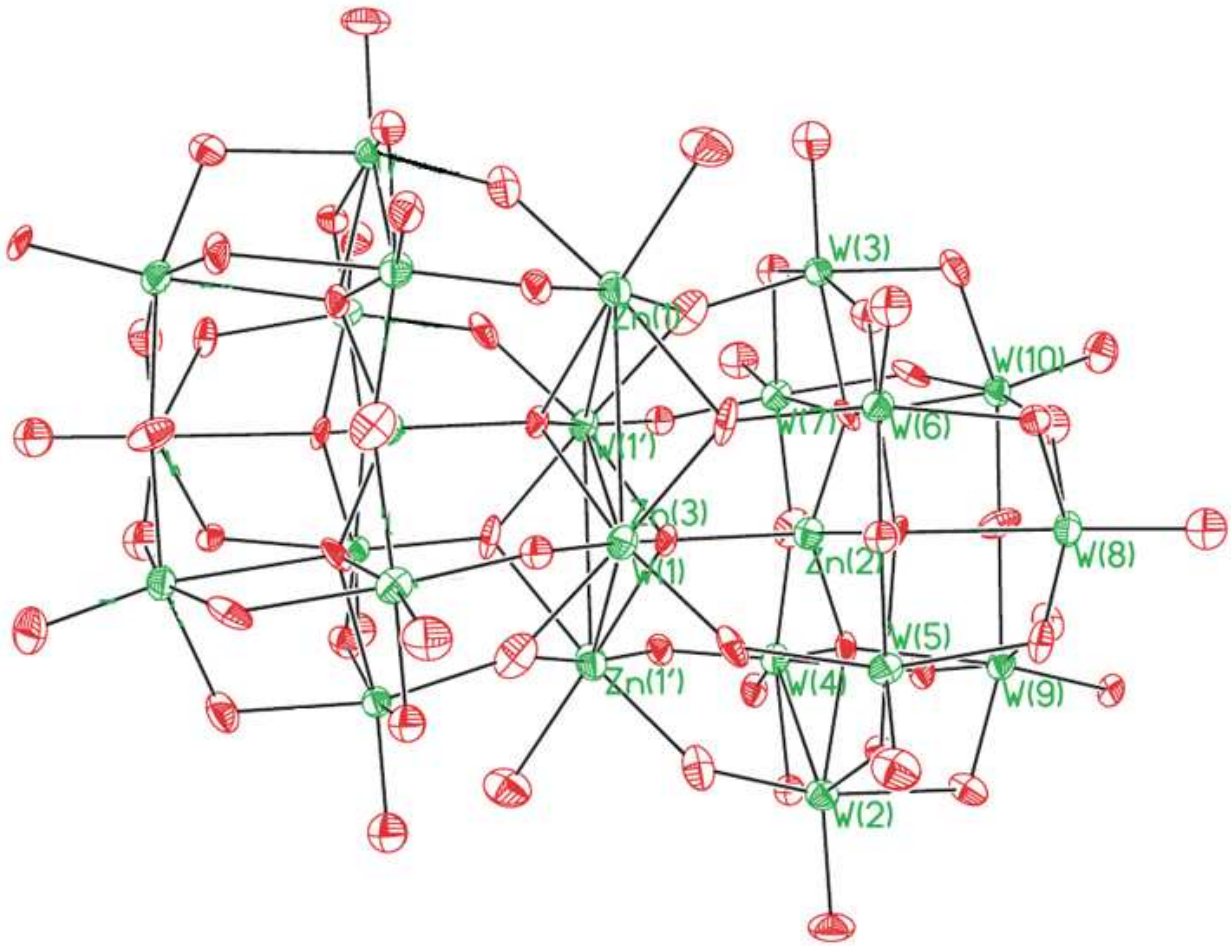

Figure 4.2 ORTEP plot of Single Crystal X ray structure of $[WZn_3(H_2O)_2(ZnW_9O_{34})_2]^{12-}$ sandwich polyoxometalate

4.3.2 UV-vis spectroscopy

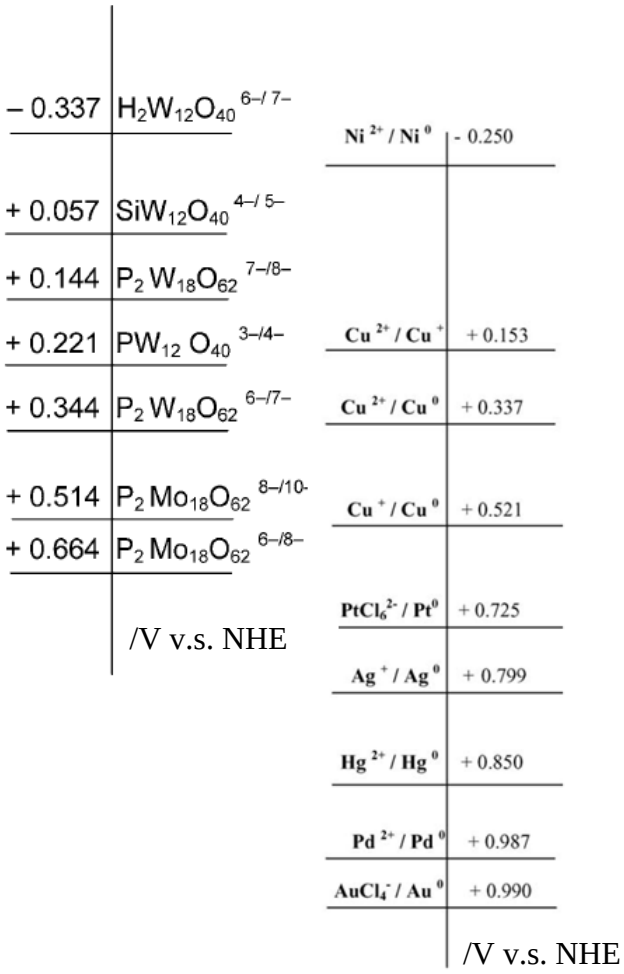

Figure 4.3 Redox potentials of polyoxometalate anions and metal ions (Volts vs. NHE).

Reproduced from Ref 19 and 20 with permission

Photo-synthesis of metal nanoparticles by polyoxometalates has been explored to a significant extent. The key of photosynthesis of metal nanoparticles by polyoxometalates is that the reduced form of polyoxometalates should be able to reduce metal ions. Many Keggin and Wells-Dawson type polyoxometalates with various oxidation states have been employed to prepare different metals nanostructures, as summarized[19,20] in Figure 4.3.

Photo-synthesis of metal nanoparticles by polyoxometalates is governed by a two-step mechanism[5]. In the first step, polyoxometalates (POM) are reduced photochemically by abstracting electrons from oxidizable organic substrates, S, under illumination of UV light, as shown in Equation (1). Then, reduced polyoxometalate reduce metal ions M^+ to the corresponding metal nanoparticles, via the route shown in Equation (2).

$$POM + S \xrightarrow{h\nu} POM(e\text{-}) + S_{ox} \qquad (1)$$

$$nPOM(e\text{-}) + nM^+ \xrightarrow{h\nu} nPOM + M^0_n \qquad (2)$$

There is one major factor that determines whether the second step, as well as the whole process, are working or not. The potential of the one-equivalent-reduced tungstate couple must be lower than potential of the metal redox couple so that the reduced POM is able to transfer the electrons efficiently to metal ions[21]. Both of our selection of polyoxometalates, $PW_{12}O_{40}^{3-/4-}$

(0.221 V v.s. NHE) and $[WZn_3(H_2O)_2(ZnW_9O_{34})_2]^{12-/13-}$ (-0.23 V v.s. NHE), have redox potentials significantly lower than Ag^+/Ag (0.799 V v.s. NHE).

Figure 4.4 Photography of as-synthesized Ag nanoparticles. 0.5mM Ag^+ — $PW_{12}O_{40}^{3-}$, 1mM Ag^+ — $PW_{12}O_{40}^{3-}$, 1.5mM Ag^+ — $[WZn_3(H_2O)_2(ZnW_9O_{34})_2]^{12-}$, 0.5mM Ag^+ — $[WZn_3(H_2O)_2(ZnW_9O_{34})_2]^{12-}$ (from left to right). The concentrations of polyoxometalate are set to 1mM.

The product photos were taken after one day of sitting in the open air to ensure there is no reduced polyoxometalate remaining. The pictures of Ag nanoparticles prepared by

photoreduction method using $PW_{12}O_{40}^{3-}$ Keggin and $[WZn_3(H_2O)_2(ZnW_9O_{34})_2]^{12-}$ sandwich type polyoxometalates show different colors, as shown in Figure 4.4.

At lower Ag^+ concentration (0.5 mM in this case), color of the colloidal silver protected by $[WZn_3(H_2O)_2(ZnW_9O_{34})_2]^{12-}$ sandwich POM is brownish red while the one prepared by $PW_{12}O_{40}^{3-}$ Keggin is light yellow. If is silver ion concentration is increased, the Keggin stabilized silver nanoparticles began agglomeration at $[Ag^+]$=1mM. In contrast, the $[WZn_3(H_2O)_2(ZnW_9O_{34})_2]^{12-}$ capped Ag nanoparticles is still stable at $[Ag^+]$=1.5mM, presenting a wine-red color. Obviously, the sandwich POM can accommodate more silver than the Keggin do.

The UV-visible spectra were collected on the above samples, which are shown in Figure 4.5. Apparently, the silver colloid made by the sandwich polyoxometalate has a different plasmon resonance peak position than the one prepared by the Keggin molecules. In the Ag^+ reduction reaction, polyoxometalates can be considered as “soluble cathodes”. They are able to trigger pure multielectron transfer reactions, which are not accompanied by the formation or breaking of bonds, acting as multielectron relays in pure-electron transfer processes as actually conventional electrodes do. Thus, the POM with more negative potential should reduce Ag^+ at a higher rate. Faster reduction leads to smaller nanoparticles with narrower size distribution as a result of favoring nucleation versus growth.

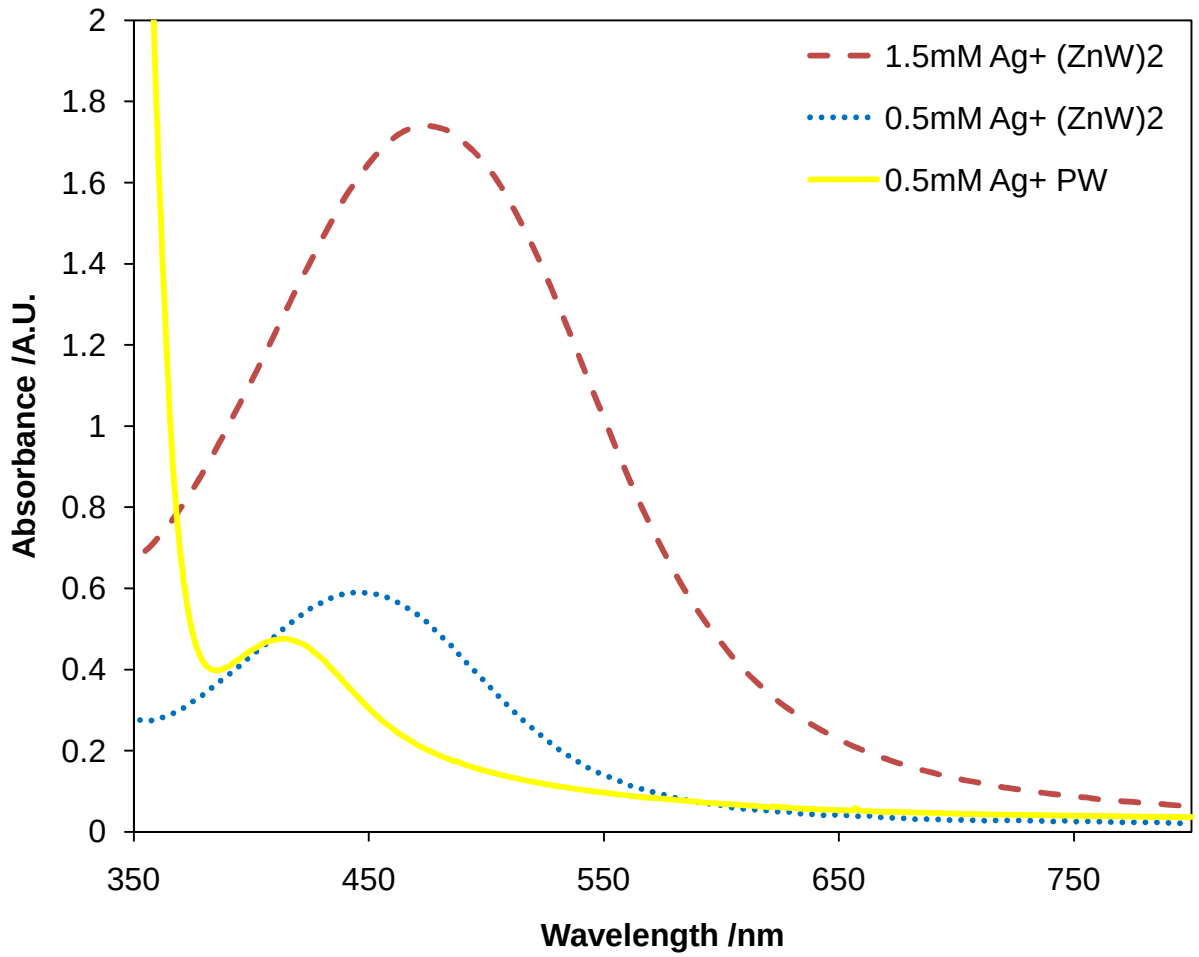

Figure 4.5 UV-visible spectra as-synthesized Ag nanoparticles. 0.5mM Ag^{+} — $PW_{12}O_{40}^{3-}$ (Yellow solid line), 1.5mM Ag^{+} — $[WZn_3(H_2O)_2(ZnW_9O_{34})_2]^{12-}$ (Red dashed line), and 0.5mM Ag^{+} — $[WZn_3(H_2O)_2(ZnW_9O_{34})_2]^{12-}$ (Blue dotted line). The concentrations of polyoxometalate are set to 1mM.

In addition, $[WZn_3(H_2O)_2(ZnW_9O_{34})_2]^{12-}$ should be able to provide better stabilization than $PW_{12}O_{40}^{3-}$ due to its higher charge density, which also favor for smaller nanocrystallines

with higher uniformity. Interestingly, with the same Ag^{+} concentration, the POM with more negative redox potential, $[WZn_3(H_2O)_2(ZnW_9O_{34})_2]^{13-}$ (-0.23 V v.s. NHE) resulted in larger size Ag colloid with a broad plasmon resonance band centered at 450 nm, while the one with more positive redox potential, $PW_{12}O_{40}^{4-}$ (0.221 V v.s. NHE) produced smaller silver nanoparticles with a narrower plasmon resonance band peaked at 420 nm. The chemical reduction method using $NaBH_4$ as reducing agent yielded the same result. Thus, the strange phenomenon should be highly related to the stabilizing polyoxometalates and is beyond explanations of either "soluble electrode" electrochemical reduction or stabilizing strength theory.

4.3.3 Transmission Electron Microscopy

To further investigate this counter-intuitive result, Transmission electron microscopy (TEM) was employed to look at as-synthesized nanoparticles. Figure 4.6 a and b show representative TEM images recorded from a drop-coated film of the Ag nanoparticles stabilized by $PW_{12}O_{40}^{3-}$ Keggin. Silver nanoparticles with average diameter of 6 nm dispersed in a matrix of polyoxometalate were observed, which is similar to published Ag nanoparticles stabilized by Keggin POM[22].

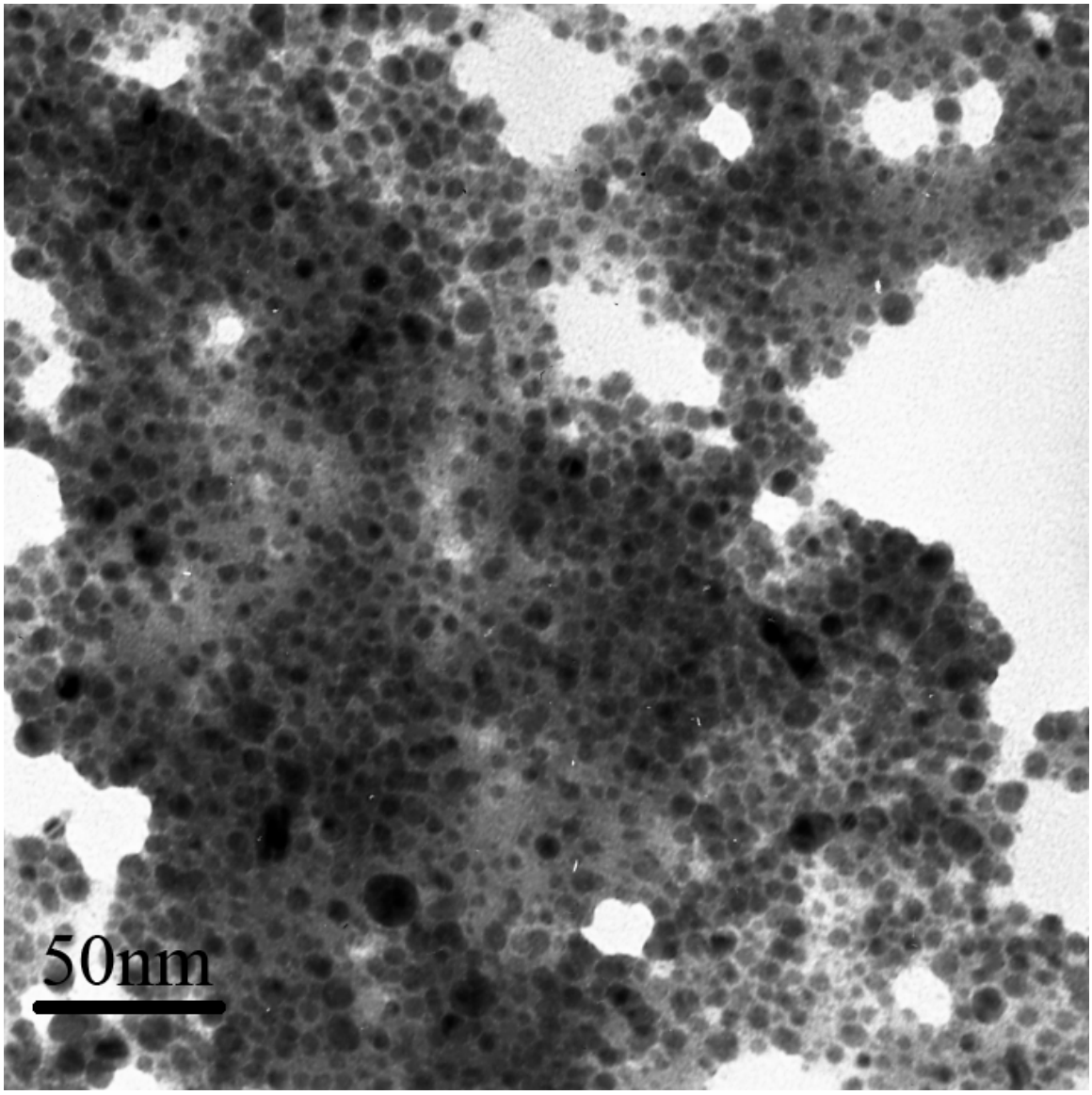

Figure 4.6a Transmission electron micrographs for Ag nanoparticles stabilized by $PW_{12}O_{40}^{3-}$ Keggin. (200k X)

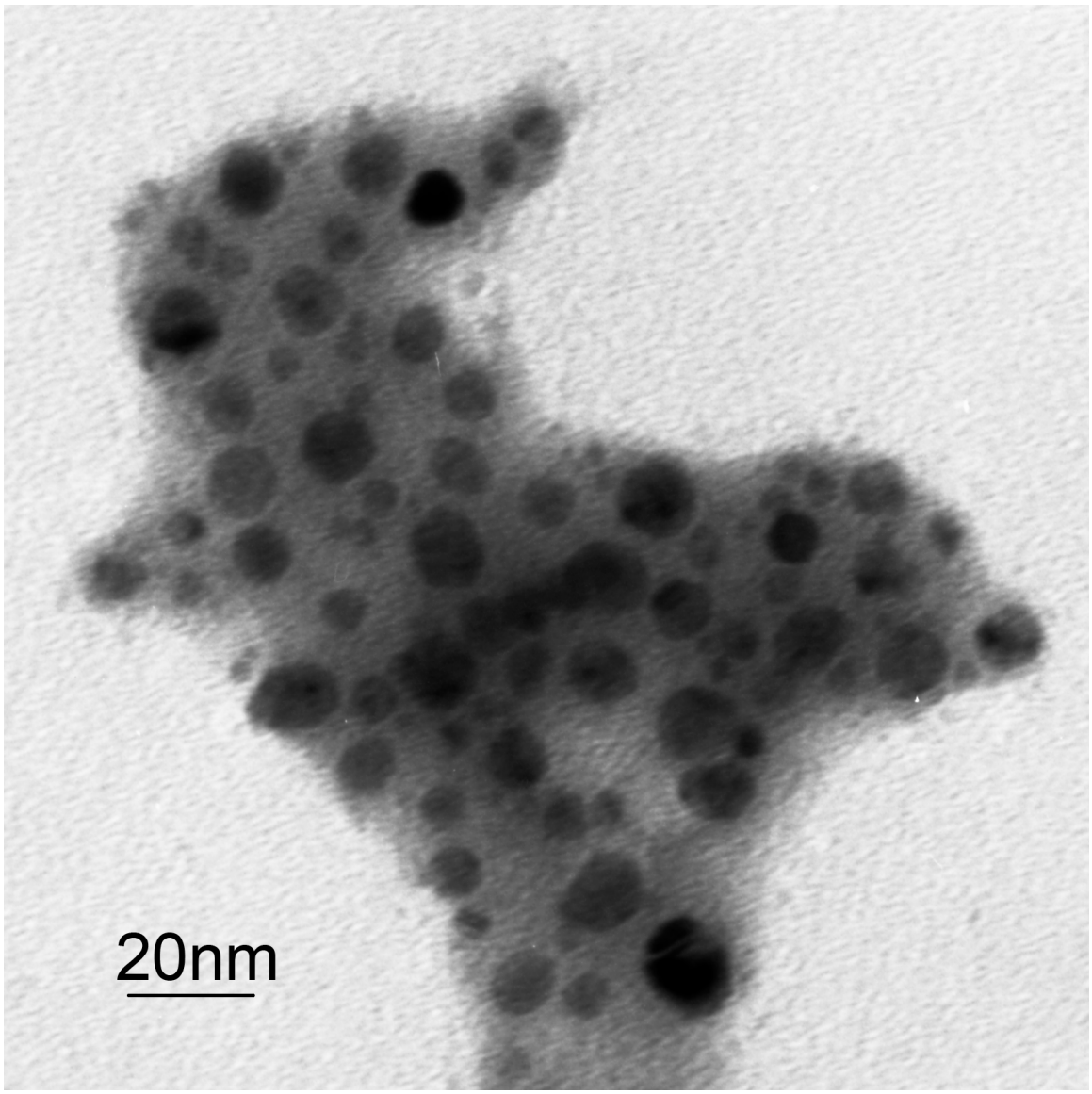

Figure 4.6b Transmission electron micrographs for Ag nanoparticles stabilized by $PW_{12}O_{40}^{3-}$ Keggin. (500k X)

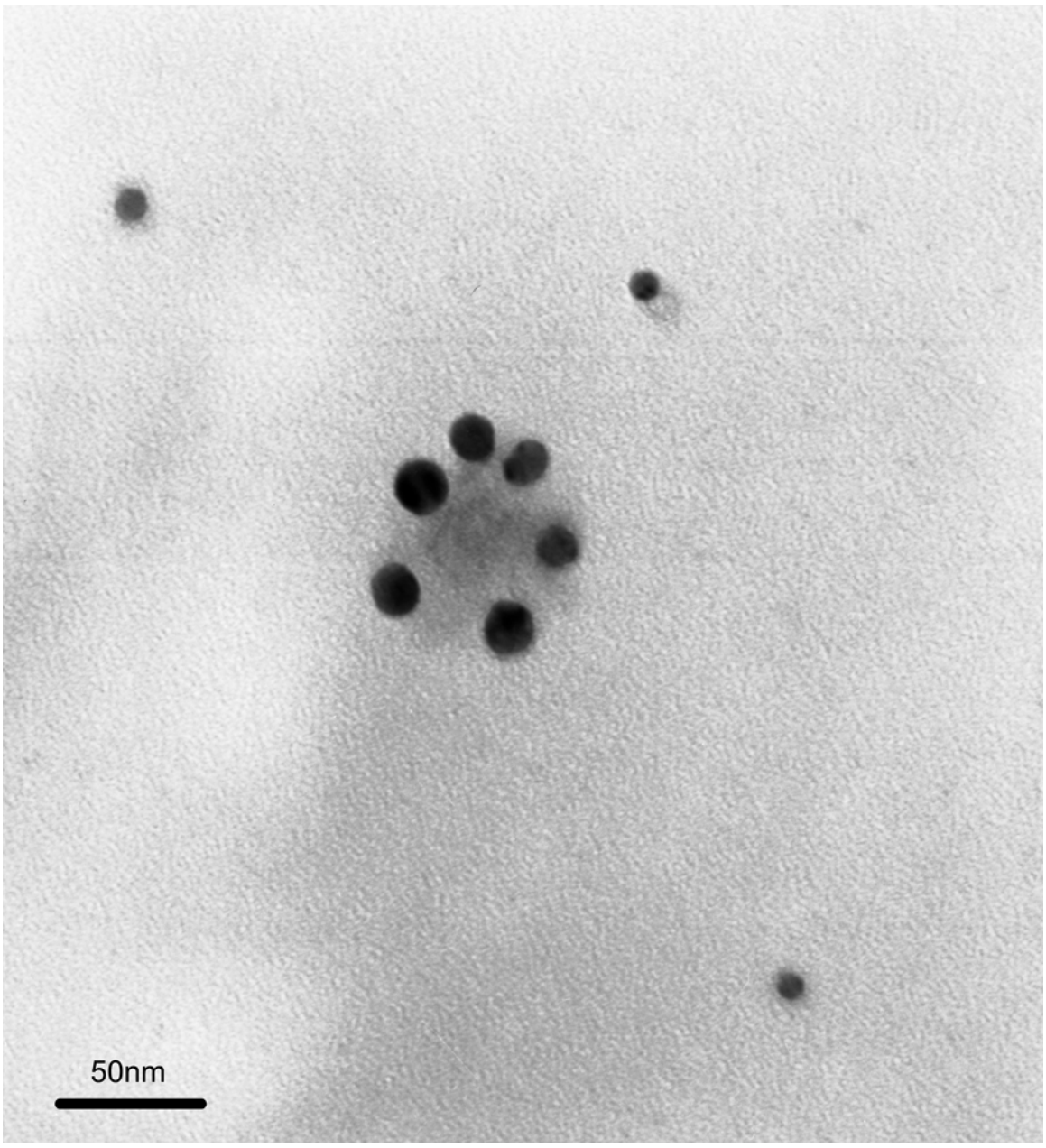

Figure 4.7a Transmission electron micrographs for Ag nanoparticles stabilized by $[WZn_3(H_2O)_2(ZnW_9O_{34})_2]^{12-}$ sandwich polyoxometalate. (200k X)

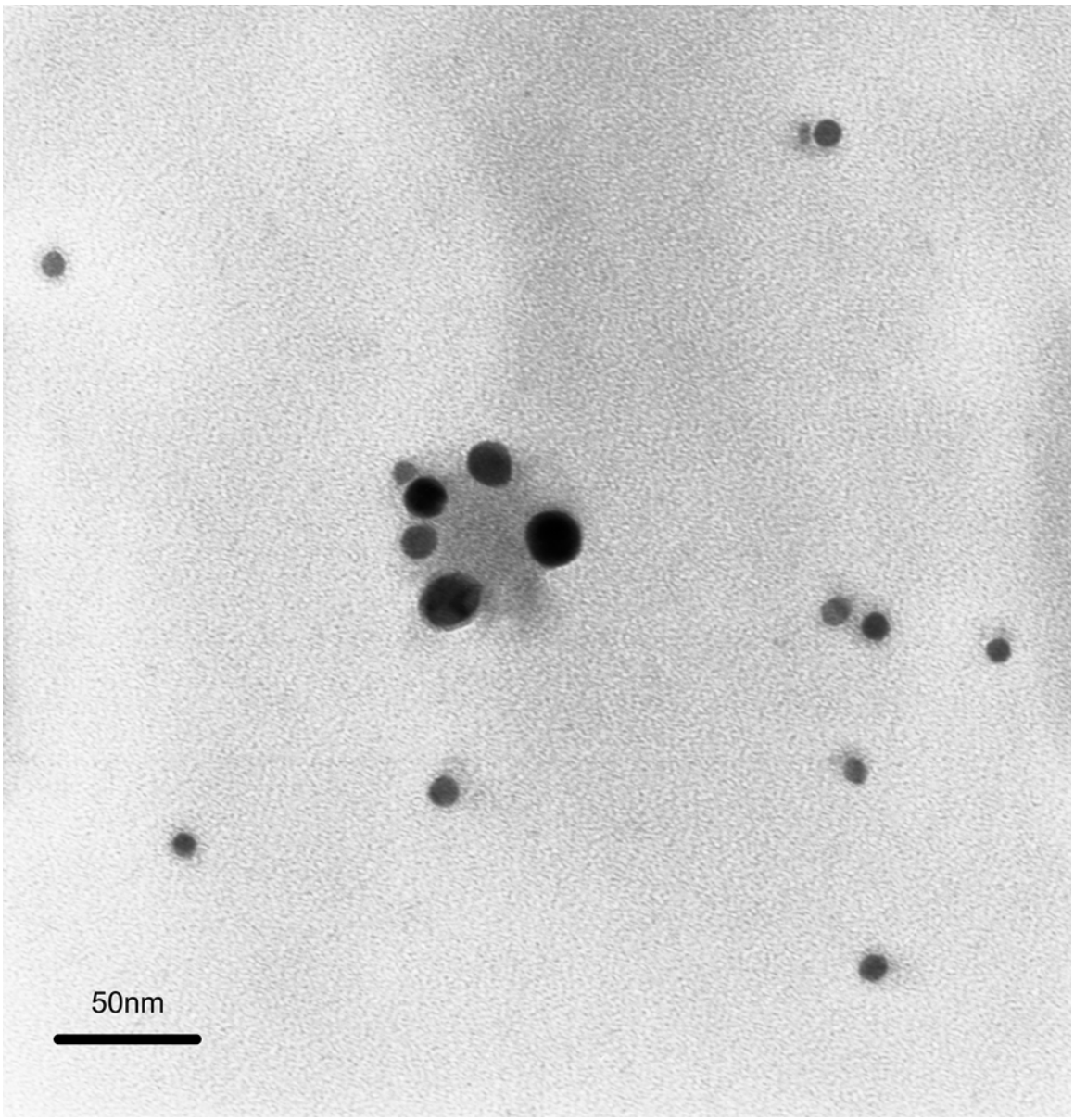

Figure 4.7b Transmission electron micrographs for Ag nanoparticles stabilized by $[WZn_3(H_2O)_2(ZnW_9O_{34})_2]^{12-}$ sandwich polyoxometalate. (200k X)

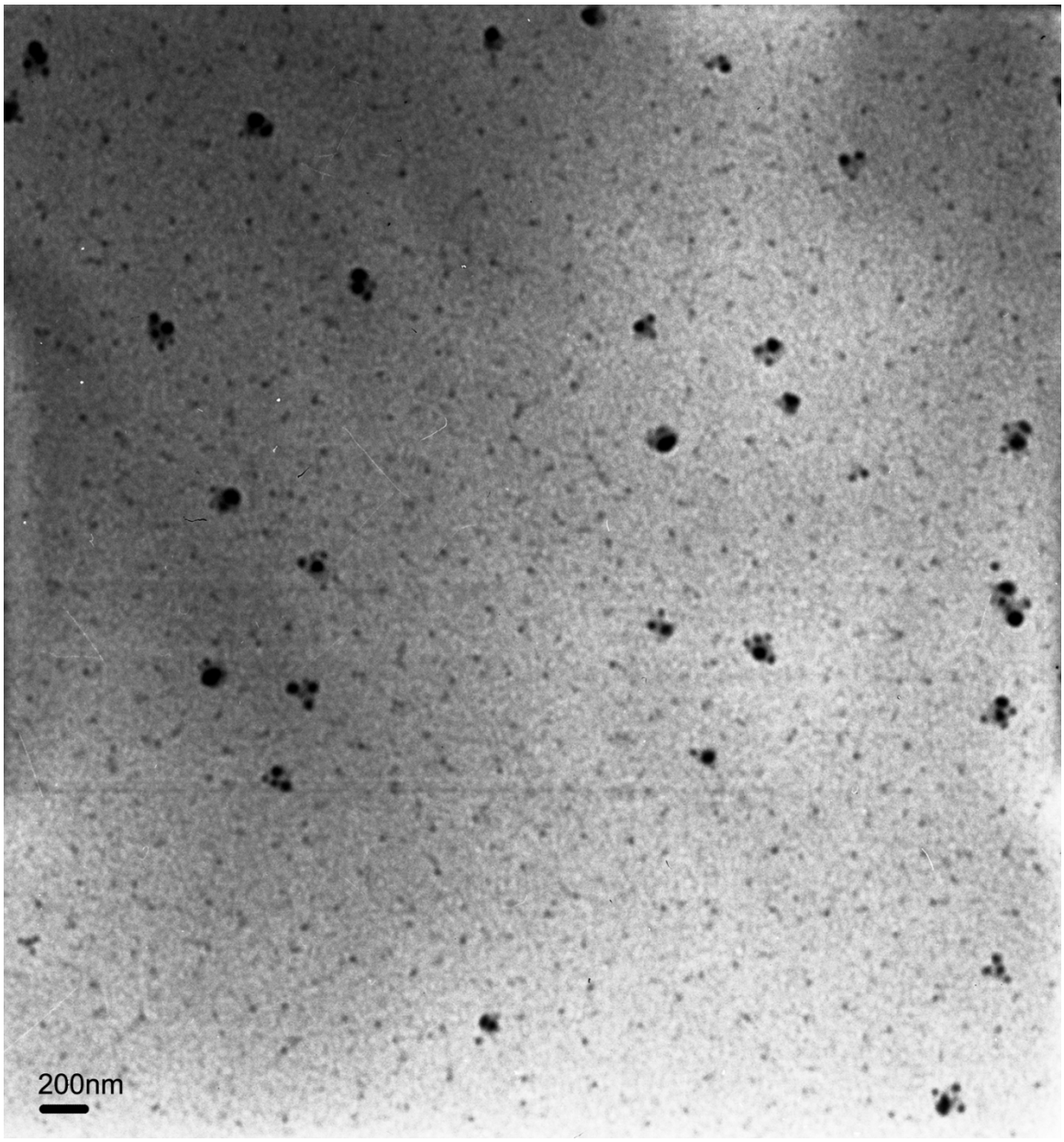

Figure 4.7c Transmission electron micrographs for Ag nanoparticles stabilized by $[WZn_3(H_2O)_2(ZnW_9O_{34})_2]^{12-}$ sandwich polyoxometalate. (20k X)

In contrast, TEM images taken from a drop-coated film of the Ag nanoparticles stabilized by $[WZn_3(H_2O)_2(ZnW_9O_{34})_2]^{12-}$ sandwich polyoxometalate showed different morphology, as shown in Figure 4.7 a, b, and c.

The silver nanoparticles stabilized by $[WZn_3(H_2O)_2(ZnW_9O_{34})_2]^{12-}$ sandwich polyoxometalate can be categorized into two groups depending on their size. Some large nanoparticles with mean diameter ~20nm decorated on the surface of ball shape matrix polyoxometalates with a size of 50~60 nm in diameter. A bigger population of smaller particles (c. a. 8 nm) was dispersed all over the micrograph. Thus, the 420nm plasmon resonance band should be attributed to the ~6nm Ag colloid when stabilized by $PW_{12}O_{40}^{3-}$ Keggin, and the band centered at 450nm can either be assigned to the 20nm Ag nanoparticles, or 60nm Ag-sandwich POM nanocomposite, when stabilized by $[WZn_3(H_2O)_2(ZnW_9O_{34})_2]^{12-}$. By comparing with reported the peak position/size relationship[23], we tended to believe that the 450nm band are due to 60nm Ag-sandwich POM nanocomposite, which implied that two different species, a 60nm Ag-sandwich POM nanocomposite and 5nm Ag nanoparticles, co-existed in the solution. But if that was the case, some other questions would come up; for example, should a peak for the smaller nanoparticles been seen in the UV-vis spectra, and how come a single reducing agent can produce two distinct sizes of silver nanoparticles in the same pot. Further investigations are needed.

4.3.4 Dynamic Light Scattering

Bearing these questions in mind, Dynamic Light Scattering (DLS) was performed to depict the size distribution in solution. In complementary to TEM, which reads the “dried”

particle size, DLS can be used to determine the size of particles in solution. Dynamic Light Scattering works by measuring the scattered light intensity at one fixed angle. Due to Brownian motion, particle positions in the solution are constantly changing. Thus the intensity of light scattered in a particular direction by dispersed particles tends to periodically change with time. Brownian motion for smaller particles is faster than the one for larger particles. The fluctuations in the intensity versus time profile for all particles in solution are recorded by DLS instruments. A correlation function can be derived from the intensity versus time profile. This exponentially decaying correlation function is analyzed for characteristic decay times, which are related to diffusion coefficients for different particles. And then particle size can be obtained from the Stokes-Einstein equation,

$$D = \frac{k_B T}{6\pi\eta r}$$

where D is the particles diffusion coefficient, k_B is the Boltzmann constant, T is the temperature of the solution, η is the viscosity of the solution, and r is the particle radius. A schematic diagram of working principles of dynamic light scattering (DLS) is outlined in Figure 4.8.

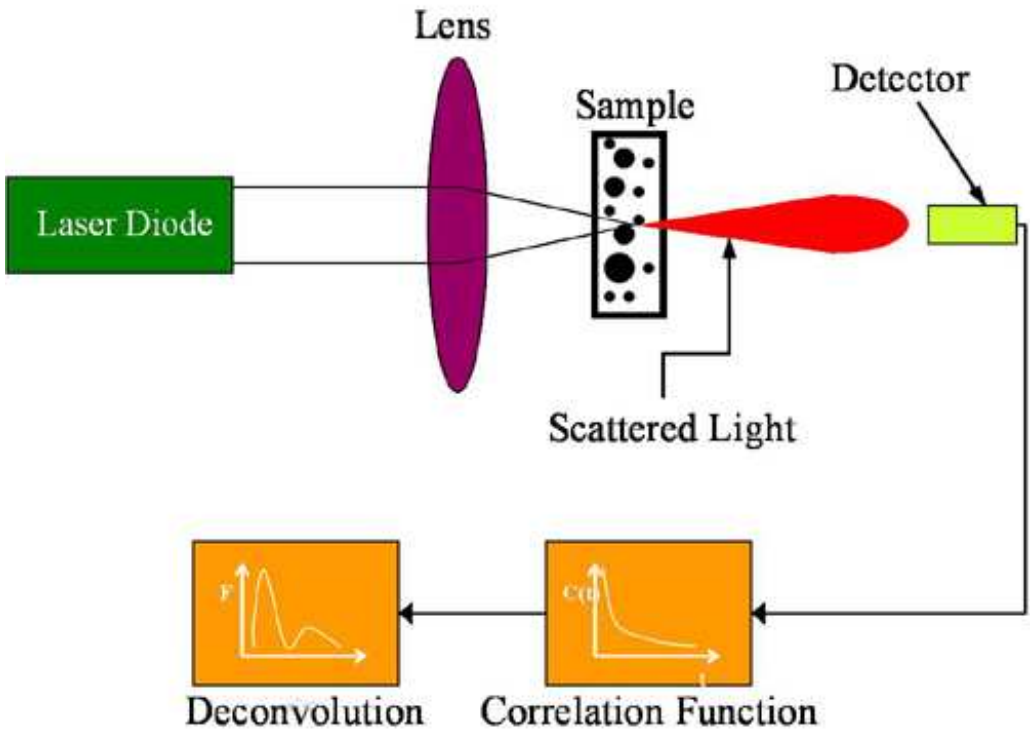

Figure 4.8 Schematic diagram of working principles of dynamic light scattering (DLS)

The Dynamic Light Scattering size distributions are shown in Figure 4.9. The intensity weighting and volume weighting results clearly indicated that there are two groups of nanoparticles in the solution, a group with larger mean diameter of ~60nm, and a group with smaller particles sizing around 7~8nm. The number weighting result only showed a single peak for the smaller particles, that's due to the overwhelming numbers of smaller particles to the numbers of larger nanocomposite. Statistical results of Dynamic Light Scattering size distributions using three different weighting methods are summarized in Table 4.1. The result of Dynamic Light Scattering not only confirmed the co-existence of ~60nm diameter Ag-sandwich

POM nanocomposite and ~5nm Ag nanoparticles, but also automatically answered the question why the peak for the smaller nanoparticles was not observed in the UV-vis spectra. There are two components[23] of the electromagnetic field contributing to the plasmon resonances in silver nanoparticles: a non-radiative absorbing component and a near-field component that evolves into radiative far-field scattering. Usually, for small particles, absorption of light is the predominant part of the plasmon resonances, whereas scattering grows quickly, becoming the major contribution as particle diameter approaches the wavelength of visible light. From the DLS data, the scattered light intensity from the nanocomposites was found almost 50 times larger than the one from nanoparticles. A Mie theory model for 70nm silver nanoball produced a scattering coefficient which is 35 times larger than absortion coefficient. Thus, the contributions from ~5nm Ag nanoparticles were too weak and overlapped by the broad plasmon resonance band of Ag-sandwich POM nanocomposites in the UV-vis result.

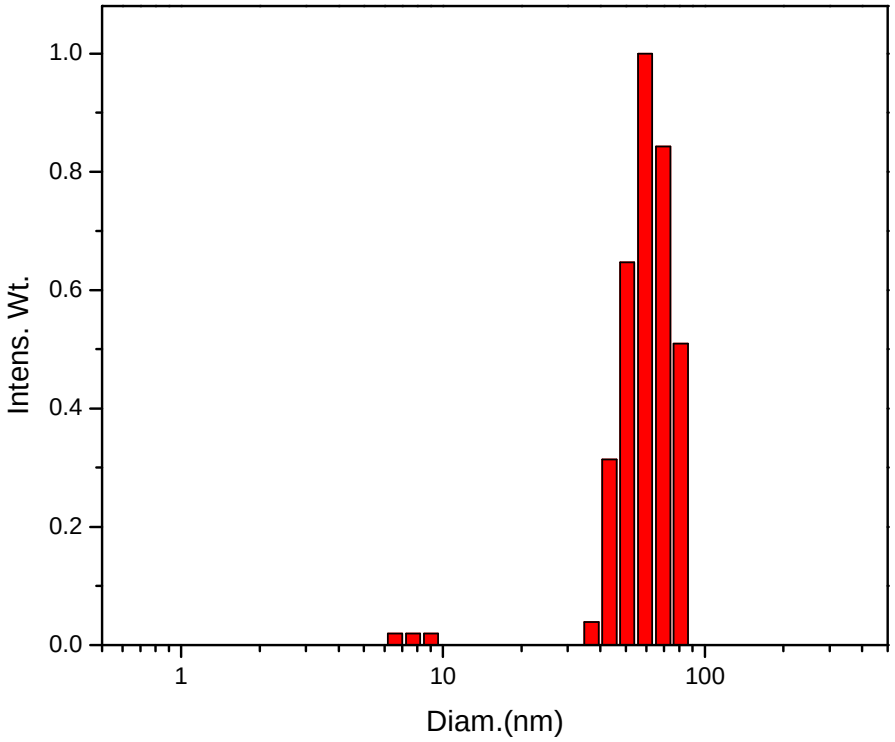

Figure 4.9a Intensity Weighting Dynamic Light Scattering size distribution of $[WZn_3(H_2O)_2(ZnW_9O_{34})_2]^{12-}$stabilizing silver colloid.

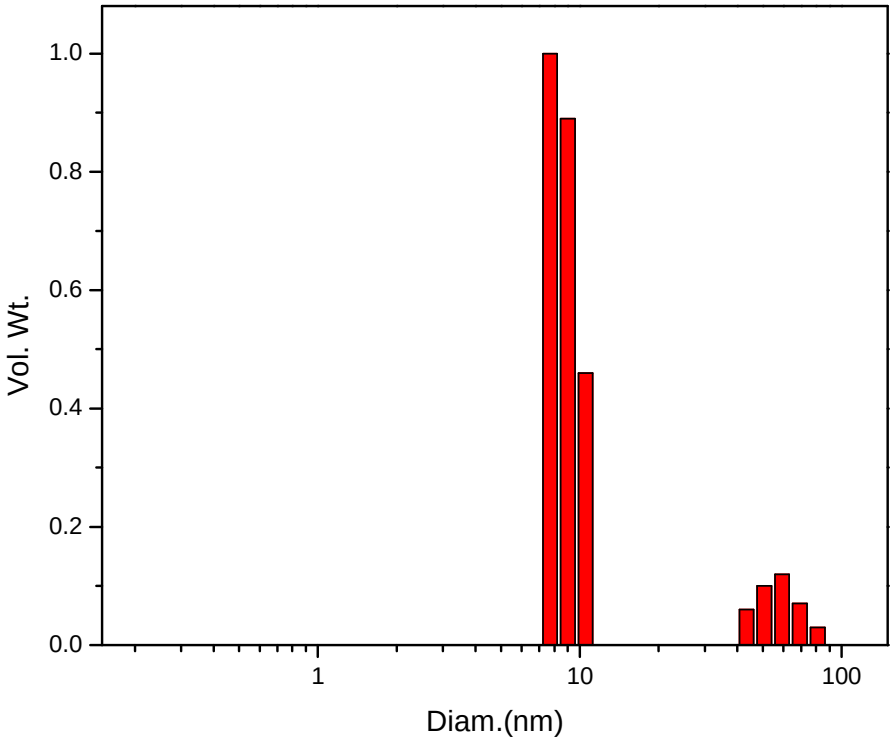

Figure 4.9b Volume Weighting Dynamic Light Scattering size distribution of $[WZn_3(H_2O)_2(ZnW_9O_{34})_2]^{12-}$stabilizing silver colloid.

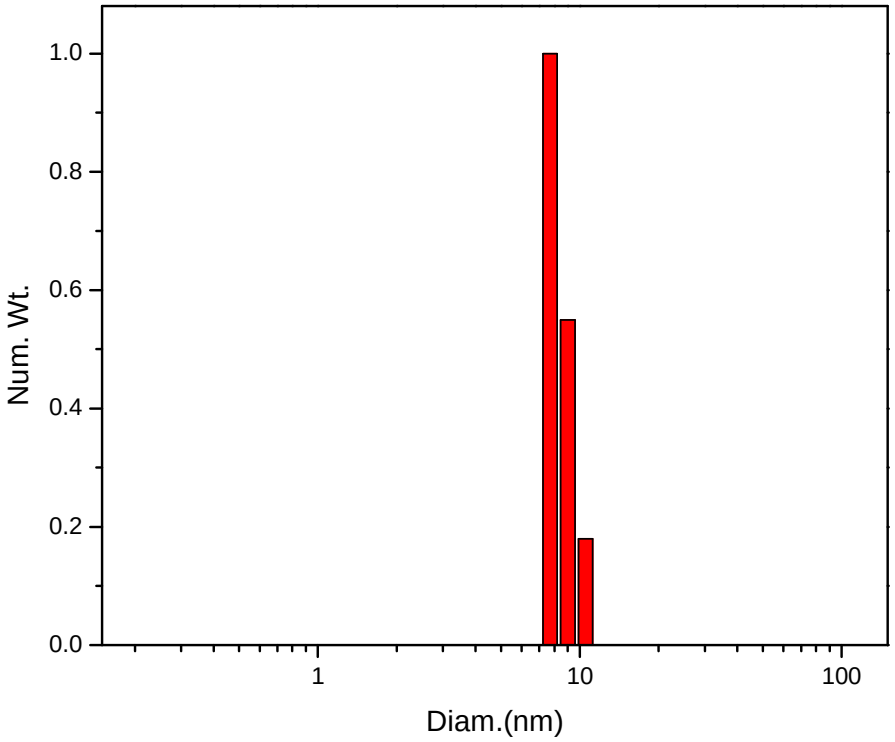

Figure 4.9c Number Weighting Dynamic Light Scattering size distribution of $[WZn_3(H_2O)_2(ZnW_9O_{34})_2]^{12-}$ stabilizing silver colloid.

Table 4.1 Statistical data for Dynamic Light Scattering size distributions using three different weighting methods

	Peak 1		Peak 2	
	size /nm	**%**	**size /nm**	**%**
Volume	7.5±0.8	93.9	53.7±11.2	6.1
Intensity	7.9±1.0	2.2	62.0±11.2	97.8
number	7.2±0.9	100	———	—

The confirmed existence of ~60nm diameter Ag-sandwich POM nanocomposite answered one question, yet another interesting question came up. Is the nanocomposite hollow or filled? Figure 4.10 shows a TEM micrograph of a broken Ag-sandwich polyoxometalate nanocomposite, which indicates the composite is not filled. Polyoxometalates have been reported to self-assemble hollow, vesicle-like, ball-shape structures[24-44], as shown in Figure 4.11. These second order structures are similar to the surfactants and membrane lipids bilayer structure, such as micelles and liposomes due to their amphiphilic character—the fact that part of their structure is attracted to polar environments while another part is attracted to non-polar environments. But the heterpolyanions do not have these bi-polar features. The driving force for the polyoxometalates self-assembly formation is believed to be a delicate balance between short-range attractive forces among polyanions solvent molecules and counter-ion, and repulsive electrostatic interactions between adjacent polyoxometalates. However, the polyoxometalates that can self-assemble into the second order structures by themselves have very large sizes, which are so-called “giant polyoxometalates”. The smallest reported POM[38] can form hollow vesicle structures by themselves is $[Cu_{20}Cl(OH)_{24}(H_2O)_{12}(P_8W_{48}O_{184})]^{25-}$.

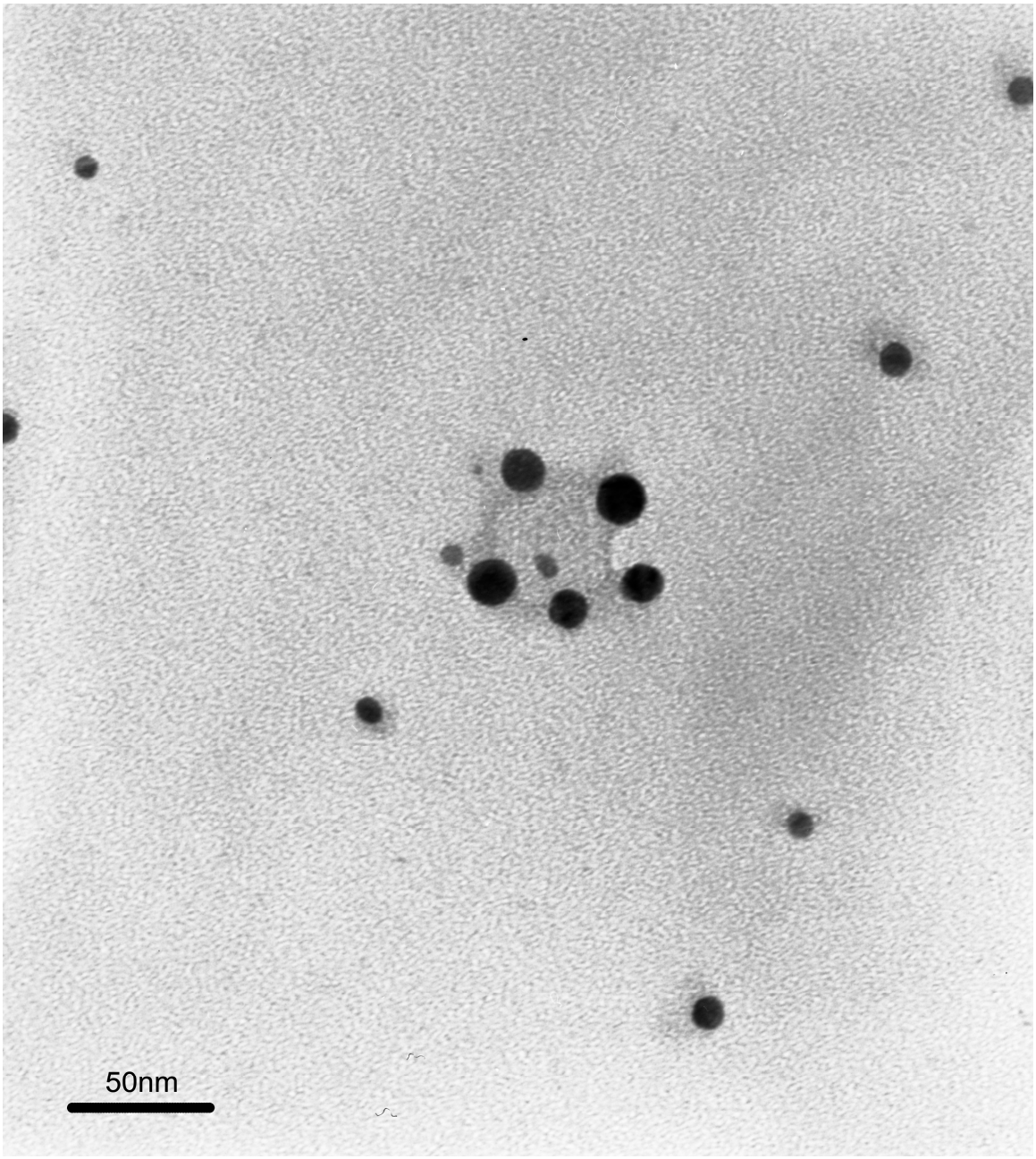

Figure 4.10 Transmission electron micrographs showing a broken hollow Ag-sandwich polyoxometalate nanocomposite.

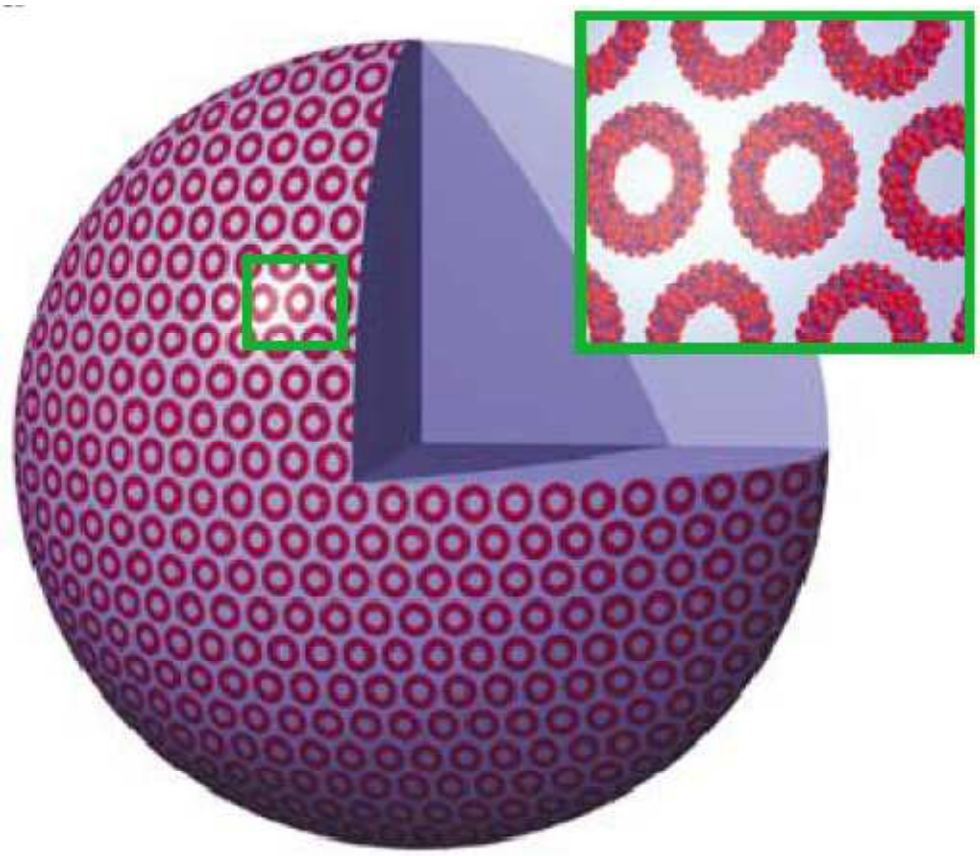

Figure 4.11 Schematic plot of the vesicle structure formed from Mo154 wheel-shape polyoxometalate (90nm in diameter) in aqueous solution, with inset showing enlarged nanowheels. Taken from Ref. 27 with permission.

4.3.5 Blackberry Structure

Smaller polyoxometalates can also form similar large vesicles, either by encapsulation of the polyanions by surfactants[39] to take advantages of their amphiphilic properties, or attaching POM to the surface of metal nanoparticles[45] to obtain nanometer sized object with POM surface. Usually, in the latter case, the size of self-assembled vesicle structure is subject to ratio of metal

ion concentration to polyoxometalate concentration. At lower ratio, the size of nanostructure increases as the ratio increase. When the ratio reaches a certain number, the diameter of self-assembled hollow vesicle becomes stable and further increase of the ratio has little influence on the size. A study of nanocomposite size dependence on the ratio of $[Ag^{+}]$ to $\{[WZn_3(H_2O)_2(ZnW_9O_{34})_2]^{12-}\}$, by Dynamic Light Scattering volume weighting, revealed that our system follow the same trend, as shown in Figure 4.12. Thus, the Ag-sandwich polyoxometalate nanocomposite is hollow ball-shape.

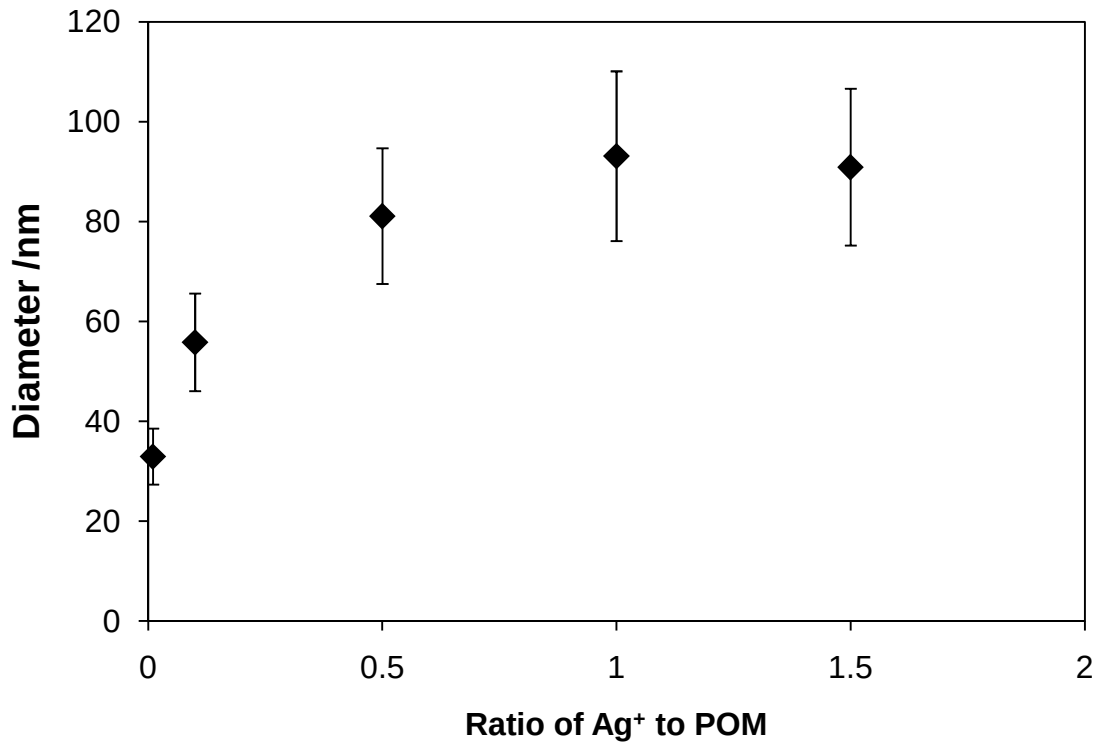

Figure 4.12 Volume weighting diameter at different molar ratios of Ratio of Ag^{+} to POM

The last mystery unsolved is why the Ag nanoparticles on the polyoxometalate vesicle surface (`20nm) are larger than those dispersed among vesicles. It has been reported that small Ag nanoparticles can fuse into larger ones via Ostwald ripening process[46-52], due to the energetic driven forces. Usually, Ostwald ripening occurs only at elevated temperatures, at least > 100 $^{\circ}$C. However, on the surface of a conductive substrate such as ITO or graphite, the reformation can happen with presence of water, which is so-called electrochemical Ostwald ripening[47]. Polyoxometalate molecules have been considered as electron-mediators at the molecular level for a long time. Some POMs have been used as conductivity promoter[53-56] in polyelectrolyte fuel cell membrane. Thus, we believe that electrochemical Ostwald ripening occurred in our system. One evidence is that the large silver nanoparticles are only found on the outer surface of the POM assembly, where there are plenty of water supplies. A formation mechanism is proposed, as shown in Figure 4.13.

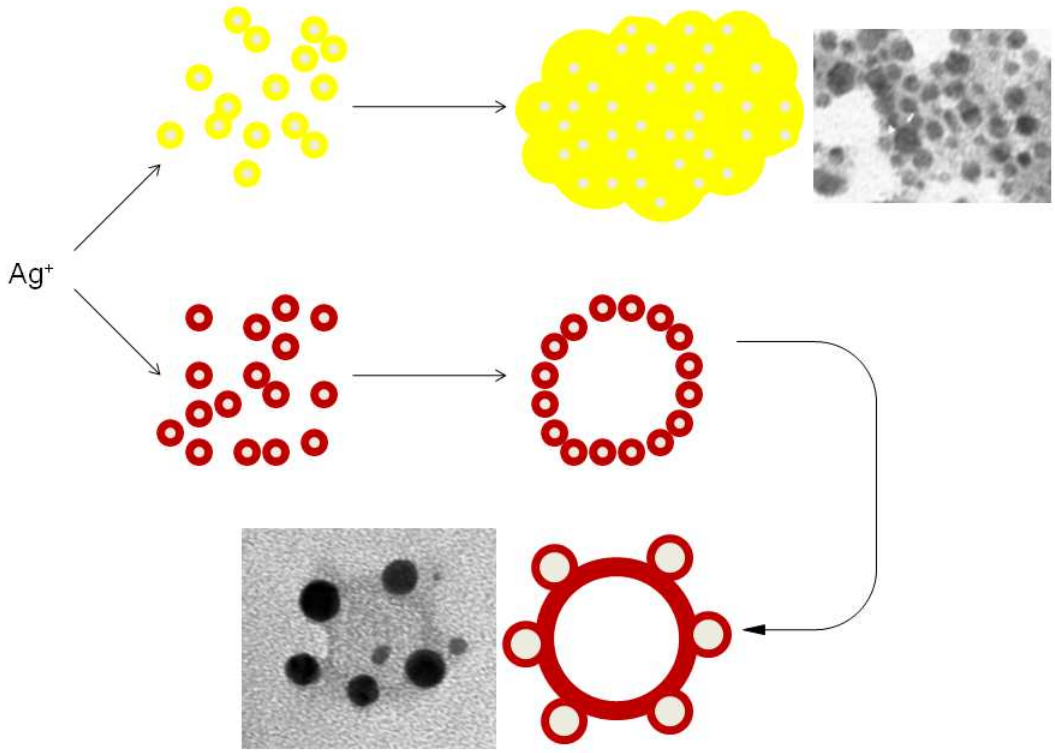

Figure 4.13 Proposed mechanism for photogeneration of Ag nanoparticles using polyoxometalate as reductant and stabilizer. (a) $PW_{12}O_{40}^{3-}$; (b) $[WZn_3(H_2O)_2(ZnW_9O_{34})_2]^{12-}$

4.4 Conclusions

Sandwich type polyoxometalates $Na_{12}[WZn_3(H_2O)_2(ZnW_9O_{34})_2]$ were synthesized. The as-synthesized sandwich POM and a Keggin type polyoxometalate $Na_3PW_{12}O_{40}$ were used as both reducing agent and stabilizing agent for silver nanoparticles. Both photoreduction and chemical reduction routes produced Ag nanoparticles with very similar size distribution. However, the plasmon resonance band position suggested that the particles produced by

sandwich POM is larger than the ones produced by Keggin, which is contradict to either “soluble electrode” electrochemical reduction or stabilizing strength theory. Transmission electron microscopy and Dynamic Light Scattering investigation showed that a large hollow ball-shape nanocomposite is formed in the sandwich polyoxometalate case. The size of the nanocomposite increased as the ratio of [Ag^{+}] to [POM] increased, and reached a plateau region when the ratio was greater than 1. The small silver nanoparticles are fused into larger ones via electrochemical Ostwald ripening on the outer surface of nanocomposite.

References

(1) Faraday, M., The Bakerian Lecture: Experimental Relations of Gold (and Other Metals) to Light; *Phil. Trans. R. Soc. Lond.* **1857**, 147, 145-181.

(2) Nie, S.; Emory, S. R., Probing single molecules and single nanoparticles by surface-enhanced Raman scattering; *Science* **1997**, 275, (5303), 1102-1105.

(3) Frattinia, A.; Pellegrib, N.; Nicastrob, D.; Sanctisb, O. d., Effect of amine groups in the synthesis of Ag nanoparticles using aminosilanes; *Materials Chemistry and Physics* **2005**, 94, (1), 148-152.

(4) Kishore, P. S.; Viswanathan, B.; Varadarajan, T. K., Synthesis and Characterization of Metal Nanoparticle Embedded Conducting Polymer–Polyoxometalate Composites; *Nanoscale Res Lett* **2008**, 3, (1), 14-20.

(5) Troupis, A.; Hiskia, A.; Papaconstantinou, E., Synthesis of Metal Nanoparticles by Using Polyoxometalates as Photocatalysts and Stabilizers; *Angew. Chem. Int. Ed.* **2002**, 41, (11), 1911-1914.

(6) Costa-Coquelarda, C.; Schaminga, D.; Lampre, I.; Ruhlmann, L., Photocatalytic reduction of Ag_2SO_4 by the Dawson anion α-$[P_2W_{18}O_{62}]^{6-}$ and tetracobalt sandwich complexes *Applied Catalysis B: Environmental* **2008**, 84, (3-4), 835-842

(7) Gordeev, A. V.; Kartashev, N. I.; Ershov, B. G., Metal Nanoparticles with $PW_{11}O_{39}^{7-}$ and $P_2W_{17}O_{61}^{10-}$ Heteropoly Anions as Stabilizing Agents: Radiation-Chemical Preparation and Properties; *High Energy Chemistry* **2002**, 36, (2), 102-106.

(8) Dolbecq, A.; Compain, J.-D.; Mialane, P.; Marrot, J.; Secheresse, F.; Keita, B.; Holzle, L. R. B.; Miserque, F.; Nadjo, L., Hexa- and Dodecanuclear Polyoxomolybdate Cyclic Compounds: Application toward the Facile Synthesis of Nanoparticles and Film Electrodeposition; *Chem.--Eur. J.* **2009**, 15, (3), 733-741.

(9) Keita, B.; Zhang, G.; Dolbecq, A.; Mialane, P.; Secheresse, F.; Miserque, F.; Nadjo, L., Mo^{V}-Mo^{VI} Mixed Valence Polyoxometalates for Facile Synthesis of Stabilized Metal Nanoparticles : Electrocatalytic Oxidation of Alcohols.; *J. Phys. Chem. C* **2007**, 111, (23), 8145-8148.

(10) Kulesza, P. J.; Karnicka, K.; Chojak, M.; Miecznikowski, K.; Skunik, M.; Baranowska, B.; Kolary, A.; Adamczyk, L., Electrocatalytic network film of polyaniline linked phosphomolybdate covered platinum nanoparticles.; *Proceedings - Electrochemical Society* **2005**, 2004, (18), 165-174.

(11) Keita, B.; Mbomekalle, I.-M.; Nadjo, L.; Haut, C., Tuning the formal potentials of new VIV-substituted Dawson-type polyoxometalates for facile synthesis of metal nanoparticles; *Electrochem. Commun.* **2004**, 6, (10), 978-983.

(12) Izumi, Y.; Konishi, K.; Tsukahara, M.; Obaid, D. M.; Aika, K.-i., Selective Butanol Synthesis over Rhodium-Molybdenum Catalysts Supported in Ordered Mesoporous Silica; *J. Phys. Chem. C* **2007**, 111, (27), 10073-10081.

(13) Ott, L. S.; Finke, R. G., Supersensitivity of transition- metal nanoparticle formation to initial precursor concentration and reaction temperature: understanding its origins. ; *J. Nanosci. Nanotechnol.* **2008**, 8, (3), 1551-1556.

(14) Ernst, A. Z.; Sun, L.; Wiaderek, K.; Kolary, A.; Zoladek, S.; Kulesza, P. J.; Cox, J. A., Synthesis of Polyoxometalate-Protected Gold Nanoparticles by a Ligand-Exchange Method: Application to the Electrocatalytic Reduction of Bromate; *Electroanalysis* **2007**, 19, (19-20), 2103-2109.

(15) Kulesza, P. J.; Marassi, R.; Karnicka, K.; Wlodarczyk, R.; Miecznikowski, K.; Chojak, M.; Kolary, A., New strategies to activation and assembling catalytic metal nanoparticles through modification with polyoxometallate monolayers.; *ECS Transactions* **2006**, 1, (6), 107-118.

(16) Sharma, V. K.; Yngard, R. A.; Lin, Y., Silver nanoparticles: Green synthesis and their antimicrobial activities; *Advances in Colloid and Interface Science* **2009**, 145, (1), 83-96.

(17) Tourné, C. M.; Tourné, G. F.; Zonnevijlle, F., Chiral polytungstometalates $[WM_3(H_2O)_2(XW_9O_{34})_2]^{12-}$ (X = M = Zn or Co^{II}) and their M-substituted derivatives. Syntheses, chemical, structural and spectroscopic study of some D,L sodium and potassium salts; *J. Chem. Soc., Dalton Trans.* **1991**, (1), 143-155.

(18) Nomiya, K.; Miwa, M., Tetrahedral metal complexes of $MW_{12}O_{40}$ - type ($M=Al^{III}$, Zn^{II}) with dodecatungstate as tetrahedral ligand; *Polyhedron* **1983**, 2, (9), 955-958.

(19) Troupis, A.; Gkika, E.; Hiskia, A.; Papaconstantinou, E., Photocatalytic reduction of metals using polyoxometallates: recovery of metals or synthesis of metal nanoparticles; *Comptes Rendus Chimie* **2006**, 9, (5-6), 851-857.

(20) Troupis, A.; Triantis, T.; Hiskia, A.; Papaconstantinou, E., Rate-Redox-Controlled Size-Selective Synthesis of Silver Nanoparticles Using Polyoxometalates; *Eur. J. Inorg. Chem.* **2008**, 2008, (36), 5579 - 5586.

(21) Weinstock, I. A., Homogeneous-Phase Electron-Transfer Reactions of Polyoxometalates; *Chem. Rev.*, **1998**, 98, (1), 113-170.

(22) Maayan, G.; Neumann, R., Direct aerobic epoxidation of alkenes catalyzed by metal nanoparticles stabilized by the $H_5PV_2Mo_{10}O_{40}$ polyoxometalate; *Chem. Commun.* **2005**, 2005, (36), 4595 - 4597.

(23) David D. Evanoff, J.; Chumanov, G., Size-Controlled Synthesis of Nanoparticles. 2. Measurement of Extinction, Scattering, and Absorption Cross Sections; *J. Phys. Chem. B* **2004**, 108, (37), 13957-13962.

(24) Müller, A.; Diemann, E.; Kuhlmann, C.; Eimer, W.; Serain, C.; Tak, T.; Knöchel, A.; Pranzas, P. K., Hierarchic patterning: architectures beyond ‘giant molecular wheels’; *Chem. Commun.* **2001**, 1928-1929.

(25) Liu, T., Supramolecular Structures of Polyoxomolybdate-Based Giant Molecules in Aqueous Solution; *J. Am. Chem. Soc.* **2002**, 124, (37), 10942-10943.

(26) Liu, T., An Unusually Slow Self-Assembly of Inorganic Ions in Dilute Aqueous Solution; *J. Am. Chem. Soc.* **2003**, 125, (2), 312-313.

(27) Liu, T.; Diemann, E.; Li, H.; Dress, A. W. M.; Müller, A., Self-assembly in aqueous solution of wheel-shaped Mo_{154} oxide clusters into vesicles; *Nature* **2003**, 426, (6), 59-62.

(28) Mishra, P. P.; Pigga, J.; Liu, T. B., Membranes based on "Keplerate"-type polyoxometalates: Slow, passive cation transportation and creation of water microenvironment; *J. Am. Chem. Soc.* **2008**, 130, (5), 1548.

(29) Tang, P. Q.; Ha, X. F.; Fan, D. W.; Wang, L. L.; Hao, J. C., Surface charges of hedgehog-shaped polyoxomolybdate modified by a cationic surfactant and the inorganic/organic complex; *Colloids and Surfaces a-Physicochemical and Engineering Aspects* **2008**, 312, (1), 18-23.

(30) Kistler, M. L.; Bhatt, A.; Liu, G.; Casa, D.; Liu, T. B., A complete macroion-"blackberry" assembly-macroion transition with continuously adjustable assembly sizes in {Mo-132} water/acetone systems; *J. Am. Chem. Soc.* **2007**, 129, (20), 6453-6460.

(31) Verhoeff, A. A.; Kistler, M. L.; Bhatt, A.; Pigga, J.; Groenewold, J.; Klokkenburg, M.; Veen, S.; Roy, S.; Liu, T. B.; Kegel, W. K., Charge regulation as a stabilization mechanism for shell-like assemblies of polyoxometalates; *Physical Review Letters* **2007**, 99, (6).

(32) Li, H. L.; Sun, H.; Qi, W.; Xu, M.; Wu, L. X., Onionlike hybrid assemblies based on surfactant-encapsulated polyoxometalates; *Angewandte Chemie-International Edition* **2007**, 46, (8), 1300-1303.

(33) Liu, T. B.; Diemann, E.; Muller, A., Hydrophilic inorganic macro-ions in solution: Unprecedented self-assembly emerging from historical "blue waters"; *Journal of Chemical Education* **2007**, 84, (3), 526-532.

(34) Long, D. L.; Burkholder, E.; Cronin, L., Polyoxometalate clusters, nanostructures and materials: From self assembly to designer materials and devices; *Chemical Society Reviews* **2007**, 36, (1), 105-121.

(35) Oleinikova, A.; Weingartner, H.; Chaplin, M.; Diemann, E.; Bogge, H.; Muller, A., Self-association based on interfacial structured water leads to {Mo-154}approximate to (1165) super clusters: A dielectric study; *ChemPhysChem* **2007**, 8, (5), 646-649.

(36) Liu, T. B.; Imber, B.; Diemann, E.; Liu, G.; Cokleski, K.; Li, H. L.; Chen, Z. Q.; Muller, A., Deprotonations and charges of well-defined $\{Mo_{72}Fe_{30}\}$ nanoacids simply stepwise tuned by pH allow control/variation of related self-assembly processes; *J. Am. Chem. Soc.* **2006**, 128, (49), 15914-15920.

(37) Liu, G.; Kistler, M. L.; Li, T.; Bhatt, A.; Liu, T. B., Counter-ion association effect in dilute giant polyoxometalate $[(As^{III}_{12}Ce)Ce^{III}_{16}(H_2O)_{36}W_{148}O_{524}]^{76-}$ ({W148}) and $[Mo_{132}O_{372}(CH_3COO)_{30}(H_2O)_{72}]^{42-}$ ({Mo-132}) macroanionic solutions; *Journal of Cluster Science* **2006**, 17, (2), 427-443.

(38) Liu, G.; Liu, T. B.; Mal, S. S.; Kortz, U., Wheel-shaped polyoxotungstate $[Cu_{20}Cl(OH)_{24}(H_2O)_{12}(P_8W_{48}O_{184})]^{25-}$ macroanions form supramolecular "blackberry" structure in aqueous solution; *J. Am. Chem. Soc.* **2006**, 128, (31), 10103-10110.

(39) Bu, W. F.; Li, H. L.; Sun, H.; Yin, S. Y.; Wu, L. X., Polyxometalate-based vesicle and its honeycomb architectures on solid surfaces; *J. Am. Chem. Soc.* **2005**, 127, (22), 8016-8017.

(40) Liu, G.; Cons, M.; Liu, T. B., The ionic effect on supramolecular associations in polyoxomolybdate solution; *Journal of Molecular Liquids* **2005**, 118, (1-3), 27-29.

(41) Liu, G.; Liu, T. B., Strong attraction among the fully hydrophilic $\{Mo_{72}Fe_{30}\}$ macroanions; *J. Am. Chem. Soc.* **2005**, 127, (19), 6942-6943.

(42) Liu, G.; Liu, T. B., Thermodynamic properties of the unique self-assembly of $\{Mo_{72}Fe_{30}\}$ inorganic macro-ions in salt-free and salt-containing aqueous solutions; *Langmuir* **2005**, 21, (7), 2713-2720.

(43) Kogerler, P.; Cronin, L., Polyoxometalate nanostructures, superclusters, and colloids: From functional clusters to chemical aesthetics; *Angewandte Chemie-International Edition* **2005**, 44, (6), 844-846.

(44) Liu, G.; Cai, Y. G.; Liu, T. B., Automatic and subsequent dissolution and precipitation process in inorganic macroionic solutions; *J. Am. Chem. Soc.* **2004**, 126, (51), 16690-16691.

(45) Zhang, J.; Keita, B.; Nadjo, L.; Mbomekalle, I. M.; Liu, T., Self-Assembly of Polyoxometalate Macroanion-Capped Pd^0 Nanoparticles in Aqueous Solution; *Langmuir* **2008**, 24, (10), 5277-5283.

(46) Chen, M.; Feng, Y.-G.; Wang, X.; Li, T.-C.; Zhang, J.-Y.; Qian, D.-J., Silver nanoparticles capped by oleylamine: Formation, growth, and self-organization; *Langmuir* **2007**, 23, (10), 5296-5304.

(47) Redmond, P. L.; Hallock, A. J.; Brus, L. E., Electrochemical Ostwald Ripening of Colloidal Ag Particles on Conductive Substrates; *Nano Lett.* **2005**, 5, (1), 131-135.

(48) Sun, J.; Ma, D.; Zhang, H.; Liu, X.; Han, X.; Bao, X.; Weinberg, G.; Pfander, N.; Su, D., Toward monodispersed silver nanoparticles with unusual thermal stability; *J Am Chem Soc* **2006**, 128, (49), 15756-15764.

(49) Sun, Y.; Mayers, B.; Herricks, T.; Xia, Y., Polyol Synthesis of Uniform Silver Nanowires: A Plausible Growth Mechanism and the Supporting Evidence; *Nano Lett.* **2003**, 3, (7), 955-960.

(50) Van Hoonacker, A.; Englebienne, P., Revisiting silver nanoparticle chemical synthesis and stability by optical spectroscopy; *Curr. Nanosci.* **2006**, 2, (4), 359-371.

(51) Wang, X.; Somsen, C.; Grundmeier, G., Aging of thin Ag/fluorocarbon plasma polymer nanocomposite films exposed to water-based electrolytes; *Acta Mater.* **2008**, 56, (4), 762-773.

(52) Zhu, L.; Lu, G.; Mao, S.; Chen, J.; Dikin, D. A.; Chen, X.; Ruoff, R. S., Ripening of silver nanoparticles on carbon nanotubes; *Nano* **2007**, 2, (3), 149-156.

(53) Choi, J. K.; Lee, D. K.; Kim, Y. W.; Min, B. R.; Kim, J. H., Composite polymer electrolyte membranes comprising triblock copolymer and heteropolyacid for fuel cell applications; *J. Polym. Sci., Part B: Polym. Phys.* **2008**, 46, (7), 691-701.

(54) Coronado, E.; Delhaes, P.; Galan-Mascaros, J. R.; Gimenez-Saiz, C.; Gomez-Garcia, C. J., Hybrid molecular materials having conducting and magnetic networks: charge transfer salts based on organic pi-donor molecules and inorganic magnetic clusters; *Synth. Met.* **1997**, 85, (1-3), 1647-1650.

(55) Gomez-Garcia, C. J.; Gimenez-Saiz, C.; Triki, S.; Coronado, E.; Le Magueres, P.; Ouahab, L.; Ducasse, L.; Sourisseau, C.; Delhaes, P., Coexistence of Magnetic and Delocalized Electrons in Hybrid Molecular Materials. The Series of Organic-Inorganic Radical Salts (BEDT-TTF)$_8$[$XW_{12}O_{40}$](solv)$_n$ (X = 2(H^+), B^{III}, Si^{IV}, Cu^{II}, Co^{II}, and Fe^{III}; solv = H_2O, CH_3CN); *Inorg. Chem.* **1995**, 34, (16), 4139-4151.

(56) Gomez-Romero, P.; Cuentas-Gallegos, K.; Lira-Cantu, M.; Casan-Pastor, N., Hybrid nanocomposite materials for energy storage and conversion applications; *J. Mater. Sci.* **2005**, 40, (6), 1423-1428.

Chapter 5.

Aqueous Mixed-Valence Di-Copper Complex Intermediate in Copper Catalyzed Degradation of Giant Polyoxomolybdate

5.1 Introduction

5.1.1 Mixed-valence di-copper complex

Copper-containing enzymes play an essential role in oxygen processing of living cells. Some enzymes are found to have fully delocalized mixed-valence di-copper center as active sites to process dioxygen activation. For example, the cellular respiratory enzyme cytochrome c oxidase couples the reduction of dioxygen to water with the production of a proton gradient across the cell membrane. Several representative di-copper enzymes are summerized in table 5.1.

Mixed-valence complexes with rapid electron exchange between the two copper nuclei are great inorganic candidates to model the redox behavior of these biological enzymes. Mixed-Valence Copper acetate $(CH_3COO)_2Cu^{I}$-$Cu^{II}(OOCCH_3)_2$, as shown in Figure 5.1, has been reported to be delocalized and to show some unusual absorption spectra only observed with di-copper enzymes[1]. However, due to the Cu(I) disproportionating reaction in water, the mixed-valence compound $(CH_3COO)_2Cu^{I}$-$Cu^{II}(OOCCH_3)_2$ is prepared in methanol[1-3], which is quite different from physiological conditions.

Table 5.1 Enzymes with di-copper active site

enzyme	function
cytochrome c oxidase	Reduction of O_2 to water and production of H^+ gradient across the cell membrane.
Nitrous oxide reductase	Reduction of N_2O to N_2 and water.
Tyrosinases	ortho-hydroxylation of phenols to catechols
Dopamine β-hydroxylase*	Conversion of dopamine to norepinephrine

*Dopamine β-hydroxylase has two di-copper units

One possible reason for those mixed-valence Copper cores stable in the enzymes is that there is less water inside. To obtain a better understanding of how the di-metal center works as active sites under the physiological conditions, some new inorganic compounds are needed. The new protein mimicking compounds need to meet the following conditions:

1. They should be stable in water.

2. They should have copper binding sites such as acetate.

3. They should be large enough to encapsulate Copper cores inside and provide them a mild aqueous environment.

4. They should have ion-channels for ion transportation.

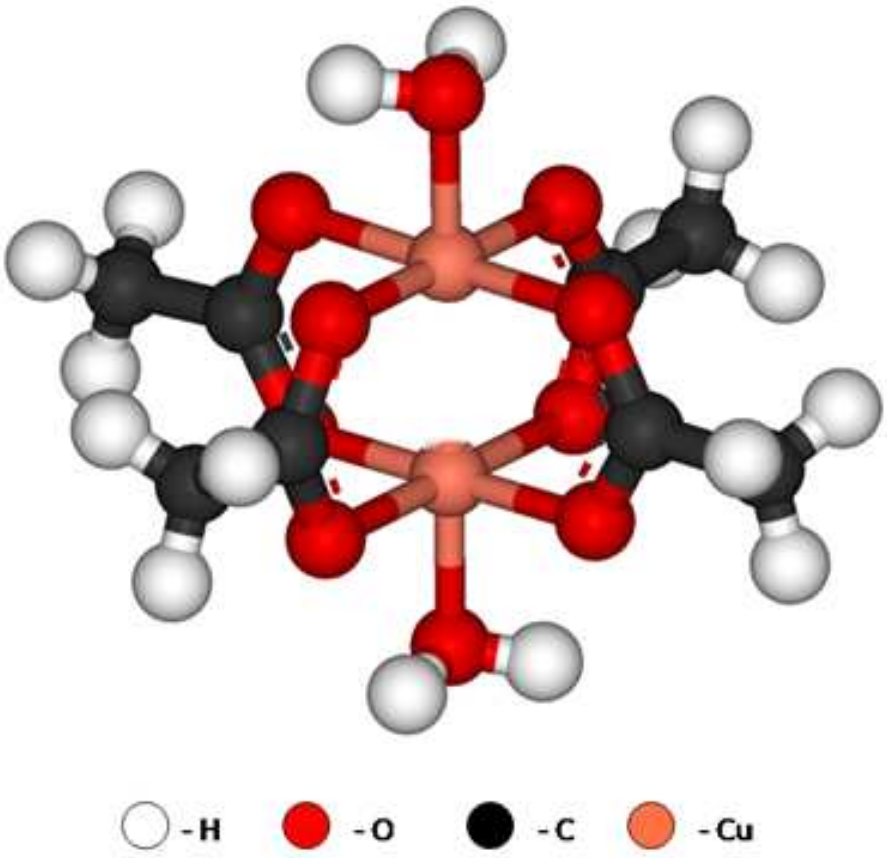

Figure 5.1 Structure of Mixed-Valence Copper acetate $(CH_3COO)_2Cu^{I}$-$Cu^{II}(OOCCH_3)_2$

5.1.2 Mo_{132} Keplerate type nano-capsule as model system.

$[Mo_{132}O_{372}(CH_3COO)_{30}(H_2O)_{72}]^{42-}$ is an ideal model compound in terms of above criteria. Its structure[4] contains mixed valence molybdenum species, as shown in Figure 5.2. It is solvable

and stable in water. It has 30 CH_3COO^- sites that Cu ion can bind to. These 30 CH_3COO^- sites are all attached to the $\{Mo^{V}_{2}\}$ groups and located in the inner side of Keplerate.

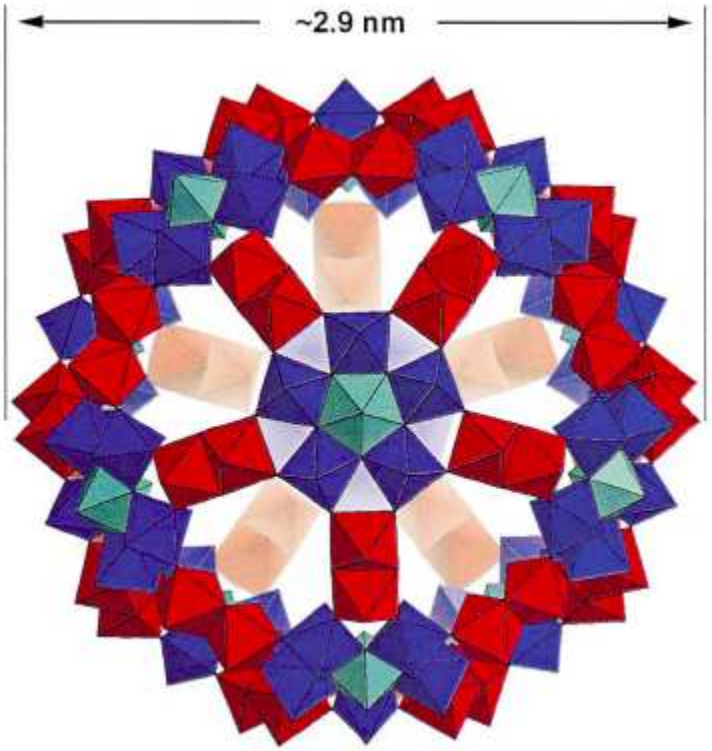

Figure 5.2 Structure of giant polyoxomolybdate $[\{(Mo^{VI})Mo^{VI}_{5}O_{21}(H_2O)_6\}_{12}\{Mo^{V}_{2}O_4(CH_3COO)\}_{30}]^{42-}$. $\{(Mo^{VI})Mo^{VI}_{5}\}$ groups (blue, with the pentagonal $Mo^{VI}O_7$ bipyramids in bright blue). $\{Mo^{V}_{2}\}$ groups, red. Taken from ref 4 with permission.

The diameter of the $[Mo_{132}O_{372}(CH_3COO)_{30}(H_2O)_{72}]^{42-}$ Keplerate is about 2.9 nm, which may accommodate more 100 Cu^{2+} ions. The ion-channels in the Keplerate have been proved to transport ions[5], such as Li^+, Na^+, Ca^{2+} and K^+. It should be noted that the latter two are larger than Cu^{2+} in size. The ion transportation by ion channels in Mo_{132} Keplerate is shown in Figure 5.3.

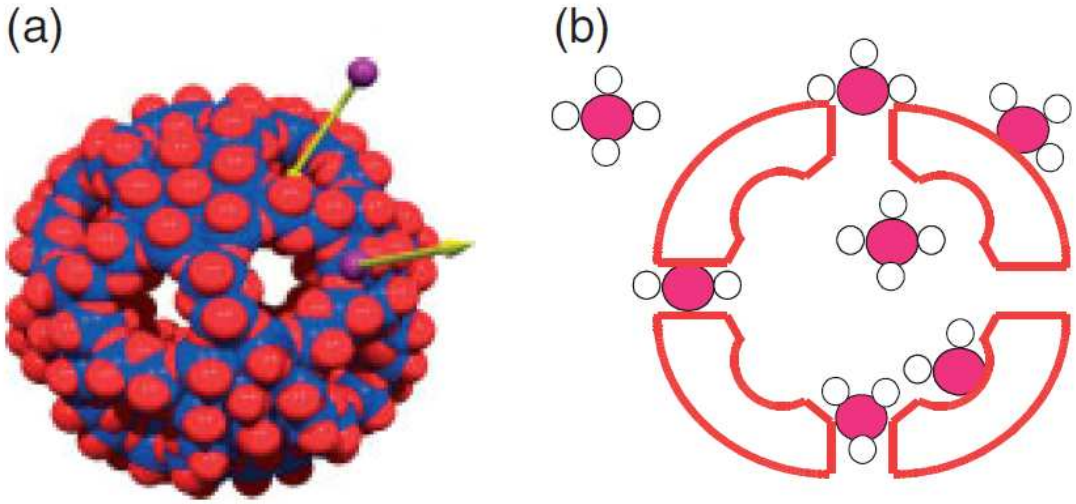

Figure 5.3 Illustration of the ion uptake and release by the Mo_{132}. (b) Cross-section view of the capsule, (full red circles: ions; open circles: solvent molecules). Taken from ref 5 with permission.

Thus, we planned to see the interaction of acetate and Cu^{2+} inside the Keplerate and hope to be able to generate mixed valence copper complexes which can mimic the biological enzymes. However, the original plan is not successful. It turned out that Cu^{2+} can destroy the

$[Mo_{132}O_{372}(CH_3COO)_{30}(H_2O)_{72}]^{42-}$ by acting as catalysts in the degradation of the Keplerate. So the research switched to investigate catalytic degradation of Mo_{132} Keplerate type polyoxometalate by Cu^{2+} ions. Some preliminary were discussed in this chapter.

5.2 Experimental

5.2.1 Materials and reagents

$CuSO_4 \cdot 5H_2O$ (≥98.0%, Sigma-Aldrich), $N_2H_4 \cdot H_2SO_4$ (≥99.0%, Sigma-Aldrich), $(NH_4)_6Mo_7O_{24} \cdot 4H_2O$ (99.98%, Sigma-Aldrich), CH_3COONH_4 (≥97.0%, Fisher Chemical), Acetic Acid, Glacial (≥99.7%, Fisher Chemical), ethanol (89-91%, Fisher Chemical), and diethyl-ether (≥99.0%, Fisher Chemical) was used as received with further purification. Millipore-Q purified distilled water (18MΩ/cm) was used to make up all solutions.

5.2.2 Synthesis of $(NH_4)_{42}[Mo_{132}O_{372}(CH_3COO)_{30}(H_2O)_{72}] \cdot \sim 300H_2O$

$(NH_4)_{42}[Mo_{132}O_{372}(CH_3COO)_{30}(H_2O)_{72}]$ was synthesized according to reference 4. $N_2H_4 \cdot H_2SO_4$ (0.8 g, 6.1 mmol) was added to a solution of $(NH_4)_6Mo_7O_{24} \cdot 4H_2O$ (5.6 g, 4.5 mmol) and CH_3COONH_4 (12.5 g, 162.2 mmol) in H_2O (250 mL). The solution was then stirred until the solution color changed to bluegreen. And then 50% CH_3COOH (83 mL) was subsequently added. The reaction solution, now green, was stored in an open 500-mL Erlenmeyer flask at 20^oC without further stirring. The solution color slowly changed to dark brown. After 4 days the precipitated red brown crystals were filtered off over a glass frit, washed with ethanol, ethanol, and, and dried in air. The crystals were collected in a glass vial for future use.

5.2.3 Characterization

UV-visible spectra were recorded on an Agilent 8453 UV-Visible Spectrophotometer with Agilent UV-Visible ChemStation software. FT-IR analysis was done on loaded transparent KBr pellets on a Shimadzu spectrometer. Raman spectroscopy was performed using the 785 nm (300 mW) line from a wavelength-stabilized high power laser diode system (model SDL-8530, SDL Inc.) or the 514 nm line (20 mW) from an air-cooled ion laser (model 163-C42, Spectra-Physics Lasers, Inc.) as the excitation source. Raman spectra were collected and analyzed using a Renishaw inVia Raman microscope system.

5.3 Results and discussion

5.3.1 Structural Characterization of $(NH_4)_{42}[Mo_{132}O_{372}(CH_3COO)_{30}(H_2O)_{72}] \cdot \sim 300H_2O$

Infrared spectroscopy was employed to determine the structural integrity of the synthesized polyoxometalate. The FT-IR characteristics of the as-synthesized crystal, $(NH_4)_{42}[Mo_{132}O_{372}(CH_3COO)_{30}(H_2O)_{72}] \cdot \sim 300H_2O$ in a typical KBr pellet is shown in Figure 5.4.

The FT-IR spectrum of the as-synthesized $(NH_4)_{42}[Mo_{132}O_{372}(CH_3COO)_{30}(H_2O)_{72}] \cdot \sim 300H_2O$ Keplerate polyoxometalate matched the published literature[4] well. The bands, δ(H-O-H) at 1616 cm^{-1}, υ_{as}(COO) at 1541 cm^{-1}, δ(CH_3) at 1442 cm^{-1} (shoulder peak), υ_s(COO) at 1400 cm^{-1}, showed the non metal-oxygen feature in the molecule. The bands in the fingerprint region, 1041, 967, 932, 849, 792, 719, 630, 567, 511, and 459 cm^{-1}, can all be attributed to the mixed valence Mo-O vibrations. Fine structues form gas phase H_2O rotation modes care also observed

over the range of 1450-1900cm^{-1}, since the $(NH_4)_{42}[Mo_{132}O_{372}(CH_3COO)_{30}(H_2O)_{72}] \cdot \sim 300H_2O$ crystals we got are pretty wet.

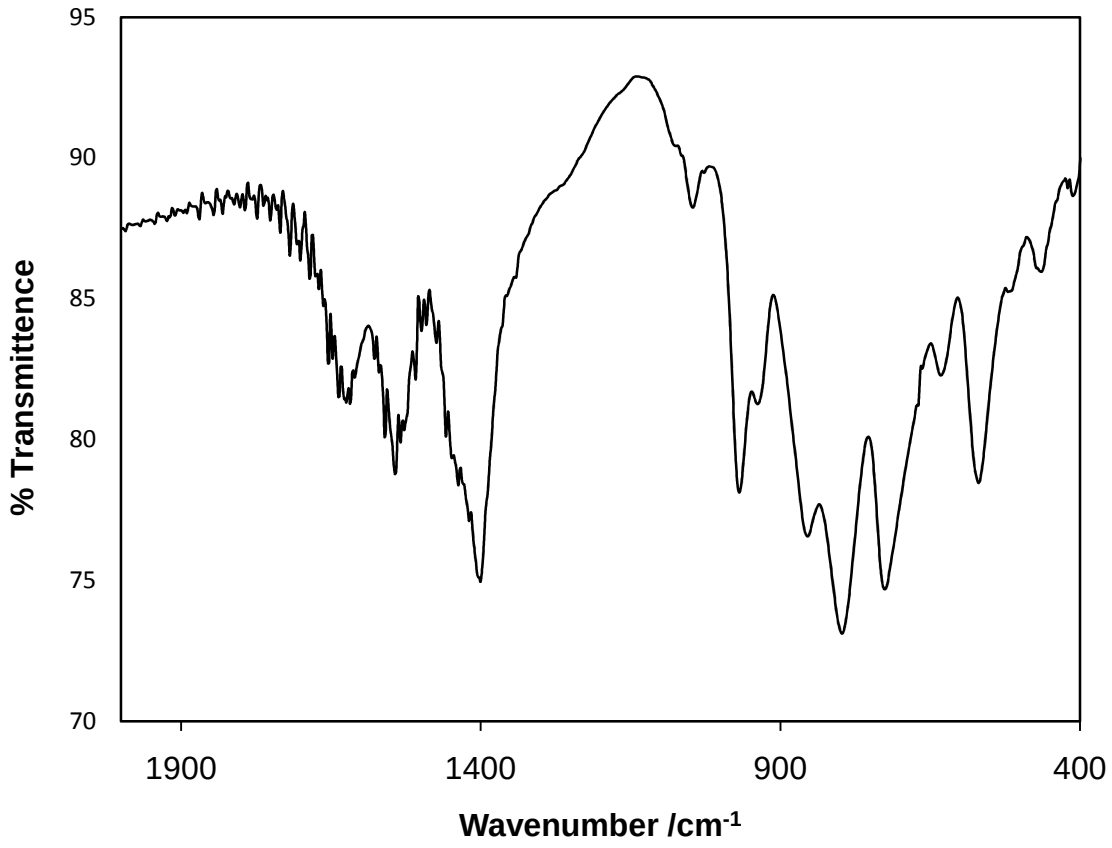

Figure 5.4 Transmission FT-IR spectrum of $(NH_4)_{42}[Mo_{132}O_{372}(CH_3COO)_{30}(H_2O)_{72}] \cdot \sim 300H_2O$ Keplerate polyoxometalate in a KBr pellet.

5.3.2 Cu^{2+} induced decomposition of $[Mo_{132}O_{372}(CH_3COO)_{30}(H_2O)_{72}]^{42-}$ Keplerate type Polyoxometalate

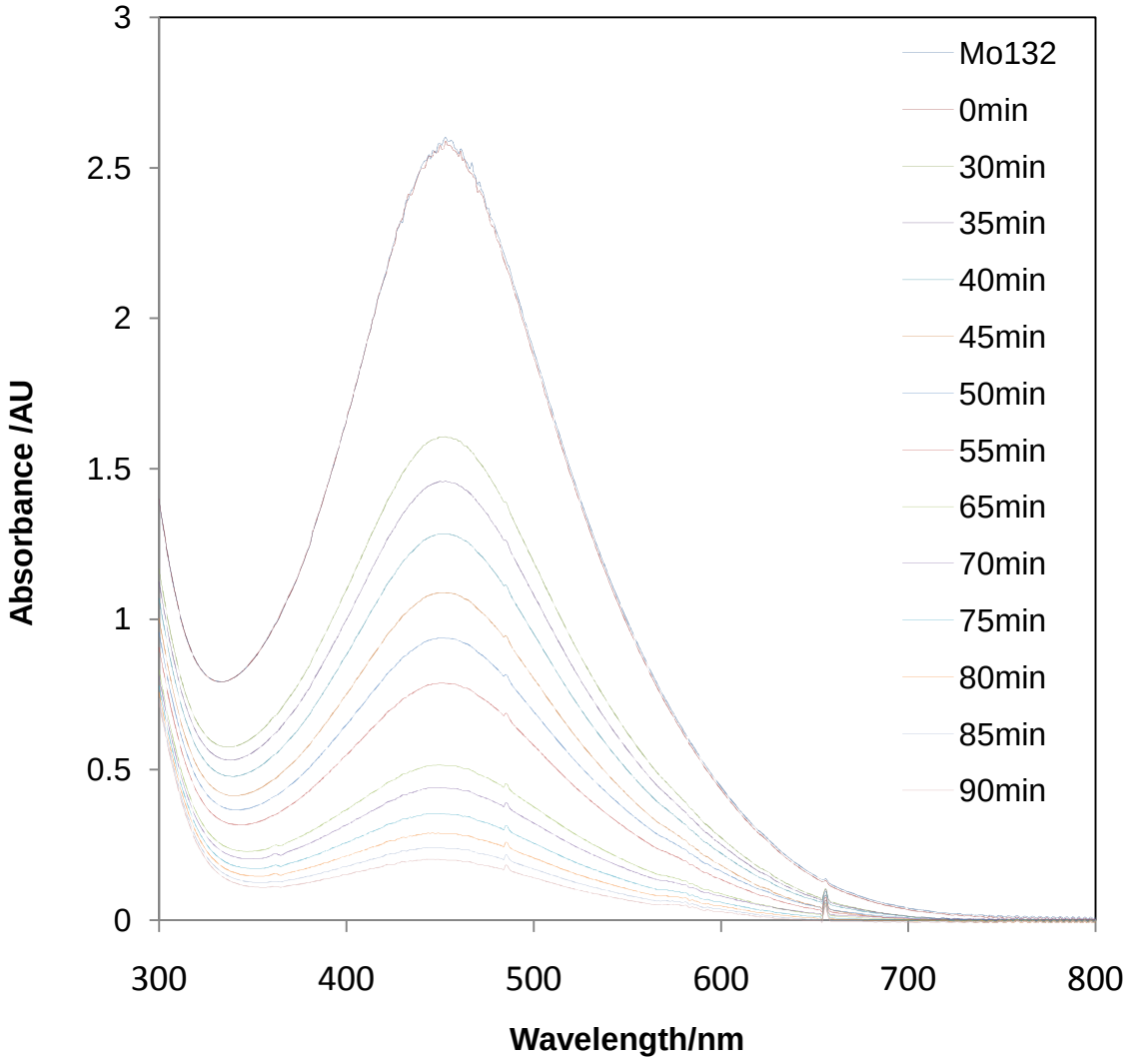

Figure 5.5 Typical time-based UV-vis spectra. The solution contains 0.01mM Mo_{132}, 10mM Cu^{2+}.

Cu^{2+} induced decomposition of $[Mo_{132}O_{372}(CH_3COO)_{30}(H_2O)_{72}]^{42-}$ Keplerate type Polyoxometalate can be confirmed by UV-vis spectroscopy and Raman spectroscopy. Typical time-dependence UV-vis spectra are shown in Figure 5.5.

The pure Mo_{132} solution shows a characteristic UV-vis resonance band showing the Mo^{V}-Mo^{VI} mixed valence feature centered at 454nm. After adding the Cu^{2+}, the intensity of the mixed valence feature band decreased over time, which implied that the Mo^{V}-Mo^{VI} mixed valence structure disappeared gradually, suggesting a slow decomposition of the mixed valence $Mo^{VI}_{72}Mo^{V}_{60}\ O_{372}(CH_3COO)_{30}(H_2O)_{72}]^{42-}$ Keplerate type polyoxometalate.

After the solution completely turn light blue, which only indicating the color of Cu^{2+}, the mixed valence $Mo^{VI}_{72}Mo^{V}_{60}O_{372}(CH_3COO)_{30}(H_2O)_{72}]^{42-}$ Keplerate type Polyoxometalate is considered totally destroyed. Then the solution was evaporated into 1/10, and colorless crystals were collected for Raman spectroscopy, which is shown in Figure 5.6.

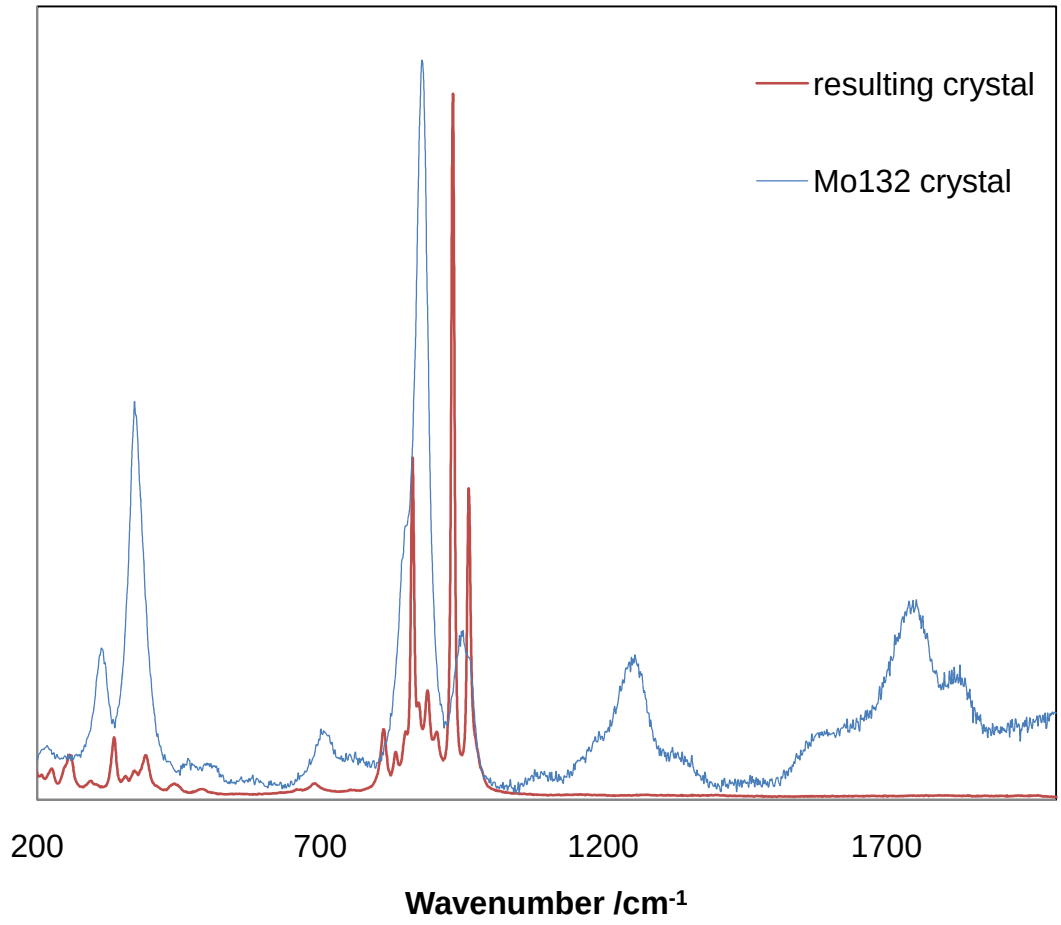

Figure 5.6 Raman spectra of $(NH_4)_{42}[Mo_{132}O_{372}(CH_3COO)_{30}(H_2O)_{72}]$ polyoxometalate and its degradation product.

The Raman results showed two totally different spectra of the Mo_{132} POM and its degradation product, which confirmed that the mixed valence $Mo^{VI}_{72}Mo^{V}_{60}O_{372}(CH_3COO)_{30}(H_2O)_{72}]^{42-}$ Keplerate type Polyoxometalate is fully destroyed. According to Reference 4, the broad band centered at 953cm^{-1}, 875cm^{-1}, 374cm^{-1}, and 314cm^{-1}

are corresponding to the mixed valence Mo-O vibration. And the broad bands centered at $1362cm^{-1}$ and $1750cm^{-1}$ are due to NH_4^+ and H_2O in $(NH_4)_{42}[Mo_{132}O_{372}(CH_3COO)_{30}(H_2O)_{72}]\cdot\sim 300H_2O$ Keplerate type polyoxometalate respectively. All these bands are not observed in the Raman spectra of decomposition products. The narrow sharp peaks observed in the product Raman spectrum suggested that the Keplerate type polyoxometalate had been fully converted to simple molybdenum oxides.

Interestingly, the UV-vis spectra showed the same intensity drop between every five minutes, which suggested that the decomposition rate remained the same while the POM concentration decreased. To further look into this, additional UV-vis studies were performed by monitoring the 454nm peak intensity changed over time, as shown in Figure 5.7. Cu^{2+} was added into the solution at t=600s.

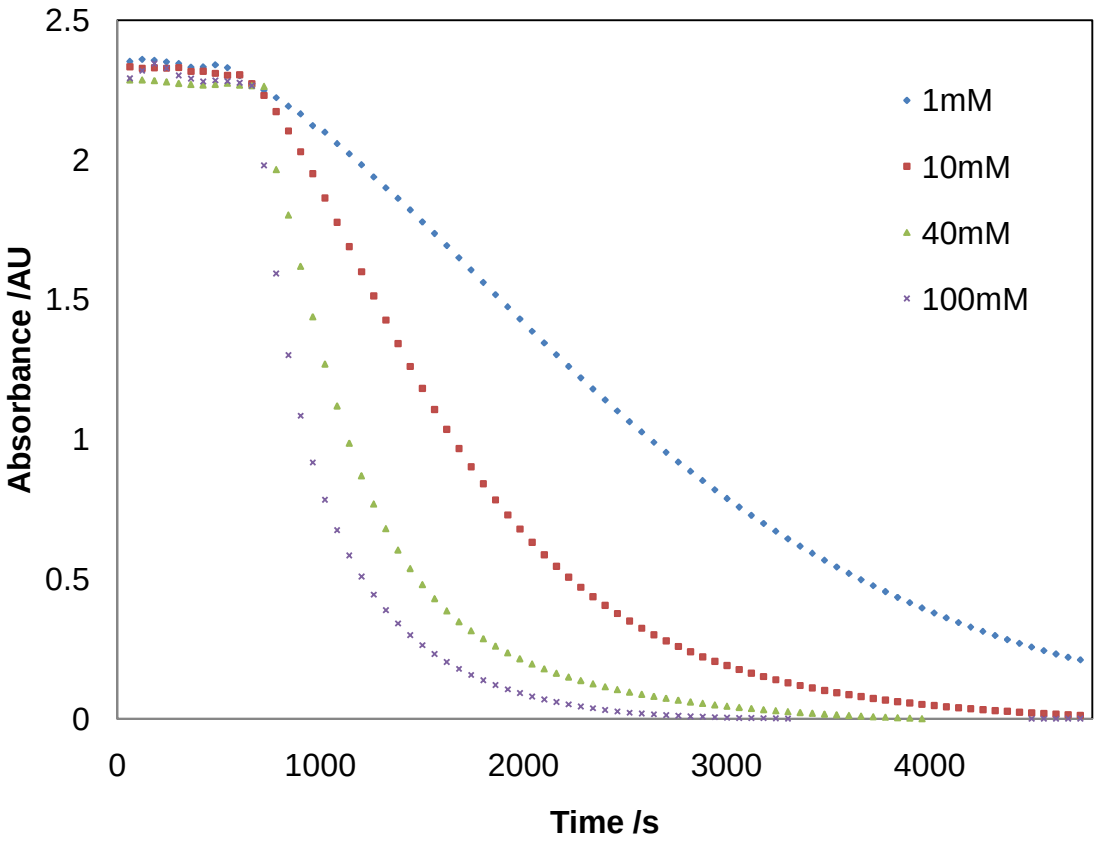

Figure 5.7a Peak intensity at λ=454 nm change as a function of time at different Cu^{2+} concentration. Cu^{2+} was added at t=600s.

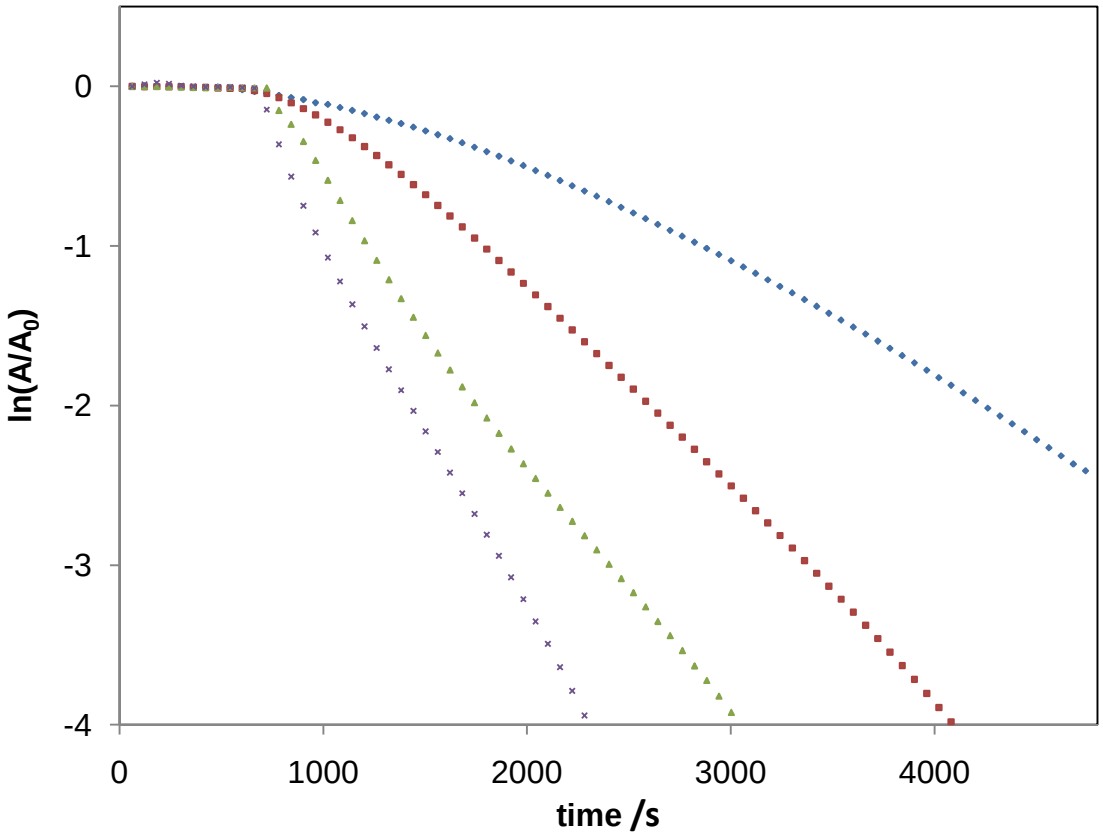

Figure 5.7b Ln(A/A_0) as a function of time at different Cu^{2+} concentration. Cu^{2+} was added at t=600s.

By keeping [POM] constant, the influence of [Cu^{2+}] was studied. From Figure 5.7a, it can be observed that the absorbance of POM is steady until addition of Cu^{2+}, indicating that the mixed valence Keplerate polyoxometalate $Mo^{VI}_{72}Mo^{V}_{60}O_{372}(CH_3COO)_{30}(H_2O)_{72}]^{42-}$ itself is stable in water. After Cu^{2+} addition, the absorbance intensity started to drop. Thus, we can conclude that the higher concentration of [Cu^{2+}], the faster the drop was.

From Figure 5.7b, a linear feature could be easily observed when plotting $ln\frac{A}{A_0}$ versus time, which suggested that the overall decomposition reaction kinetics is psudo-first order. The same conclusion could be achieved by another UV-vis kinetic study, which kept [Cu^{2+}] constant and varied {$Mo^{VI}_{72}Mo^{V}_{60}O_{372}(CH_3COO)_{30}(H_2O)_{72}]^{42-}$}, as shown in Figure 5.8.

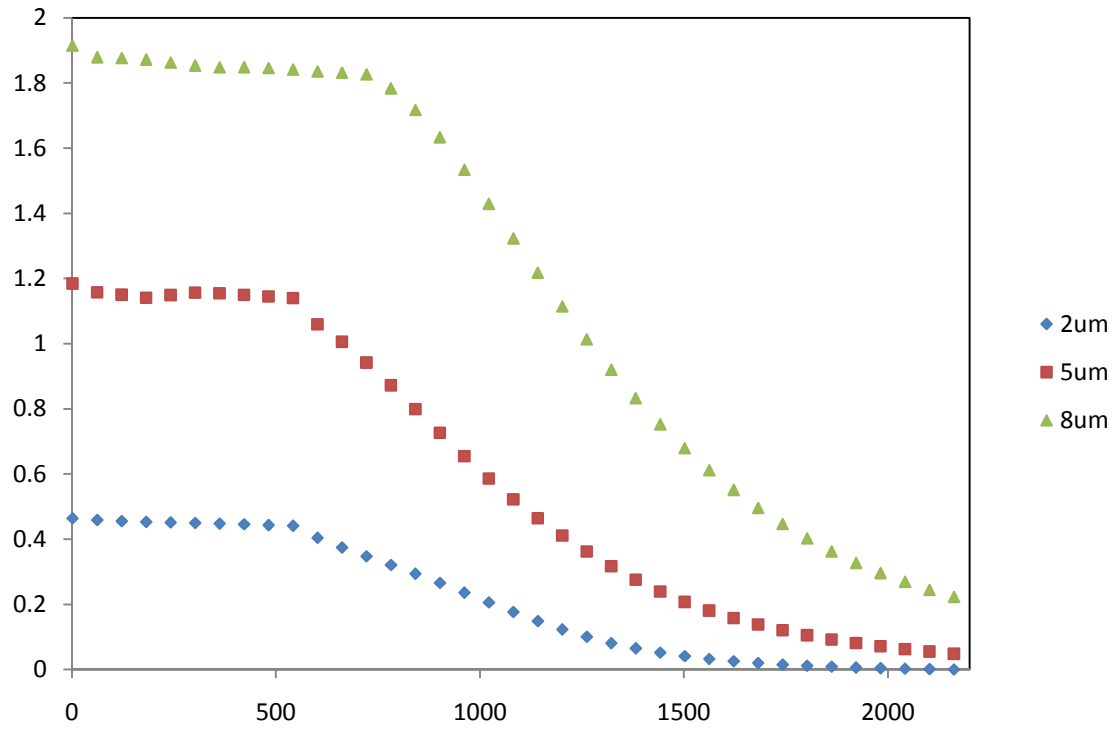

Figure 5.8 Peak intensity at λ=454 nm change as a function of time at different POM concentration. Cu^{2+} was added at t=600s.

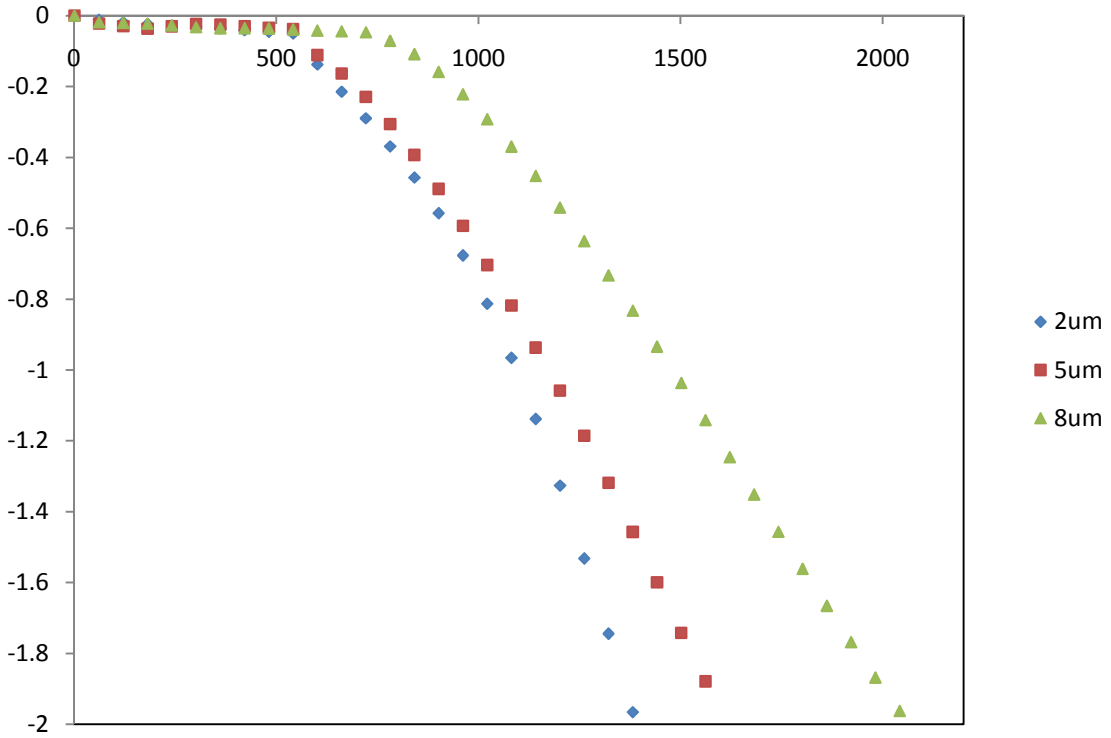

Figure 5.8 $Ln(A/A_0)$ as a function of time at different POM concentration. Cu^{2+} was added at t=600s.

5.4 Conclusions

From the above investigations, it can be draw to a conclusion that $Mo^{VI}_{72}Mo^{V}_{60}O_{372}(CH_3COO)_{30}(H_2O)_{72}]^{42-}$ is not a suitable model system to study mixed valence di-copper compound in aqueous environment, due to the Cu^{2+} catalyzed degradation of the Keplerate polyoxometalate. The degradation reaction kinetics is first order. Some other model systems are needed to mimic the di-copper enzyme. However, by having numerous advantages, such as high solubility in water, multi metal binding sites in the inner side of the hollow structure,

larger inner volume with multiple channel for ion transportations, $Mo^{VI}_{72}Mo^{V}_{60}O_{372}(CH_3COO)_{30}(H_2O)_{72}]^{42-}$ Keplerate polyoxometalate is still a promising inorganic candidate for mimicking biological cells, especially for small ion uptake and release.

References

(1) Sigwart, C.; Hemmerich, P.; Spence, J. T., Binuclear mixed-valence copper acetate complex as a model for copper-copper interaction in enzymes; *Inorg Chem* **1968**, 7, (12), 2545–2548.

(2) Toledo, I.; Arancibia, M.; Andrade, C.; Crivelli, I., Redox chemistry of copper acetate binuclear complexes in acetic acid-methanol mixture as solvent; *Polyhedron* **1998**, 17, (1), 173-178.

(3) Crivelli, I. G.; Andrade, C. G., Hush theory in a copper mixed valence bioinorganic model generated photochemically *Inorg. Chim. Acta* **1998**, 203, (1), 115-120.

(4) Müller, A.; Krickemeyer, E.; Bögge, H.; Schmidtmann, M.; Peters, F., Organizational Forms of Matter: An Inorganic Super Fullerene and Keplerate Based on Molybdenum Oxide; *Angew. Chem. Int. Ed.* **1998**, 37, (24), 3360-3363.

(5) Rehder, D.; Haupt, E. T. K.; Müller, A., Cellular cation transport studied by ^{6,7}Li and ^{23}Na NMR in a porous Mo_{132} Keplerate type nano-capsule as model system; *Magnetic Resonance in Chemistry* **2008**, 46, (S1), S24-S29.

Chapter 6.

Conclusions and Recommendations for Future Work

The primary objective of this research work was to employ these versatile polyoxometalate structures as electron mediators in nano-scale applications. For this purpose, several polyoxometalate structures were successfully synthesized and characterized. We have successfully demonstrated that polyoxometalates can conduct electrons, not only between conventional electrodes and nanoparticles (Chapter 2 and 3), but also between adjacent nanoparticles assembly layers (Chapter 3), and among individual nanoparticles (Chapter 4). The electron shuttling properties of polyoxometalates opens a door for electrochemistry for nanomaterials.

In terms of methanol oxidation, polyoxometalates grab the photo-generated electrons from conduction band of dispersed TiO_2 nanoparticles to platinum electrode, preventing them from recombining with electron holes in valence band. This process protects a significant amount of electron holes, and thus boosting the methanol oxidation rate. The efficiency of the polyoxometalate assisted hybrid photo-electrochemical cell is 50 times greater than similar photo-electrochemical system without the polyoxometalates. Although the system has been applied in some other fields, this is the first example of using polyoxometalate-TiO_2 co-catalytic photo-electrochemical system in methanol oxidation. Some optimizations, such as

polyoxometalateconcentration dependence, pH dependence, are executed as well. Further optimizations are needed to improve the performance/price ratio. For example, we used a whole full beaker of dispersed TiO_2 solution to reach a larger light accepting area, which might be largely excessed to what the system really need. An optimization of dispersed TiO_2 solution to electrode area is desired to reduce the cost and device size. And a fuel cell system test is needed for further investigation to adopt the polyoxometalate-TiO_2 co-catalytic photo-electrochemical system to the real methanol fuel cell. The polyoxometalate-TiO_2 co-catalytic photo-electrochemical can be used in other applications too. The final products of methanol oxidation should be identified as well.

Au nanoparticle inside films prepared on glassy carbon supports by depositing alternating layers of positively charged poly(diallyldimethylammonium)-stabilized Au nanoparticles and negatively charged Cobalt substituted α_2-Wells-Dawson-polyoxometalate ($CoP_2W_{17}O_{61}^{8-}$) interlayers are electro-active. The polyoxometalate anions play as electron shuttle transferring electrons between the carbon electrode and Au nanoparticles, as well as between adjacent Au nanoparticles layers. CuI was deposited onto the surface of Au nanoparticles using electrochemical atomic layer deposition, while CdS and CdTe films were grown by an atom-by-atom codeposition method. The conventional ways to prepare metal-semiconductor core-shell nanoparticles are wet-chemistry, usually involve toxic organic solvent, high temperature, expensive precursors. And the thickness of the semiconductors shell is predetermined by the precursors added before the reaction starts, which lacks flexible control. In contrast, electrochemical methods offer numerous advantages over wet-chemistry, such as aqueous solvents, room-temperature deposition, low cost, and precise control of composition and thickness. However, the lack of electrically addressable nanoparticles makes electrochemical

synthesis of metal-semiconductor core-shell nanoparticles very difficult. Ours is the first example of synthesis of metal-semiconductor core-shell nanoparticles using electrochemical methods. However, we confirm the synthesis using only electrochemistry and spectroscopic methods. Microscopic methods such as TEM are desired to provide direct evidence of the formation of the core-shell structure, as well as morphology and defects on the shell. However, the layer-by-layer assembly is very stable. To get Au nanoparticles out of it, we need to use harsh conditions to break the layer-by-layer film, which would destroy the nanoparticles as well. Some better methodologies should be devised to achieve this goal. And the metal nanoelectrode array can be used in other applications too.

The dual function role of polyoxometalate in nanoparticles synthesis is already well-known. However, the Ag nanoparticles synthesized by $[WZn_3(H_2O)_2(ZnW_9O_{34})_2]^{12-}$ in return assist the polyoxometalate blackberry structure formation is a big surprise. Polyoxometalates that reported to self-assembled into the blackberry structures by themselves have very large sizes. $[WZn_3(H_2O)_2(ZnW_9O_{34})_2]^{12-}$ is very small, compared to those so-called "giant polyoxometalates". The polyoxometalate shell has been proved to be able to separate the inside and outside solution of the blackberry structure by other researchers using fluorescence spectroscopy. The Ag nanoparticles on the blackberry structure might be able to serve as an electrochemical probe for the inside blackberry environment. Future research may also be focused on surface enhanced Raman spectroscopy (SERS) of the inside blackberry environment to take advantages of the Ag nanoparticles.

Further focus of the Cu^{2+} catalyzed degradation of giant mixed valence polyoxometalate $[\{(Mo^{VI})Mo^{VI}_5O_{21}(H_2O)_6\}_{12}\{Mo^{V}_2O_4(CH_3COO)\}_{30}]^{42-}$ should be focused on detail degradation mechanism, the role that acetate plays, and reason why the degradation is only sensitive to Cu^{2+},

but not other di-valent metal cations, such as Co^{2+} and Ni^{2+}, might also worth to be explored. To achieve these three goals, collaborations with other faculties are recommended. Understanding of the decomposition mechanism would help in design and synthesize new type of polyoxometalates as well.